Artificial Magnetic Materials for High Gain Planar Antennas

by

Hussein Mahmoud Abdelsalam Attia

A thesis
presented to the University of Waterloo
in fulfillment of the
thesis requirement for the degree of
Doctor of Philosophy
in
Electrical and Computer Engineering

Waterloo, Ontario, Canada, 2011

I hereby declare that I am the sole author of this thesis. This is a true copy of the thesis, including any required final revisions, as accepted by my examiners.

I understand that my thesis may be made electronically available to the public.

Abstract

A new method is proposed to enhance the gain and efficiency of planar printed antennas. The proposed method is based on using artificial magnetic materials as a superstrate for planar printed antennas while maintaining the low-profile attractive feature of these antennas. It is found that the antenna's gain increases as the permeability of the superstrate increases. Due to the lack of low-loss natural magnetic materials in the microwave band, designing artificial materials with magnetic properties has become increasingly attractive in recent years. In particular, using magneto-dielectric superstrates reduces the wavelength in the media leading to a miniaturized composite structure (antenna with superstrate). The split ring resonator SRR is used as a unit cell of an artificial magnetic superstrate for a microstrip antenna to enhance the antenna gain and efficiency. Also, in this work, mechanism of operation for artificial magnetic materials is theoretically investigated. Analytical and numerical methods are provided to model the behaviour of these materials.

Full-wave analysis of multilayered periodic structures is an expensive computational task which requires considerable computer resources. In this work, a fast analytical solution for the radiation field of a microstrip antenna loaded with a generalized superstrate is proposed. The proposed solution is based on using the cavity model in conjunction with the reciprocity theorem and the transmission line analogy. The proposed analytical formulation reduces the simulation time by two orders of magnitude in comparison with full-wave analysis. The method presented in this work is verified using both numerical and experimental results for the case of a patch antenna covered with an artificial 3D periodic superstrate.

Another useful feature of a microstrip antenna covered with superstrate is controlling the direction and beamwidth of the main beam of the antenna. Beam steering has been traditionally implemented in antenna arrays using phase shifters which result in complex and expensive structures and suffer from high loss and mass. This work provides a novel method to steer the main beam of a patch antenna by partially covering it with a high refractive index superstrate. The beam steering of a single patch is possible because of the dual-slot radiation mechanism of the microstrip antenna (according to the cavity model). Full-wave simulations, analytical modeling and experiments are provided to support the proposed technique of beam steering in planar antennas.

Acknowledgements

Dedication

To the brave people of Egypt who triggered the Egyptian Revolution *peacefully* on Jan. 25 - Feb. 11, 2011 for seeking their virtue, freedom and dignity.......

Table of Contents

List of Tables

List of Figures

Chapter 1

Introduction

1.1 Motivation

Microstrip patch antennas have many attractive features, such as low profile, ease of fabrications, light weight and compatibility with planar circuitry [1]–[6]. However, microstrip antennas have major disadvantages such as narrow impedance bandwidth, low gain and efficiency, which limit the application of the microstrip antennas significantly. The gain of a typical patch antenna on a grounded substrate is about 5 - 8 dBi [7]–[10].

To overcome the problem of low gain for planar printed antennas, a method involving the addition of a superstrate (cover layer) over radiation sources (microstrip patch, wire or aperture antenna) was recently discussed [11]–[17]. This method utilizes a superstrate (cover layer) with dielectric constant greater than 1 and/or relative permeability greater than 1 and one can achieve a very high gain at any desired angle θ by choosing the appropriate configuration of the superstrate layer [8] (see Fig. 1.1). On the other hand, the gain of microstrip antennas can be increased by using planar arrays; an attractive solution as it does not increase the vertical profile of the antenna structure. However, planar arrays need a feeding network which introduces losses and design complications [18]–[22]. Moreover, arrays increase the footprint of the radiating system.

In addition to the aforementioned benefits of using a superstrate cover layer for antenna application, superstrate (cover) dielectric layer are often used to shield the antenna from its environment hazards (wind, rain, sand, UV, ice, etc.) and/or hide antenna electronic
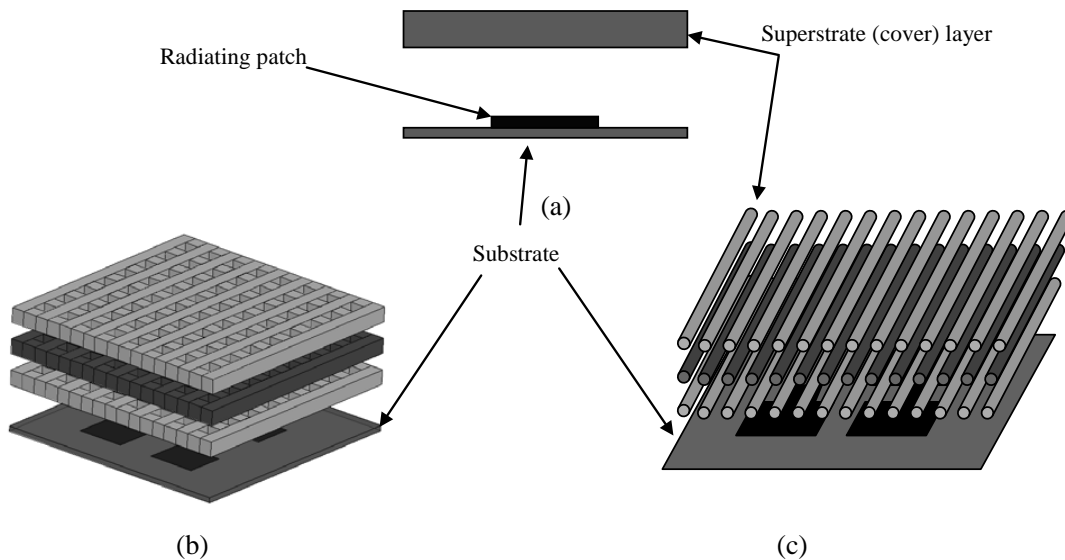
Figure 1.1: Different Configurations for superstrate cover layers over microstrip patch antennas. (a) Side view of a conventional dielectric superstrate layer over a single patch microstrip antenna. (b) Cross-stacked EBG (electromagnetic bandgap) superstrate for a 2X2 microstrip array antenna. (c) Cylindrical rods EBG superstrate for a 2X2 microstrip array antenna.

equipment from public view. Also, these superstrate layers may be naturally formed (e.g. ice layers) during flight or severe weather conditions especially when placed on aircrafts and missiles.

Whether a superstrate cover layer is naturally formed or impressed by the antenna designer, it is necessary to study and optimize this superstrate cover layer to enhance the antenna basic performance characteristics, such as gain, radiation resistance and efficiency enabling the cover to act as a desirable part of the antenna as well as a weatherproof enclosure to protect the antenna. Furthermore, in the case of integrating microstrip antennas in RF (radio frequency) integrated circuits which usually have substrates such as gallium arsenide (GaAs) or silicon (Si), the antenna radiation efficiency and gain is reduced dramatically because of the high value of the substrate relative permittivity and the associated surface wave effects. For this reason, it is important to develop a technique to increase the

2

antenna radiation efficiency and gain.

1.2 Previous Work on Enhancement of the Gain of Planar Antennas

Previous research on enhancing the gain of planar printed antennas using superstrate layers can be classified into three categories according to the approach and the superstrate configuration. More details about these categories are given in the following sub-sections.

1.2.1 Resonance Conditions for Substrate-Superstrate Printed Antenna

The work in [7]–[12] covers research on investigating the resonance conditions for a substrate-superstrate printed antenna geometry which allows for large antenna directivity and gain. In [7], partially-reflective surface was used as a superstrate to cover an antenna over a ground plane to improve its directivity. A simple ray-tracing method was used to show that the resultant high directivity was due to the multiple reflections occurring between the reflective superstrate surface above and the ground plane beneath the source antenna. Also in [7], it was shown that the resonant spacing between the antenna and its superstrate should be as large as $\lambda/2$ to achieve high directivity.

In [8], asymptotic formulas for gain and beamwidth of a horizontal Hertzian dipole embedded within a grounded substrate were calculated analytically. It was shown that using a superstrate layer over this antenna would result in large antenna gain as the permittivity or permeability of the superstrate becomes large. This method was extended to produce narrow patterns about the horizon, and directive patterns at two different angles [8]. In [9], it was shown that using a thick superstrate (about a half-wavelength in the medium), a resonance condition may be created whereby gain and radiation resistance are improved over a significant bandwidth.

In [10], a modified gain enhancement method was proposed which is based on multiple superstrate layers which all have to be electrically quarter wavelength thick. It was shown in [10] that extremely large resonance gain can be obtained even with moderate values of

permittivity and permeability of the multiple superstrate layers. This method was also applied to obtain the radiation patterns of printed circuit antennas with inhomogeneous substrates, it was reported that the radiation pattern is affected noticeably when the inhomogeneity in the substrate is not weak [10]. As shown in [8]–[10], the gain and radiation resistance are improved over a significant bandwidth. However, these structures require thick layers, leading to an overall antenna size which could be incompatible with integrated circuit antenna applications. Moreover, the bandwidth varies inversely with gain so that a moderate gain limit is established for practical antenna operation and, therefore, the design becomes more sensitive to the device parameters. Furthermore, the aperture efficiency of these configurations [8]–[10] is typically less than 60%.

In [11], the experimental results of 2x8 array antenna with a superstrate and 4x8 array antenna without a superstrate were shown. The designed 2x8 array antenna using the superstrate had a high gain of 22.5 dBi and wide impedance bandwidth of 17%. In [12], the properties of microstrip patch antennas with double superstrates were studied, a directivity of about 16 dBi within a bandwidth of 11% was obtainable, with a superstrate relative permittivity of 3.2 and a surface area of 40 X 40 mm^2.

1.2.2 Electromagnetic Bangap (EBG) Material as a Superstrate

The work in [13]–[17] covers research on using electromagnetic bangap (EBG) material as a superstrate to enhance the basic properties of planar printed antennas such as gain and radiation efficiency. EBG materials when used as a superstrate for planar printed antennas act as a spatial angular filter for filtering undesired radiation by sharpening the radiation pattern (grating-lobe suppression) and thus increasing the antenna gain.

In [13], Cheype et al. have introduced a new explanation of the electromagnetic bangap (EBG) material. This explanation is based upon breaking up the periodicity of the EBG material by introducing defects into the periodical structure, and hence an allowed band inside the forbidden bandgap would be created. It was reported that using this EBG structure as a superstrate for a microstrip patch antenna would increase the gain by 13 dBi [13]. However, the height of the whole structure (antenna with superstrate) was about 61 mm (one wavelength in free space at 4.75 GHz) which sacrifices the low-profile attractive feature of patch antennas. Also, the planar size of the ground plane was 13 times the patch size.

In [14], Lee et al. have introduced two different defects inside the EBG material, one introduced by the ground plane of the microstrip patch antenna and the other produced by a row of defect rods with different dielectric constants in the EBG structure. They have presented a design methodology for controlling the defect frequencies of the EBG superstrate for specified frequency bands. They have also presented three applications of the EBG superstrate covering a class of patch antennas: i) a superstrate for dual-band dual-polarization; ii) a compact superstrate with wide directivity bandwidth; and iii) a cover for an array antenna to suppress its grating lobes. They have demonstrated that it is possible to achieve significant directivity enhancements of the antenna with EBG superstrates, and that the EBG also help with the polarization isolation. But, the authors have not discussed the effects of the superstrate layers on the antenna radiation efficiency and input impedance bandwidth [14].

In [15], two different designs have been studied for the application of EBG as a superstrate for 2X2 microstrip array antenna. It was shown that the cross-stacked EBG superstrate improves the input impedance bandwidth and reduces the overall size of the antenna in comparison to previous designs.

In [16], Pirhadi et al. examined a combination of a frequency selective surface (FSS) as a superstrate layer and an artificial magnetic conductor (AMC) ground plane in high-directivity EBG resonator antennas. Also, it was reported that using artificial magnetic conductor (AMC) ground plane compared to conventional perfect electric conductor (PEC) ground plane helps to design more compact structures in the same operating frequency(ies). This characteristic is achieved due to the ability of the artificial ground plane to adjust its reflection phase and to excite resonance modes that cannot be excited in the presence of PEC ground plane [16].

In [17], a thin, two layered frequency selective surface (FSS) type of metamaterial superstrate for dual-band directivity enhancement was presented as an alternative to a conventional FSS superstrate, which is thicker. Based on the unit-cell simulation, Lee et al. investigated several important parameters to determine their effects and have presented the design guidelines for controlling the resonant frequency as well as the quality factor of the FSS superstrate [17].

1.2.3 Engineered Periodic Materials (Metamaterials) as Superstrate

This category represents the most recent trend to enhance the gain of planar antennas. It covers research on using engineered periodic materials (metamaterials) [23]–[30] as a superstrate to enhance the basic properties of planar printed antennas such as gain and radiation efficiency and to reduce the overall size of the superstrate antenna composite. Recently it was shown that using magneto-dielectric materials instead of dielectrics offer many advantages in antennas applications. Magneto-dielectrics are materials which can be polarized both electrically and magnetically when exposed to an applied electromagnetic (EM) field, so they have both relative permeability and permittivity higher than one. When materials with only high permittivity are used as superstrates for gain enhancement, the thickness of the superstrate is large, about $\lambda/2$ in the medium [8]–[10]. But in the case of magneto-dielectric materials, the wavelength in the medium is much smaller, leading to a miniaturized composite structure. However, in the microwave region, naturally occurring magnetization is not possible due to the inertia of the atomic system that is not able to track an electromagnetic field with high frequency. Therefore, designing superstrates with magnetic properties that do not exist in naturally-occurring materials has become increasingly attractive in recent years [30]–[33]. Generally, an engineered magnetic substrate is composed of small resonating inclusions which exhibit magnetic properties within a frequency band centered at their resonance frequency. Presently developed engineered magnetic materials, due to their resonating nature, are strongly frequency dispersive leading to poor performance in wide-band microwave applications [34].

The work in [35]–[37] represent samples of this third category. In [35], three configurations were presented to reduce the size of a high-gain planar antenna. Initially, a conventional microstrip antenna with a high-permittivity dielectric superstrate was designed. Then, using a periodic structure of metallic patches acting as an artificial magnetic conductor (AMC), the antenna size was reduced. Furthermore, another size reduction method for this class of high-gain antennas was proposed using magneto-dielectric materials which also provided much wider bandwidth and eliminated the sidelobes of the radiation patterns. However, in [35], the potential applications of magneto-dielectric materials were investigated without considering the realization and fabrication of these magneto-dielectric materials.

In [36], the behaviour of a multi-frequency dipole antenna array that is closely placed to a meta-surface superstrate was experimentally investigated. The proposed meta-surface was based on resonating unit cells formed by capacitively loaded strips and split ring resonators (SPRs). Radiation efficiency values for this configuration of more than 80% and gain values of more than 4.5 dBi were obtained [36].

In [37], Latrach et al. used edge-coupled split ring resonator (SRR) inclusions to provide artificial superstrate comprising alternately layers with negative permeability and positive index of refraction materials to increase the gain of a patch antenna. However, Latrach et al. [37] did not present any design guidelines for the SRRs unit cells and did not provide an explanation for how the engineered superstrate increased the antenna gain.

1.3   Objectives and Scope

The objectives of this research are described in the following points.

- Providing an analytical formulation for the radiation field of a microstrip antenna loaded with a superstrate. The proposed analytical formulation reduces the simulation time significantly and also provides physical insight to understand the gain enhancement mechanism of such structures (antenna with superstrate).

- The derivation of the resonance conditions required to achieve the highest possible gain and efficiency of the whole radiating system (patch antenna with superstrate). These resonance conditions depend on the thickness of each layer in the radiating system and the proper choice of the permeability and permittivity of the superstrate.

- Design, analysis and fabrication of artificial magnetic material to be used as a superstrate of planar printed antenna in order to increase the gain and efficiency of the antenna without enlarging the size of the whole radiating system significantly. Moreover, Hessian matrix (i.e., the second derivatives of the Lagrangian multipliers) method [38] will be used to optimize the directivity of a patch antenna covered with a superstrate having arbitrary thickness, permeability and permittivity and placed at an arbitrary distance over a patch antenna.

- In this thesis, I propose a novel implementation of the antenna-superstrate configuration in which the superstrate is *displaced* along the E-plane of the patch such that it covers only one of the radiation slots of the patch antenna (according to the cavity model). The effect is to steer the main beam of the patch antenna by *partially* covering it with a high-refractive index superstrate. Moreover; the antenna gain will be enhanced. The beam steering of a single patch is possible because of the dual-slot radiation mechanism of the microstrip antenna. In effect, the electromagnetic radiation from the covered radiating slot reaches the far-field with an additional phase with respect to the uncovered slot, resulting in an inclined beam whose angle depends on the superstrate's refractive-index.

1.4   Thesis Organization

The thesis consists of 7 chapters and one appendix including the present chapter which is "Introduction".

- **Chapter 2**: A fast and accurate analytical technique will be developed to calculate the radiation field of a microstrip antenna covered with a generalized superstrate. The analytical formulation is based on using the cavity model to replace the patch antenna by two magnetic line sources. The reciprocity theorem and transmission line analogy are used to calculate the far field of the two magnetic line sources representing the patch antenna.

- **Chapter 3**: It is shown that, under some resonance conditions, a microstrip patch antenna can be designed to achieve the highest possible gain when covered with a superstrate at the proper distance in free space. The transmission line analogy and the cavity model are used to deduce the resonance conditions required to achieve the highest gain. The resonance conditions depend on the spacing between the antenna substrate and the superstrate and on the thickness of the superstrate. The permeability and permittivity of the superstrate are determined based on these resonant lengths and the appropriate characteristic impedance of each layer in this multilayered structure.

- **Chapter 4**: Based on the resonance conditions derived in Chapter (3), which require a high-permeability superstrate to enhance the antenna gain, this chapter explains the operational principle of the artificial magnetic materials as an emulation of the magnetization occurred in natural magnetic materials. The equivalent circuit model of the split ring resonator SRR unit cell acting as a building block of the engineered superstrate will be provided and the analytically calculated effective permeability and permittivity will be found to be in a good agreement with the numerically calculated parameters using a plane wave incident on the metamaterial SRR unit cell.

- **Chapter 5**: By utilizing the design guidelines presented in the previous chapter for the unit cell of an artificial magnetic superstrate, this chapter presents the experimental and numerical analysis of a patch antenna covered with an engineered magnetic superstrate. It is shown that for a patch antenna resonating at 2.2 GHz, using the engineered magnetic superstrate results in a 3.8 dBi enhancement in gain and 14% enhancement in efficiency, while maintaining an antenna profile of $\lambda_0/7$. The planar size of the radiating system was only 2.3 times the patch size. These improvements were achieved while having an insignificant effect on the impedance bandwidth of the antenna.

  Furthermore, the analytical formulation for the radiation field explained in Chapter (2) is used to calculate the radiation field of the microstrip antenna covered with an artificial magnetic superstrate. The proposed analytical model is implemented and verified by a comparison with experiments and full-wave simulations. The proposed analytical formulation reduces the simulation time by two orders of magnitude in comparison with full-wave analysis.

- **Chapter 6**: A novel mechanism of steering the main beam of a microstrip antenna using high refractive-index superstrate is presented. Moreover; the antenna gain is enhanced. The proposed configuration consists of the high refractive-index superstrate partially covering the patch such that one of the radiation slots is exposed. Through full-wave simulations and experiments, the main beam of the antenna is shown to deflect to higher angles as the refractive index of the superstrate is elevated. The radiation mechanism is investigated by plane wave approximations and antenna array theory. The two radiation slots act as a two-element array with a phase disparity that is created by the placing of the superstrate layer on one of the slots.

Good agreement between the proposed plane wave model and the HFSS simulations was obtained despite the huge difference in computational resources used by the two methods. The proposed model consumed only 1/100 of the time taken by HFSS. The proposed method can be of commercial value when used in antenna array systems for radar applications. With tuneable engineered superstrate, a reconfigurable beam steerable microstrip patch can be obtained.

- **Chapter 7**: This chapter summarizes the most important elements of this thesis. Also, the implications of various aspects of this research are presented and possible topics for future research are discussed.

Chapter 2

Analytical Model for Calculating the Radiation Field of Microstrip Antennas With Generalized Superstrates

2.1 Introduction

In this chapter, a fast analytical solution for the radiation field of a microstrip antenna loaded with a generalized superstrate is proposed. This analytical solution is based on the cavity model of microstrip antennas in conjunction with the reciprocity theorem and the transmission line analogy. The proposed analytical formulation for the antenna far-field is much faster when compared to full-wave numerical methods. It only needs 2% of the time acquired by full-wave analysis. Therefore; the proposed method can be used for design and optimization purposes. The method is verified using both numerical and experimental results. This verification is done for both conventional dielectric superstrates and artificial periodic superstrates. The analytical formulation introduced here can be extended for the case of a patch antenna embedded in a multilayered artificial dielectric structure. To the best of our knowledge, the proposed analytical technique is applied for the first time for the case of a practical microstrip patch antenna working in the Universal

Mobile Telecommunications System (UMTS) band and covered with a superstrate made of an artificial periodic metamaterial with dispersive permeability and permittivity.

The addition of a superstrate layer over a microstrip patch antenna (MPA) has been reported to allow for the enhancement of the antenna gain and radiation efficiency [39]–[45]. The reasons why the gain of planar printed antennas is enhanced when the antenna is covered by a superstrate layer are described in the following points:

- The addition of a superstrate over radiating sources as shown in Fig. 2.1, increases the radiation aperture of the original radiating source, therefore, increases the gain of the antenna.

- The theory behind gain enhancement of planar printed antennas in the presence of superstrates will be theoretically studied in depth in this chapter (3) using the reciprocity theorem and the cavity model; furthermore, the transmission line analogy will be used to show that very high gain can be achieved if the multilayered structure (antenna with superstrate(s)) has resonant thickness of each layer and the superstrate has very high characteristic impedance ($\sqrt{\mu/\epsilon}$).

Several configurations of superstrates were used to improve antenna radiation properties (see Fig. 1.1), such as dielectric slabs [46, 47], electromagnetic bandgap (EBG) structures [14], and highly-reflective surfaces [45].

To analyze the composite structure (antenna with superstrate), full-wave electromagnetic simulation tools (HFSS, CST, COMSOL,....., etc.) which utilize numerical methods are usually used. However, using numerical methods to analyze metamaterials, or periodic structures in general, is an expensive computational task which requires considerable computer resources. The primary reason for such large computational burden is the resolution needed to capture the quasi-static resonance behavior in the metamaterial particles which are electrically very small. Therefore, numerical methods may not be practical for real-world designs that require many runs for optimization. Developing a fast analytical method to analyze such structures, which is the focus of this work, can accelerate the design process.

So far several analytical methods for calculating the far-field of Hertzian dipole in multi-layer structure has been reported in the literature [8, 9], [39]–[44]. In [9], Green's
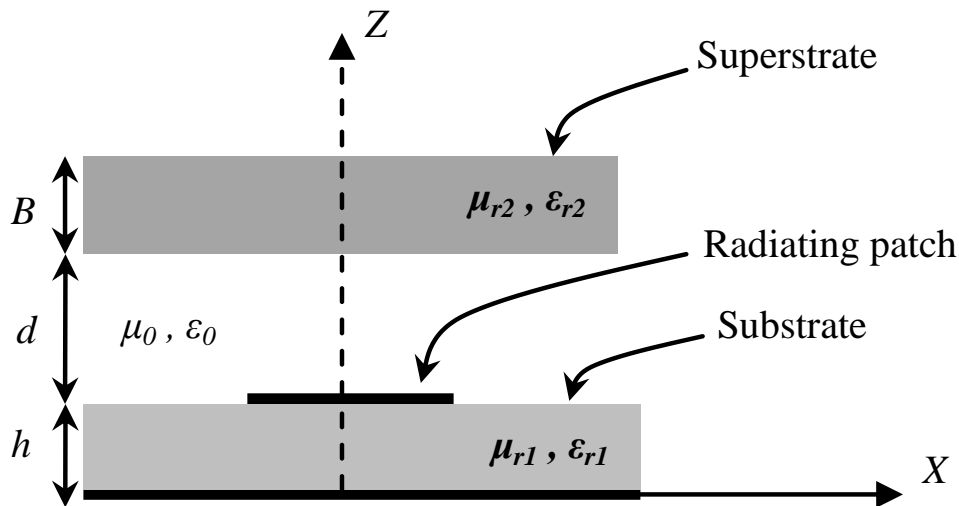
Figure 2.1: Microstrip patch antenna covered by a superstrate.

function and the stationary phase integration approach were used to calculate the gain of an infinitesimal dipole embedded in the top layer of a two-layer dielectric structure. Additionally, in [9], it was shown that a resonance condition may be created, whereby gain and radiation resistance are improved over a significant bandwidth. Later in [8], the reciprocity theorem and transmission line (TL) analogy were used to provide asymptotic formulas for gain and beamwidth of a Hertzian dipole embedded within a grounded substrate and covered with a superstrate. In [42, 43], the TL analogy method was used to compute the radiation patterns of arbitrarily directed simple dipole source that is embedded in a multilayered dielectric structure. Also, a dielectric resonator antenna covered with plain dielectric superstrate was analyzed [42]. The straightforward method proposed in this chapter, based on the cavity model, avoids the need to use the particle swarm optimization (PSO) method used in [42] to obtain a set of Hertzian dipoles representing the antenna to be analyzed using the reciprocity theorem and TL analogy.

Although several attempts have been reported to develop analytical methods, most of those works consider the case of a simple infinitesimal dipole antenna covered with plain dielectric superstrate [39]–[44]. In this work, we consider a practical microstrip patch antenna working in the UMTS band and covered with an artificial magnetic (metamaterial) superstrate used for increasing the antenna directivity. The cavity model of a MPA in conjunction with the reciprocity theorem and the transmission line analogy is used to develop a

fast analytical solution for the radiation field. The artificial superstrate constituted by split ring resonators SRR printed on both sides of a dielectric slab is characterized analytically and numerically by obtaining its effective permeability and permittivity.

The organization of this chapter is as follows: in Section (2.2), the radiation patterns of a MPA covered with a generalized superstrate layer at some distance in free space are calculated by replacing the MPA with two magnetic current sources based on the cavity model and then using reciprocity theorem and the TL analogy to compute the antenna directivity. In Section (2.3), the proposed analytical formulation is verified through a comparison with numerical full-wave simulation results, where the directivity of a MPA covered with different conventional superstrates is calculated.

2.2 Analytical Formulation of the Antenna Far-Field

The basic problem to be studied is shown in Fig. 2.1. A MPA of dimensions $(a \times b)$ is covered with a superstrate layer at a distance d in free space. The MPA is printed on a grounded substrate of thickness h having relative permeability and permittivity of μ_{r1} and ϵ_{r1}, respectively. At distance d from the substrate is the superstrate layer of thickness B having relative permeability and permittivity of μ_{r2} and ϵ_{r2}, respectively. To compute the far-field, first the MPA is modeled as a dielectric-loaded cavity [48]–[51], then the reciprocity theorem and the transmission line analogy are applied to the whole structure (antenna with the superstrate).

2.2.1 Reciprocity Theorem

Assume $\mathbf{J}_1$, $\mathbf{M}_1$ and $\mathbf{J}_2$, $\mathbf{M}_2$ are two groups of sources radiating inside the same medium generating the fields $\mathbf{E}_1$, $\mathbf{H}_1$, and $\mathbf{E}_2$, $\mathbf{H}_2$, respectively. The sources and fields satisfy the *Lorentz Reciprocity Theorem* in integral form [52]

$$\iint_{s} [\mathbf{E}_2 \times \mathbf{H}_1 - \mathbf{E}_1 \times \mathbf{H}_2].d\mathbf{s} = \iiint_{v} [\mathbf{E}_1 \cdot \mathbf{J}_2 + \mathbf{H}_2 \cdot \mathbf{M}_1 - \mathbf{E}_2 \cdot \mathbf{J}_1 - \mathbf{H}_1 \cdot \mathbf{M}_2] \, dV \quad (2.1)$$

In order to use the reciprocity theorem to compute the radiation field of MPA, one needs to consider the fields $(\mathbf{E}_1, \mathbf{H}_1, \mathbf{E}_2, \mathbf{H}_2)$ and the sources $(\mathbf{J}_1, \mathbf{M}_1, \mathbf{J}_2, \mathbf{M}_2)$ inside a medium

that is surrounded by a sphere of infinite radius. Hence, the left side of (2.1) is essentially zero and (2.1) is reduced to

$$\iiint_v [\mathbf{E}_1 \cdot \mathbf{J}_2 + \mathbf{H}_2 \cdot \mathbf{M}_1 - \mathbf{E}_2 \cdot \mathbf{J}_1 - \mathbf{H}_1 \cdot \mathbf{M}_2] \, dV = 0 \qquad (2.2)$$

According to (2.2), two problems need to be established. In the first problem, the original radiating patch at $z = h$ is replaced with an electric current source $\mathbf{J}_1$ and/or a magnetic current source $\mathbf{M}_1$ (using the cavity model [48]) radiating an electric field of $\mathbf{E}_1$ and $\mathbf{H}_1$ at the observation point of $P(r, \theta, \phi)$. In the second problem, a fictitious dipole (reciprocity source) of $\mathbf{J}_2$ (choosing $\mathbf{M}_2$ is equal to zero) at the same observation point radiates a far-field of $\mathbf{E}_2$ and $\mathbf{H}_2$ at the original patch location at $z = h$. Our goal is to use (2.2) to formulate the far-field of the MPA as $\mathbf{E}_1$.

2.2.2 Cavity Model of Microstrip Antenna

In order to use (2.2) to compute the far-field of the MPA loaded with a generalized super-strate, the MPA should be replaced by a set of electric and/or magnetic current sources. The cavity model [48] of MPA is used here to determine these equivalent currents.

The volume bound by the microstrip patch (located in the x-y plane at $z = h$) and the ground plane can be modeled as a dielectric-loaded cavity resonator by considering the top and bottom walls of this volume as perfect electric conductor (PEC) and the four side walls as ideal open circuit (magnetic walls). The mode of concern here is the dominant transverse magnetic mode (TM_{10}) which assumes a zero value of H_z but a non-zero value of E_z. By using the expression of E_z under ideal magnetic side walls boundary condition, one can formulate the equivalent magnetic current in the cavity's apertures (side walls) using the equivalence principle as $-\hat{\boldsymbol{n}} \times \boldsymbol{E}$. The resultant magnetic currents $\mathbf{M}_{1a}$ and $\mathbf{M}_{1b}$ will be y-directed on the two cavity's side walls parallel to the y-z plane as shown in Fig. 2.2. The equivalent electric current is very small (ideally zero) because $\hat{\boldsymbol{n}} \times \boldsymbol{H} = 0$ on the side walls. Hence, $\mathbf{J}_1$ in (2.2) is equal to zero.

To validate the cavity model concept of MPA and to have more physical insight. The numerical simulation tool HFSS based on the finite element method was used to plot the electric field vector on the four side walls of the box formed by the patch antenna and
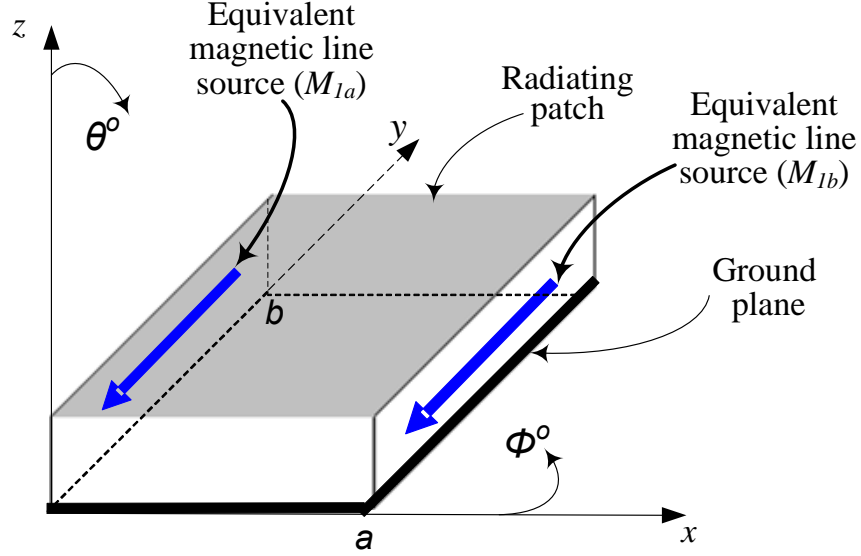
Figure 2.2: Equivalent magnetic current sources representing the patch antenna.

the ground plane (with substrate in between) as shown in Fig. 2.3. It is obvious that the radiation is much larger through only two side walls where the equivalent magnetic currents exist (in y-direction).

2.2.3 Formulating the Antenna Far-field

According to the reciprocity theorem, a fictitious dipole (reciprocity source) of $\mathbf{J}_2$ (choosing $\mathbf{M}_2$ = zero) at the observation point $P(r, \theta, \phi)$ is considered to radiate a far-field of $\mathbf{H}_2$ and $\mathbf{E}_2$ at the patch antenna location at $z = h$. Hence, equation (2.2) reduces to

$$\iiint_v [\mathbf{E}_1 \cdot \mathbf{J}_2] \, dV = - \iiint_v [\mathbf{H}_2 \cdot \mathbf{M}_1] \, dV \tag{2.3}$$

The reciprocity source is assumed to have a value of $\mathbf{J}_2 = \delta(\overrightarrow{\mathbf{r}} - \overrightarrow{\mathbf{r}_p}) \cdot \widehat{u}$ where $\widehat{u} = \widehat{\theta}$ for TM (parallel polarization) and $\widehat{u} = \widehat{\phi}$ for TE (perpendicular polarization) incident wave on the whole structure (the patch antenna with the superstrate). Hence, equation (2.3) reduces to

16
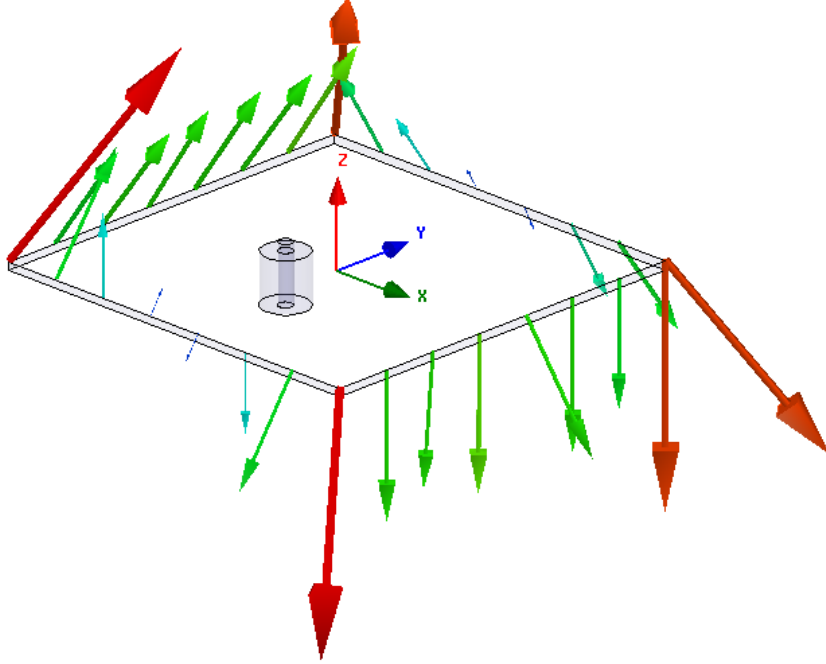
Figure 2.3: Electric field vectors on the four sides (slots) of the box formed by the patch antenna and its ground plane.

$$\mathbf{E}_1(\overrightarrow{r_p}).\widehat{u} = -\iiint\limits_{v} [\mathbf{H}_2 \cdot \mathbf{M}_1] \, dV \tag{2.4}$$

The above equation will be used to obtain the radiation field $\mathbf{E}_{1a}$ due to one of the two equivalent magnetic current sources which can be the one at the radiation slot $x = 0$ (i.e. $\mathbf{M}_{1a}$). Then, by treating the two identical radiation slots (at $x = 0$ and $x =$ a) as a two-element array, the array factor can be used to calculate the total radiated field $\mathbf{E}_1$ of the MPA covered with the superstrate, with the assumption that the existence of the superstrate does not considerably affect the current distributions in those two radiation slots.

It is observed from (2.4) that the $\mathbf{H}_2$ field is determined at the magnetic current source location (i.e. $\mathbf{M}_1$) due to the reciprocity source at the observation point $P(r, \theta, \phi)$ in either $\widehat{\theta}$ or $\widehat{\phi}$ direction. From the reciprocity theorem, $\mathbf{H}_2$ is proportional to the required radiation field $\mathbf{E}_1(\overrightarrow{r_p})$ due to the original patch antenna at $z = h$. The $\mathbf{H}_2$ field near the multilayered
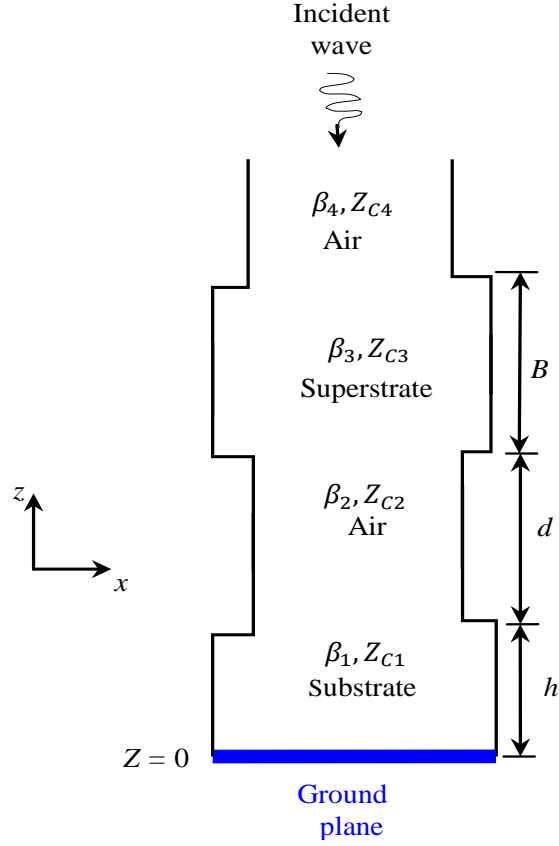
Figure 2.4: Transmission line equivalent model of the structure of Fig. 2.1.

structure due to this reciprocity source is essentially a plane wave, and therefore can be found at the $\mathbf{M}_{1a}$ location by modeling each layer as a transmission line segment (see Fig. 2.4) having a characteristic impedance and propagation constant which depend on the incident angle of θ. The propagation constants and the characteristic impedances of the multi-section transmission line equivalent model shown in Fig. 2.4 are derived from the oblique incidence of a plane wave (see Fig. 2.5) on a plane interface between two dielectric regions [53] as follows:

$$\beta_1 = K_o\sqrt{\mu_{r1}\epsilon_{r1} - \sin^2(\theta)}, \quad \beta_2 = K_o\cos(\theta) \tag{2.5}$$

$$\beta_3 = K_o\sqrt{\mu_{r2}\epsilon_{r2} - \sin^2(\theta)}, \quad \beta_4 = K_o\cos(\theta) \tag{2.6}$$
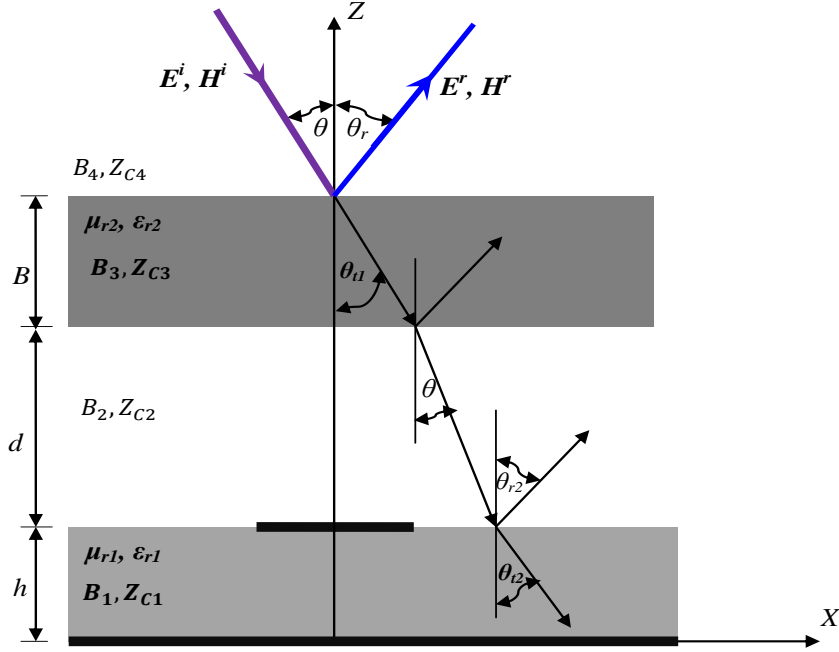
Figure 2.5: Plane wave incidence from the reciprocity source on the superstrate-substrate structure.

For TE wave or perpendicular polarization:

$$Z_{c1} = \frac{\eta_o \mu_{r1}}{\sqrt{\mu_{r1}\epsilon_{r1} - \sin^2(\theta)}}, \quad Z_{c2} = \eta_o \sec(\theta) \tag{2.7}$$

$$Z_{c3} = \frac{\eta_o \mu_{r2}}{\sqrt{\mu_{r2}\epsilon_{r2} - \sin^2(\theta)}}, \quad Z_{c4} = \eta_o \sec(\theta) \tag{2.8}$$

For TM wave or parallel polarization:

$$Z_{c1} = \frac{\eta_o \sqrt{\mu_{r1}\epsilon_{r1} - \sin^2(\theta)}}{\epsilon_{r1}}, \quad Z_{c2} = \eta_o \cos(\theta) \tag{2.9}$$

$$Z_{c3} = \frac{\eta_o \sqrt{\mu_{r2}\epsilon_{r2} - \sin^2(\theta)}}{\epsilon_{r2}}, \quad Z_{c4} = \eta_o \cos(\theta) \tag{2.10}$$

where, $K_o = \omega\sqrt{\mu_o\epsilon_o}$, $\eta_o = \sqrt{\mu_o/\epsilon_o}$

19
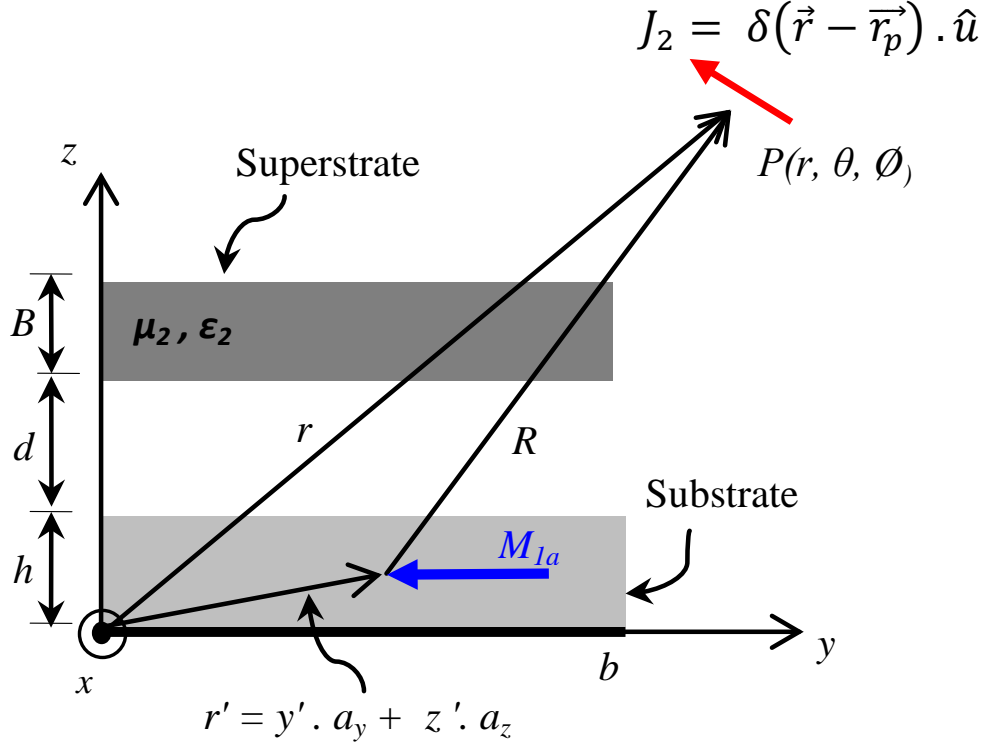
Figure 2.6: Coordinate system for computing far-field from the reciprocity electric source J_2 at the patch antenna's radiation slot located at $x = 0$.

In case of TE incident wave $(\hat{u} = \widehat{\phi})$ from the reciprocity source (infinitesimal dipole) located at the observation point $P(r, \theta, \phi)$ (see Fig. 2.6), the magnetic vector potential due to this source is equal to

$$\overrightarrow{A} = \frac{\mu_o e^{-jK_o r}}{4\pi r} \widehat{\phi} \tag{2.11}$$

Hence, the far fields of the reciprocity source are expressed as

$$E_r = -j\omega A_r = 0, \quad E_\theta = -j\omega A_\theta = 0, \quad E_\phi = -j\omega A_\phi = -j\omega\mu_o \frac{e^{-jK_o r}}{4\pi r}$$

$$\overrightarrow{H} = \frac{\widehat{r}}{\eta_o} \times \overrightarrow{E}$$

$$H_r = H_\phi = 0, \quad H_\theta = \frac{j\omega\mu_o}{\eta_o} \frac{e^{-jK_o r}}{4\pi r} \tag{2.12}$$

According to (2.4), the magnetic field due to the reciprocity source H_2 should be expressed

in y-direction to comply with the direction of $\mathbf{M}_1$. Hence, the y-component of the magnetic field due to the reciprocity source would be (note the replacing of $\omega\mu_o/\eta_o$ by K_o)

$$H_{2y} = \frac{jK_o}{4\pi}\frac{e^{-jK_oR}}{r}\sin(\phi)\cos(\theta) \tag{2.13}$$

To include the effect of the multi-layered structure (antenna with superstrate) on the magnetic field radiated by the reciprocity source, the following formula for H_{2y} at the location of $\mathbf{M}_{1a}$ can be used

$$H_{2y} = \frac{jK_o}{4\pi}\frac{e^{-jK_or}}{r}e^{jK_o(y'\sin(\theta)\sin(\phi)+z'\cos(\theta))}\sin(\phi)N(\theta) \tag{2.14}$$

The function $N(\theta)$ depends on θ only and it represents the current at $z = h$ / 2 (as midpoint in the radiation slot at $x = 0$) in the transmission line analogy (Fig. 2.4) due to an incident current wave of strength $\cos(\theta)$.

A straightforward method to determine the current at $z = h/2$ and, therefor, $N(\theta)$ is to define the voltage and current on each transmission line segment shown in Fig. 2.4 as

$$V_i = V_i^+ e^{-j\beta_i z} + V_i^- e^{j\beta_i z} \tag{2.15}$$

$$I_i = \frac{1}{Z_{ci}}(V_i^+ e^{-j\beta_i z} - V_i^- e^{j\beta_i z}) \tag{2.16}$$

where $i \in [1,N]$ is the transmission line segment number. In the model considered here, $N = 4$. Note that as the substrate of the MPA is backed by a ground plane, $V_1^+ = - V_1^-$. Also, $V_4^+/Z_{c4} = \cos(\theta)$ for the TE case. Then, by enforcing the continuity of the voltages and current at the boundaries of these transmission line segments, one can calculate all the unknown parameters (V_i^+ and V_i^-) and hence solve for the required current at $z = h/2$. This straightforward method is extendable easily to the case of MPA covered with any number of layers.

Substituting H_{2y} from (2.14) in (2.4), the far-field $E_{1a}.\widehat{\phi}$ due to the radiation slot at $x = 0$ can be calculated. Note that the volume integration in (2.4) will be converted into surface integration due to the fact that the current M_1 has a surface current distribution as shown in Fig. 2.6. Due to the length and straightforward nature of the derivation; only the final result is given here as follows:

$$E_{1a}.\widehat{\phi} = \frac{jV_oK_obe^{-jK_or}}{2\pi r}e^{j(Y+Z)}\frac{\sin Y}{Y}\frac{\sin Z}{Z}\sin(\phi) \ N(\theta) \tag{2.17}$$

where,

$$
\begin{aligned}
Y &= \frac{K_ob}{2}\sin(\theta)\sin(\phi) \\
Z &= \frac{K_oh}{2}\cos(\theta) \\
V_o &= -h \ M_{1a}
\end{aligned}
\tag{2.18}
$$

where b is the patch dimension in the y-direction (see Fig. 2.2). Note that for $h \lll \lambda$, $\frac{\sin Z}{Z} \cong 1$.

Similarly, the far field due to the other radiation slot at $x = a$ can be obtained. By adding the fields due to the two radiation slots together, the total field (in the ϕ direction) due to the MPA covered with the superstrate can be obtained. Another interesting way to compute the total field of the MPA in the TE mode is treating the two identical radiation slots (at $x = 0$ and a) as a two-element array. Hence, the array factor can be used to calculate the total radiated field E_ϕ of the MPA covered with the superstrate. Adopting the latter method, the total field can be formulated as

$$E_\phi = \frac{jV_oK_obe^{-jK_or}}{\pi r}e^{j(X+Y+Z)}\cos X\frac{\sin Y}{Y}\sin(\phi) \ N(\theta) \tag{2.19}$$

where,
$$X = \frac{K_o \ a}{2}\sin(\theta)\cos(\phi) \tag{2.20}$$

where a is the patch dimension in x-direction (see Fig. 2.2).

Similarly, in the case of TM incident wave ($\widehat{u} = \widehat{\theta}$) from the reciprocity source located at the observation point $P(r, \theta, \phi)$ (see Fig. 2.6), the total radiated field E_θ of the MPA covered with the superstrate can be formulated as

$$E_\theta = -\frac{jV_oK_obe^{-jK_or}}{\pi r}e^{j(X+Y+Z)}\cos X\frac{\sin Y}{Y}\cos(\phi) \ Q(\theta) \tag{2.21}$$

The function $Q(\theta)$ depends on θ only and it represents the current at $z = h \ / \ 2$ (as midpoint in the radiation slot at $x = 0$) in the transmission line analogy (Fig. 2.4) due

22

to an incident current wave of strength 1 A. Hence, $V_4^+/Z_{c4} = 1$ in the transmission line equivalent model (Eqs (2.15) and (2.16)). The function $Q(\theta)$ can be computed in the same way explained earlier in the case of $N(\theta)$.

Interestingly, the closed forms for the far-field given by (2.19) and (2.21) agree well with the ones calculated using the conventional vector potential approach [50] (see Eqs (45) and (46) in [50]) when the superstrate is air (i.e. patch antenna in free space) where $N(\theta)$ = $\cos(\theta)$ and $Q(\theta) = 1$, this agreement verifies the accuracy of the proposed analytical formulation. However, the vector potential approach [50] works only for a patch antenna in free space.

The far-field of the MPA covered with the superstrate is calculated at the desired frequency using (2.19) and (2.21), and integrated as follows to calculate the antenna directivity:

$$Directivity(\theta, \phi) = \frac{4\pi * F}{\int_0^{2\pi} \int_0^{\frac{\pi}{2}} F * \sin(\theta) d\theta d\phi} \tag{2.22}$$

where,

$$F = \cos^2(X)\frac{\sin^2(Y)}{Y^2} * (\sin^2(\phi)|N(\theta)|^2 + \cos^2(\phi)|Q(\theta)|^2)$$

2.3 Radiation due to a Patch Antenna Covered with Conventional Superstrate

In this section, the radiation patterns of a patch antenna covered with a conventional superstrate is investigated using the analytical technique explained in the previous section and verified using the commercial full-wave simulator HFSS.

In accordance with Fig. 2.1, assume a MPA having dimensions of 36 mm x 36 mm, and printed on a substrate of Rogers RO4350 having a relative permittivity of 3.48, loss tangent of $tan\delta = 0.004$ and a thickness of 0.762 mm. The patch is covered with a superstrate of thickness 6.286 mm. The spacing between the antenna and the superstrate is 12 mm. The three-layer radiating system is infinitely extended in the x-y plane to comply with the

transmission line analogy in order to calculate the current at the patch location due to the TE and TM incident plane waves.

Three superstrates with different values of permeability (μ_{r2}) and permittivity (ϵ_{r2}) are studied here. The 2-D radiation patterns shown in Figs. 2.7, 2.8 for (μ_{r2}= 1, ϵ_{r2} = 1), Figs. 2.9, 2.10 for (μ_{r2}= 16, ϵ_{r2} = 1), and Figs. 2.11, 2.12 for (μ_{r2}= 1, ϵ_{r2} = 6). It is observed that the resultant E-plane ($\phi = 0^o$) and H-plane ($\phi = 90^o$) directivity radiation patterns agree well with the HFSS results in the three cases. The discrepancies noticed between the two methods in Figs. 2.9 and 2.11 near the azimuthal plane are due to the fact that the analytical method assumes infinite ground plane.

Fig. 2.13 shows a comparison between the analytically and numerically (HFSS) calculated directivity in broadside direction ($\phi = \theta = 0^o$) at 2.2 GHz of the patch antenna covered with a superstrate having a relative permeability μ_{r2} of 1 and varying relative permittivity ϵ_{r2}. Good agreement is observed between the two methods.
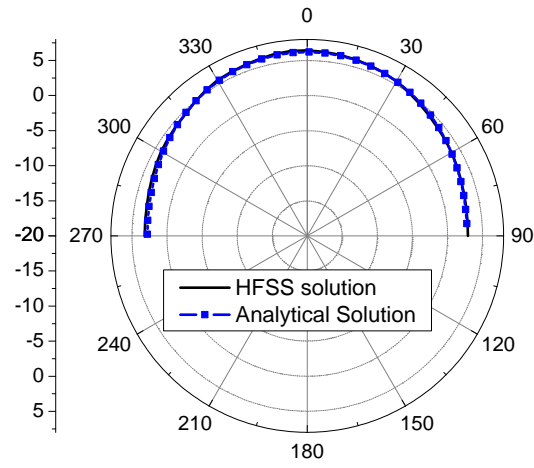
Figure 2.7: The E-plane directivity radiation pattern at 2.2 GHz of the patch antenna covered with a superstrate ($\mu_{r2}= 1$ and $\epsilon_{r2} = 1$) at d=12 mm, B=6.286 mm and h=0.762 mm.
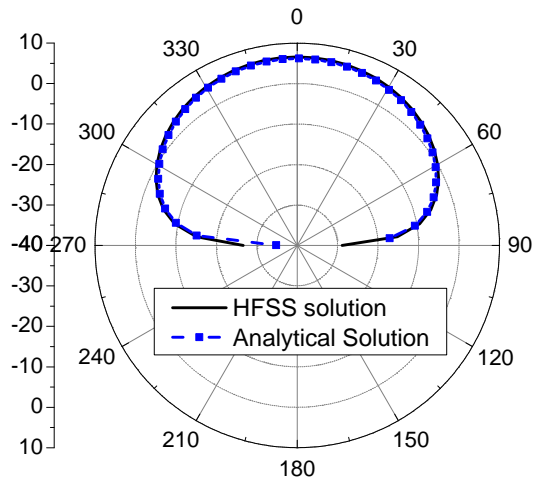
Figure 2.8: The H-plane directivity radiation pattern at 2.2 GHz of the patch antenna covered with a superstrate ($\mu_{r2}= 1$ and $\epsilon_{r2} = 1$) at d=12 mm, B=6.286 mm and h=0.762 mm.
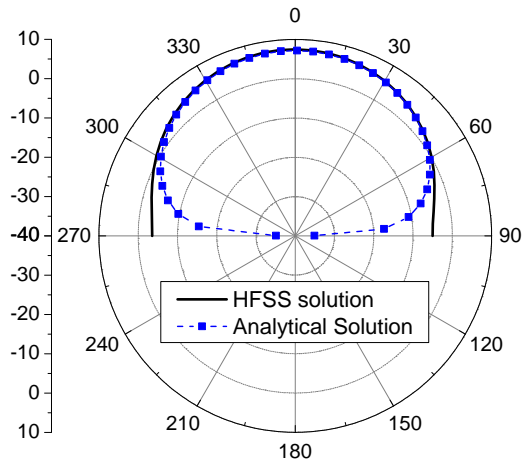
Figure 2.9: The E-plane directivity radiation pattern at 2.2 GHz of the patch antenna covered with a superstrate (μ_{r2}= 16 and $\epsilon_{r2} = 1$) at d=12 mm, B=6.286 mm and h=0.762 mm.
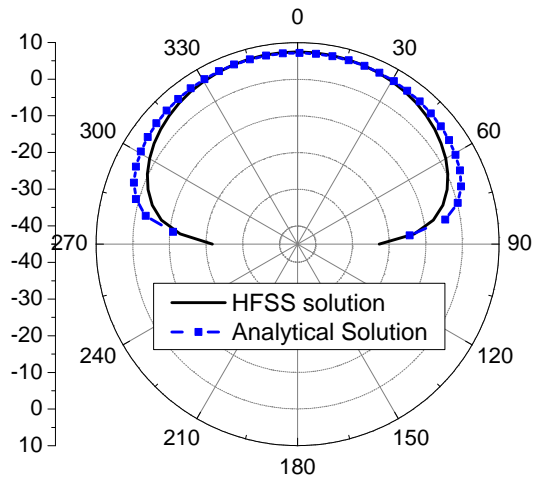
Figure 2.10: The H-plane directivity radiation pattern at 2.2 GHz of the patch antenna covered with a superstrate (μ_{r2}= 16 and $\epsilon_{r2} = 1$) at d=12 mm, B=6.286 mm and h=0.762 mm.
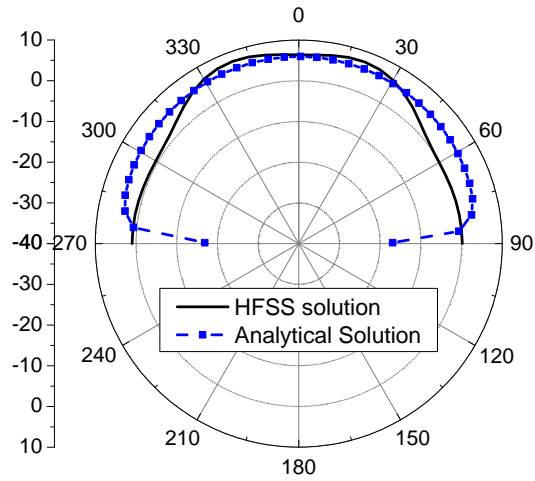
Figure 2.11: The E-plane directivity radiation pattern at 2.2 GHz of the patch antenna covered with a superstrate ($\mu_{r2}= 1$ and $\epsilon_{r2} = 6$) at d=12 mm, B=6.286 mm and h=0.762 mm.
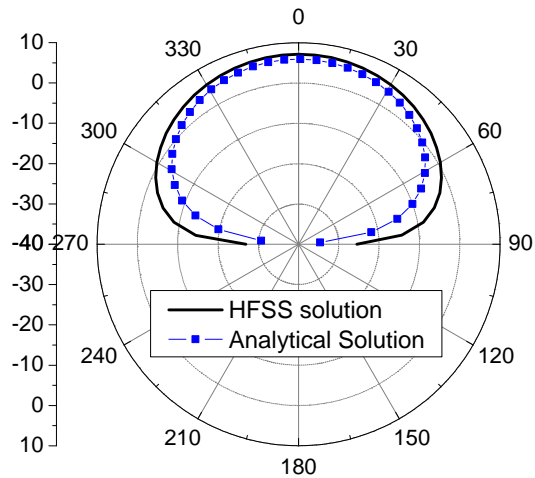
Figure 2.12: The H-plane directivity radiation pattern at 2.2 GHz of the patch antenna covered with a superstrate ($\mu_{r2}= 1$ and $\epsilon_{r2} = 6$) at d=12 mm, B=6.286 mm and h=0.762 mm.
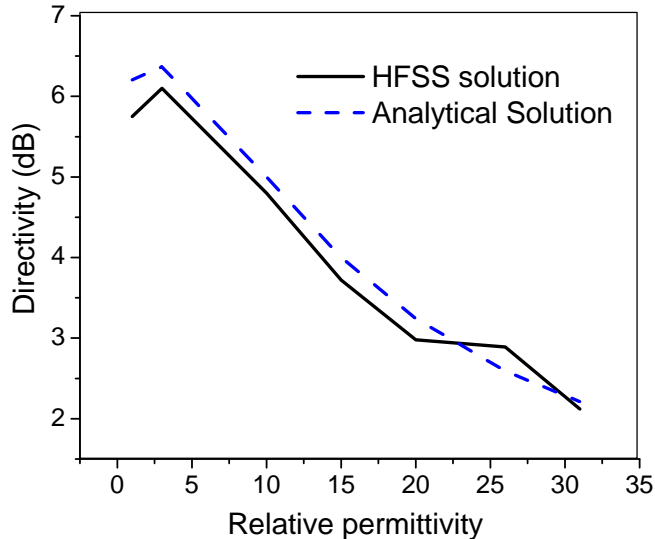
Figure 2.13: The directivity of MPA shown in Fig. 1 versus the relative permittivity of the superstrate with $\mu_{r2}= 1$ at 2.2 GHz, d=12 mm, B=6.286 mm and h=0.762 mm.

2.4   Conclusions

A fast and accurate analytical technique was developed to calculate the radiation field of a microstrip antenna covered with a generalized superstrate. The analytical formulation is based on using the cavity model to replace the patch antenna by two magnetic line sources. Then, the reciprocity theorem and transmission line analogy were used to calculate the far-field of these two magnetic line sources representing the patch antenna. The proposed analytical model was implemented and verified by a comparison with a full-wave simulator for the case of patch antenna covered with different conventional superstrate layers.

The analytical formulation introduced here can be extended for the case of a patch antenna embedded in a multilayered dielectric structure. We emphasize that the analytical method presented in this work is not restricted to the case of isotropic conventional superstrate, and can be used for analysis of any superstrate made of engineered periodic structures (positive or negative permeability and/or permittivity) as the next chapters will show.

Chapter 3

Resonance Conditions for High Gain Microstrip Antennas Loaded with High Characteristic Impedance Superstrates

3.1   Introduction

It is shown that, under some resonance conditions, a microstrip patch antenna can be designed to achieve the highest possible gain and directivity when covered with a superstrate at the proper distance in free space. The transmission line model presented in the previous chapter is employed herein to analytically derive the resonance conditions required to achieve the highest directivity of the antenna with superstrate. These resonance conditions include the condition on spacing between the antenna substrate and the superstrate and the thickness of the superstrate. The permeability and permittivity of the superstrate is determined based on these resonant lengths and the appropriate characteristic impedance of each layer in this multilayered structure. The results are verified using both analytical and numerical methods. The effect of anisotropy of the superstrate is numerically investigated. The design criteria proposed here will reduce the total profile of the radiating system by 50% when compared with previous techniques [14, 45].

29

In all different configurations of antenna-superstrate structures [39]–[45], the substrate-superstrate spacing and the thickness and nature of the superstrate(s) affect the value of the antenna gain significantly and also the shape of the radiation pattern. Therefore, proper determination of these parameters could produce the highest possible gain of a patch antenna when the multilayered structure (antenna with superstrate(s)) is treated as a multi-section transmission line with resonant lengths. Using full-wave numerical electromagnetic simulation tools, to analyze and optimize a patch antenna with artificial periodic (metamaterial) superstrate, is a very expensive computational task [14]. Therefore, these techniques may not be used to optimize the structure for maximum gain. On the other hand, adopting the analytical technique explained in the previous chapter would reduce the optimization time significantly.

In this chapter, the multilayered structure (antenna with superstrate) is treated as a multi-section transmission line with resonant lengths. The transmission line approximations and the cavity model of a patch antenna are used to derive the resonance conditions for a patch antenna with superstrate to achieve the highest possible gain and directivity. Then an antenna with superstrate is designed based on the derived resonance conditions. The analytical results for the far-field are then verified using two different numerical methods (i.e., HFSS and CST). The design criteria proposed here will reduce the total profile of the radiating system by 50% when compared with previous methods based on partially reflective superstrate [45] and conventional dielectric superstrate [46] where a half wavelength separation (in air) is required between the patch antenna and the superstrate.

3.2   Resonance Conditions for Maximum Directivity

In this section, the resonance conditions for the optimum directivity of a patch antenna covered with a superstrate (see Fig. 3.1) are derived. As shown in Fig. 3.1, a patch antenna, printed on a grounded substrate of thickness h, is covered with a superstrate layer of thickness B, at a distance d in free space. The relative permeability and relative permittivity of the substrate and superstrate, are denoted as μ_{r_1}, ϵ_{r_1}, μ_{r_2} and ϵ_{r_2}, respectively.

According to (2.4) which is repeated herein
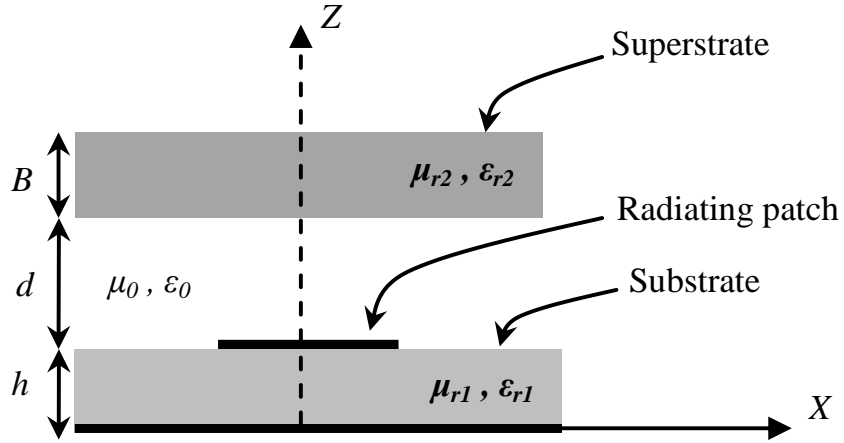
Figure 3.1: Microstrip patch antenna covered by a superstrate.

$$\mathbf{E}_1(\vec{r_p}).\hat{u} \; = \; - \iiint\limits_v \; [\mathbf{H}_2 \cdot \mathbf{M}_1] \; dV \tag{3.1}$$

It is observed from (3.1) that the $\mathbf{H}_2$ field is determined at the original patch location at $z = h$ due to the reciprocity source at the observation point $P(r,\,\theta,\,\phi)$ in either $\widehat{\theta}$ or $\widehat{\phi}$ direction. From the reciprocity theorem, $\mathbf{H}_2$ is proportional to the required radiation field $\mathbf{E}_1(\vec{r_p})$ due to the original patch antenna at $z = h$. The $\mathbf{H}_2$ field near the multilayered structure due to this reciprocity source is essentially a plane wave, and therefore can be found by modeling each layer as a transmission line segment (see Fig. 3.2(a)) having a characteristic impedance and propagation constant which depend on the incident angle of θ. Consequently, $\mathbf{H}_2$ is directly proportional to the current at $z=h$ (assuming $h \ll \lambda_o$) in the transmission line analogy (Fig. 3.2(a)) due to an incident current wave of strength $\cos(\theta)$ in the TE case and of strength one in the TM case.

Hence, in order to maximize the radiation field (Eq. 3.1) of the patch antenna with superstrate, the current at $z = h$ (see Fig. 3.2(a)) should be maximized. One way to achieve this goal is to have the substrate-superstrate spacing (d) and also the superstrate thickness (B) as *quarter wave length* in the respective medium; hence

31
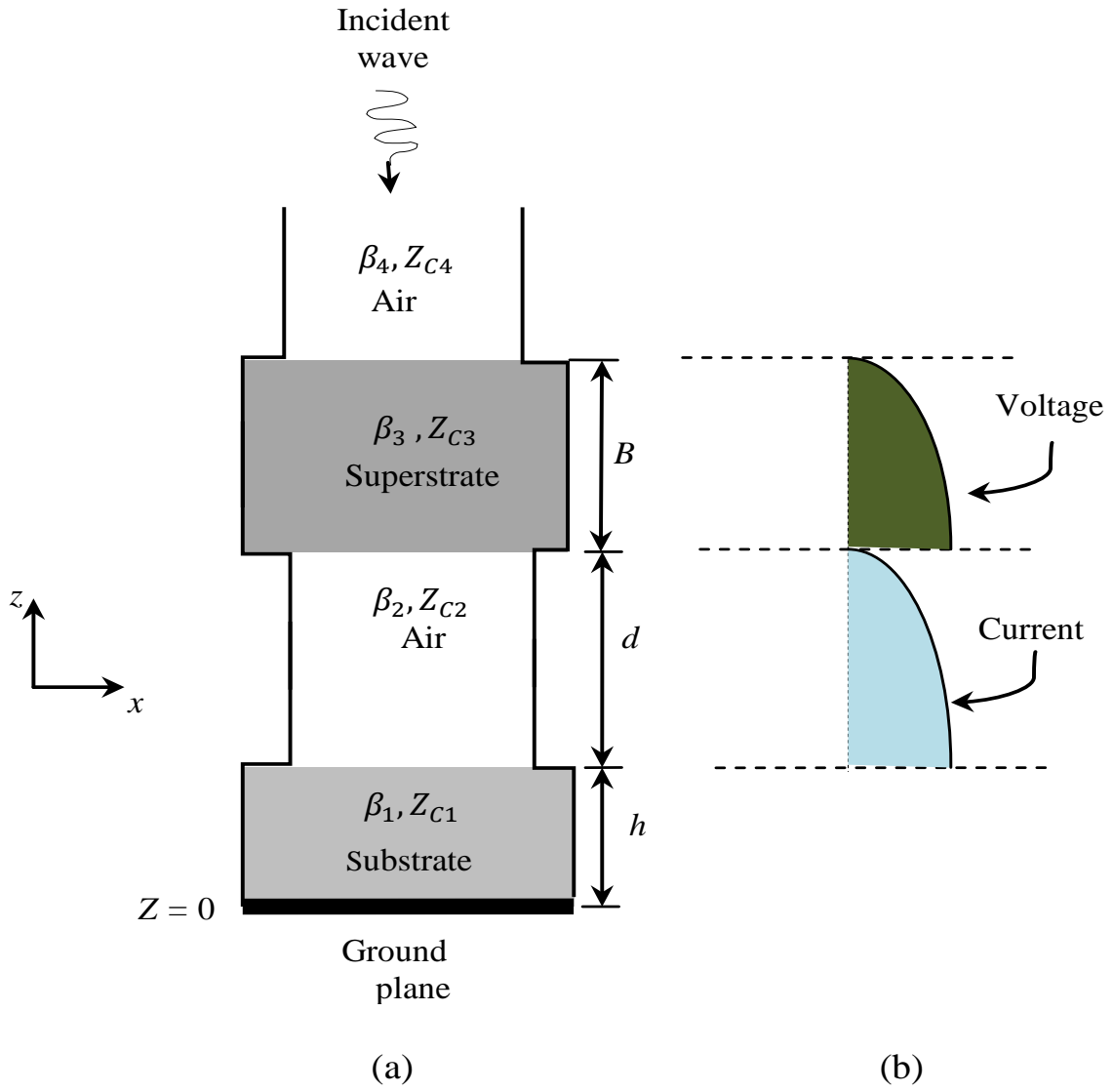
Figure 3.2: (a) Transmission line equivalent model of the structure of Fig. 3.1. (b) Voltage and current distributions on the transmission line model when d and B equal to quarter wave length in the respective medium.

$$d = \frac{\lambda_o}{4} \tag{3.2}$$

$$B = \frac{\lambda_o}{4 \times \sqrt{\mu_{r_2} \epsilon_{r_2}}} \tag{3.3}$$

Under the above resonance conditions and assuming that $h \ll \lambda_o$ (i.e. neglecting the effect of the substrate), the short circuit (ground plane) in Fig. 3.2(a) is basically at $Z = h$ and consequently the impedance at $Z = h{+}d{+}B$ would equal to zero due to the resonant lengths in the TL model. As a result, the voltage and current distributions on the TL model would be as depicted in Fig. 3.2(b) and the current is maximized at the patch location ($z = h$) as required to achieve the maximum radiated field of the patch antenna. With this in mind, the ratio μ_{r_2}/ϵ_{r_2} should be maximized so that the characteristic impedance of the superstrate will be very high causing the voltage along the superstrate section of TL model to be very high. When this large voltage wave gets injected into the air layer underneath the superstrate (i.e. at $Z = h{+}d$), it will produce a very high current inside this air layer causing the current at the patch location to be very high and hence producing a very high radiation of the patch antenna under these resonance conditions.

3.3 High Directivity Patch Antennas

In this section, the aforementioned resonance conditions for the optimum directivity are validated. The Hessian matrix (i.e., the second derivatives of the Lagrangian multipliers) method [38] is used to optimize the directivity (Eq. 2.22) of a patch antenna covered with a superstrate having arbitrary permeability μ_{r_2} and permittivity ϵ_{r_2}. Four variables were optimized subject to pre-determined constraints as shown in Table 3.1

Table 3.1: Optimization of the directivity of patch antenna covered with superstrate

Variable	Constraints	Optimized value
m	min.=1, max.=10	4.091
n	min.=1, max.=10	4.0027
μ_{r_2}	min.=1, max.=100	100
ϵ_{r_2}	min.=1, max.=20	1

where,

$$d = \lambda_o/m \ , \ B = (\lambda_o/\sqrt{\mu_{r_2} * \epsilon_{r_2}})/n$$

The optimized parameters as obtained in Table 3.1 strongly agree with the aforementioned explanation about the resonance conditions.

To apply these resonance conditions in a practical perspective and in accordance with Fig. (3.1), assuming a patch antenna working at 2.2 GHz for UMTS (Universal Mobile Telecommunication Systems) applications. The patch has dimensions of 36 mm x 36 mm and is printed on a substrate of Rogers RO4350 having a relative permittivity of 3.48, loss tangent of $tan\delta = 0.004$ and a thickness of 0.762 mm. The substrate and ground plane have equal planar size of 432 mm x 432 mm. The patch is covered with a superstrate of $\mu_{r_2} = 50$, $\epsilon_{r_2} = 1$ and planar size of 360 mm X 360 mm. The substrate-superstrate spacing (d) and the superstrate thickness (B) are equal to quarter wave length in the respective medium at 2.2 GHz. Fig. 3.3 shows the radiation patterns calculated analytically using (2.22) and verified using HFSS. As shown in Fig. 3.3, the directivity of the designed antenna under resonance conditions, is equal to 18.5 dBi which is about 13 dBi higher than the directivity of the standard patch antenna without superstrate. Also, the radiation pattern becomes much sharper around the broadside direction. The small discrepancy in Fig. 3.3 is due to the assumption that the four-layers radiating system is infinitely extended in the x-y plane to comply with the transmission line analogy in the analytical solution. On the other hand, the same radiating system has finite size when simulated using HFSS.

To do a further study on the effect of the permeability of the superstrate on the antenna directivity, Table 3.2 shows the analytically calculated directivity for different values of the relative permeability (μ_{r_2}) of the superstrate (the antenna and superstrate have the same specifications as mentioned above). It is observed that the directivity increases as μ_{r_2} increases, as concluded before, and in compliance with the resonance conditions for high radiation.

Table 3.2: Directivity of the patch antenna for different values of μ_{r_2}

| μ_{r_2}	Directivity (dBi)
1000	40.12
500	34.27
100	23.43
75	22.12
50	20.38
25	17.51
10	14.00
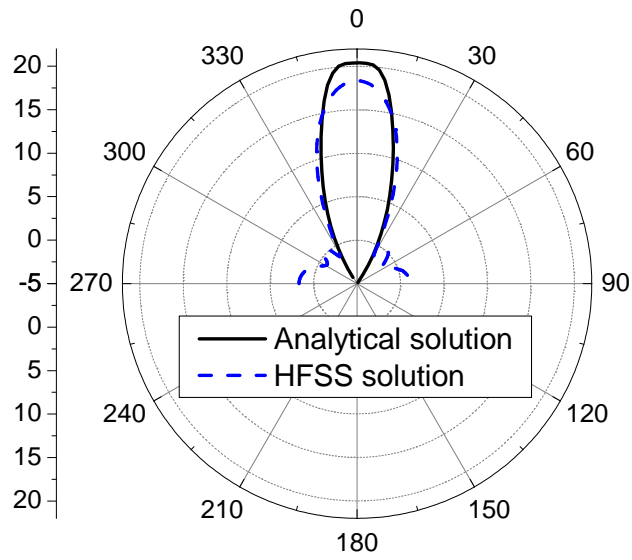
(a)
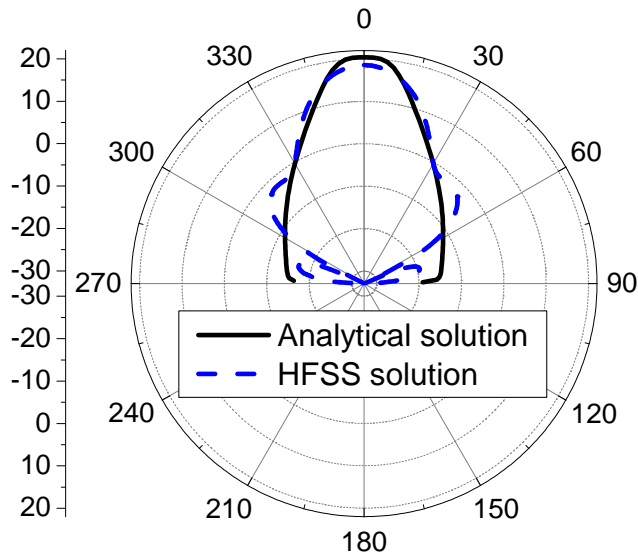
(b)

Figure 3.3: The directivity radiation pattern at 2.2 GHz of the patch antenna covered with a superstrate having $\mu_{r_2} = 50$ and $\epsilon_{r_2} = 1$ and with thickness of *quarter wave length* in the medium. (a) E-plan. and (b) H-plan.

Fig. 3.4(a) shows the variation of the radiation field at $\theta = \phi = $ o deg. of the aforementioned patch antenna covered with a superstrate of thickness $\lambda_o/(4\sqrt{\mu_{r_2}\epsilon_{r_2}})$ and placed at distance of $\lambda_o/4$ of the patch antenna. It is obvious that the radiation field increases as μ_{r_2} increases. Also, Fig. 3.4(b) shows that the optimum value of ϵ_{r_2} is unity in order to achieve the highest possible radiation field.

Another example showing the validity of the resonance conditions to increase the antenna gain is the numerical simulations of a patch antenna working at 5.8 GHz for WLAN (Wireless Local Area Network) applications. The patch has dimensions of 12.5 mm x 12.5 mm and is printed on a substrate of Rogers RO4350 having a relative permittivity of 3.48, loss tangent of $tan\delta = 0.004$ and a thickness of 0.762 mm. The substrate and ground plane have equal planar size of 125 mm x 125 mm. The patch is covered with a superstrate of $\mu_{r_2} = 50$, $\epsilon_{r_2} = 1$ and planar size of 360 mm X 360 mm. The same resonance conditions are being used here for the substrate-superstrate spacing (d) and the superstrate thickness (B).

The gain of the antenna with and without the superstrate is calculated numerically using two different software tools (i.e., HFSS and CST) and shown in Fig. 3.5. It is observed that the gain increases from 6.19 dBi to about 17 dBi after adding the superstrate with high characteristic impedance. Also, a good agreement is observed between HFSS and CST. The E-plane gain radiation pattern at 5.8 GHz is calculated using both CST and HFSS and shown in Fig. 3.6. Strong agreement is observed between the two methods and very sharp beam is achieved after applying the resonance conditions.

The radiation efficiency of the patch antenna with and without the same superstrate is calculated numerically using the same software tools and shown in Fig. 3.7. It is observed that the radiation efficiency increases by about 12% after adding the superstrate with high characteristic impedance. The enhanced efficiency is believed to be a consequence of the increase in the antenna gain due to the direct proportionality between the gain and efficiency.
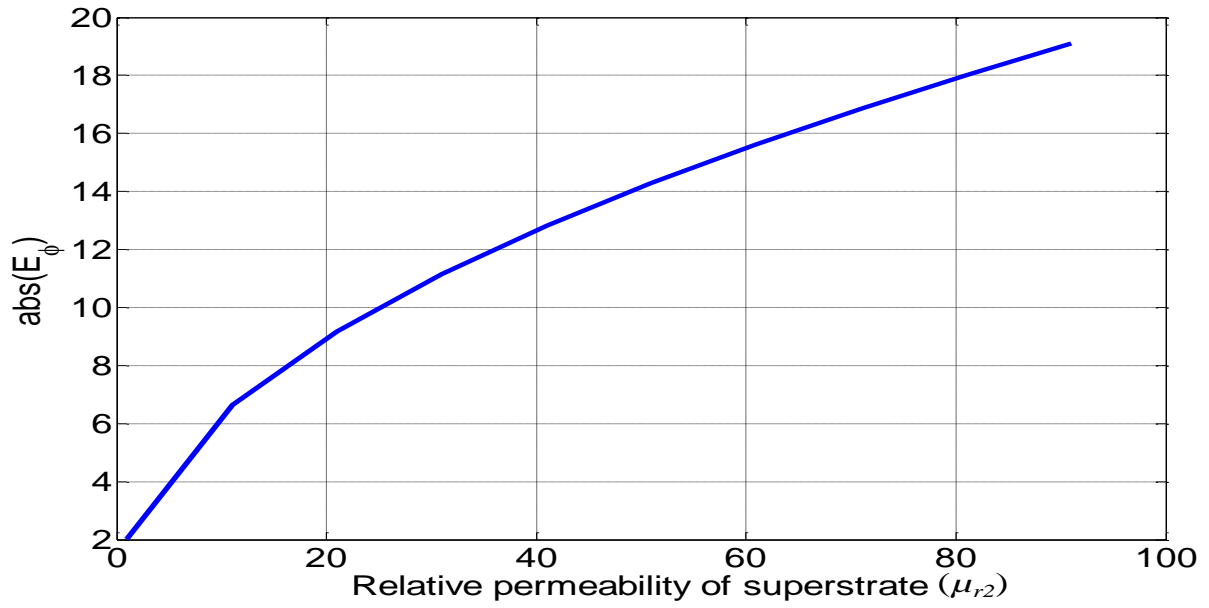
(a)
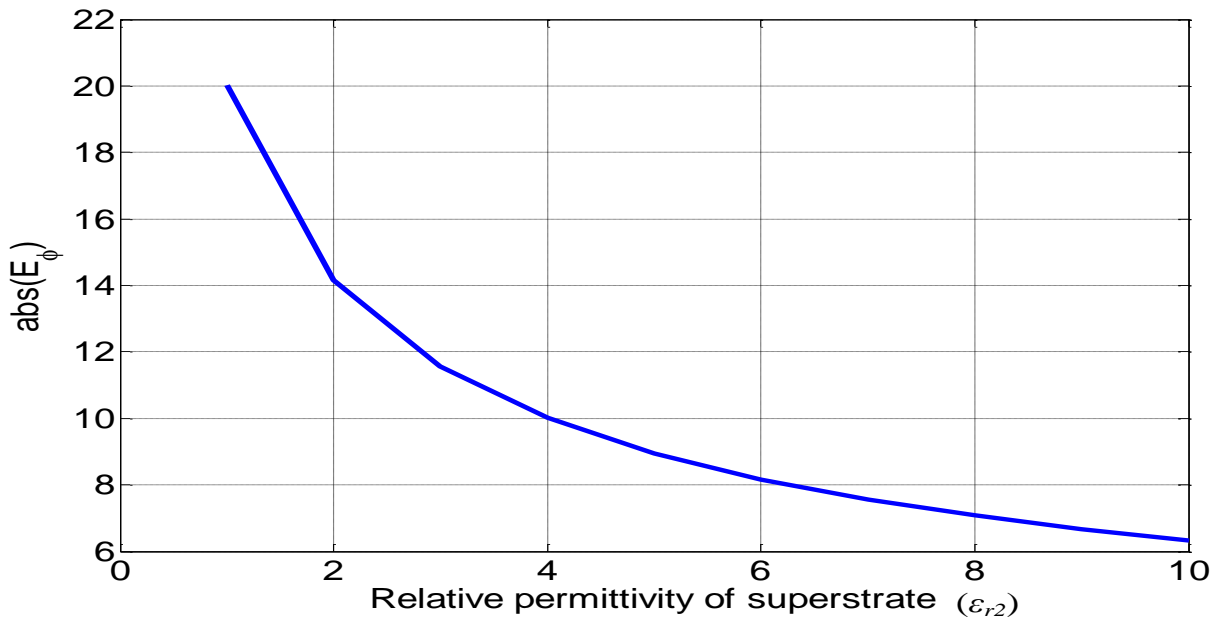
(b)

Figure 3.4: (a) The radiation field at broadside direction of the patch antenna versus μ_{r_2} when $\epsilon_{r_2} = 1$ and (b) versus ϵ_{r_2} when $\mu_{r_2} = 100$. ($d = B = \lambda/4$ in the respective medium)
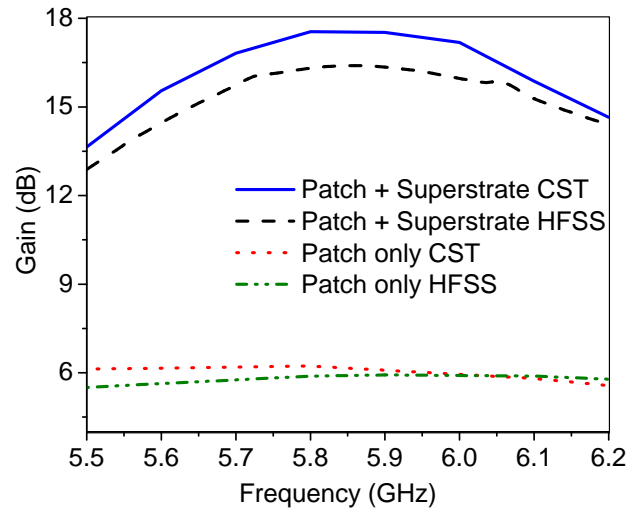
Figure 3.5: The gain of a patch antenna with and without a superstrate having $\mu_{r_2} = 50$ and $\epsilon_{r_2} = 1$ and with thickness of quarter wave length in the medium.
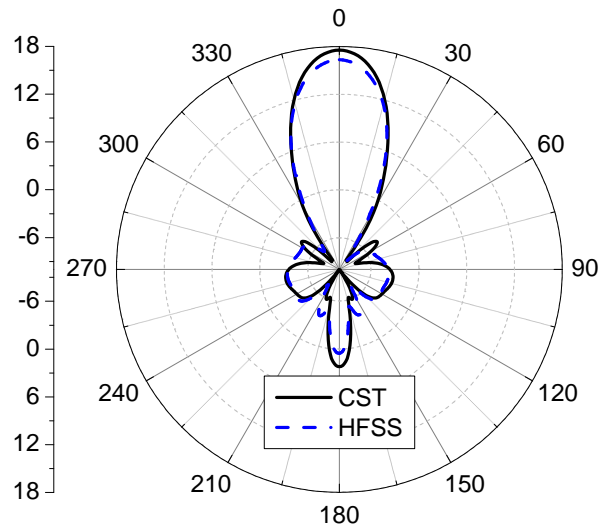
Figure 3.6: The gain radiation pattern of patch antenna with a superstrate having $\mu_{r_2} = 50$ and $\epsilon_{r_2} = 1$ and with thickness of quarter wave length in the medium at 5.8 GHz.
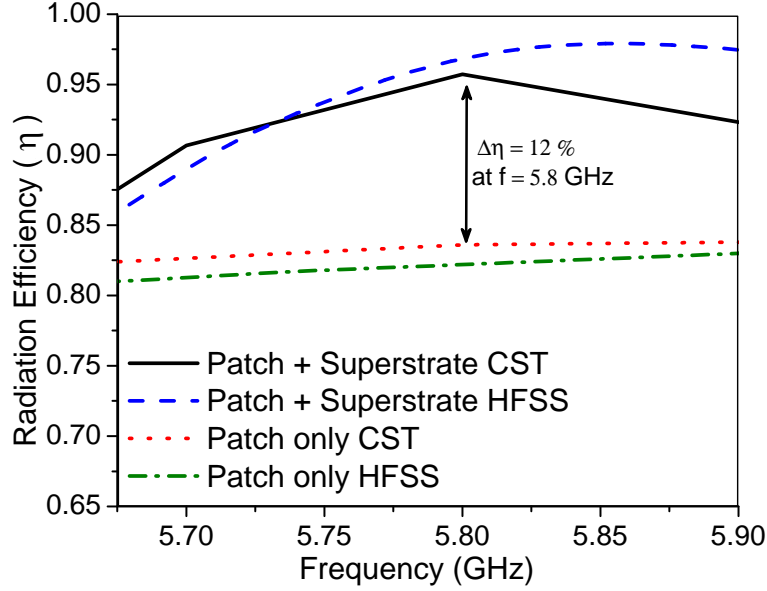
Figure 3.7: The radiation efficiency of patch antenna with a superstrate having $\mu_{r_2} = 50$ and $\epsilon_{r_2} = 1$ and with thickness of quarter wave length in the medium at 5.8 GHz.

3.4 Effects of the Anisotropy of High Permeability Superstrate

As discussed in the previous section, high-permeability superstrate is required to achieve very directive radiation from the patch antenna. Artificial magnetic structures (AMS) can be used to provide such superstrate. AMS are composed of metallic unit cells printed periodically on a dielectric material. When excited by external magnetic field, AMS provide high permeability only in the direction of the applied magnetic field and provide permeability of 1 in all other directions [33]. Due to the fact that the AMS are inherently anisotropic, it is important to study the effect of the anisotropy of the superstrate on the antenna radiation pattern and gain.

In accordance with Fig. 3.1, assume a patch working at 2.2 GHz with the same specifications as in the previous section except for the relative permeability of the superstrate (μ_{r_2}) which is assumed to have anisotropic form of

$$\overline{\overline{\mu_{r_2}}} = \begin{bmatrix} \mu_{r_x} & 0 & 0 \\ 0 & \mu_{r_y} & 0 \\ 0 & 0 & \mu_{r_z} \end{bmatrix} \quad (3.4)$$

For simplicity, assume $\mu_{r_2} = (\mu_{r_x}, \mu_{r_y}, \mu_{r_z})$.

The substrate-superstrate spacing (d) and the superstrate thickness (B) are equal to quarter wave length at 2.2 GHz in the respective medium. Fig. 3.8 shows the HFSS simulation of the gain variations for different anisotropic configurations of the superstrate. It is observed that the superstrate with high permeability in Y-direction acts similarly as the isotropic case and improves the antenna gain significantly. On the other hand, the superstrate with high permeability in either X- or Z-direction does not affect the antenna gain. Consequently, it is essential to develop AMS based superstrate with appropriate anisotropic permeability in order to achieve the highest possible gain of the whole radiating system (antenna with superstrate). Next chapter will provide the theory and development of AMS to be used as superstrates of planar antennas.

3.5   Conclusions

The transmission line analogy and the cavity model of a patch antenna were used to derive the resonance conditions for a high-gain patch antenna covered with a superstrate. The resonance conditions require that the substrate-superstrate spacing and the superstrate thickness should be equal to *quarter wave length* in the respective medium. A superstrate with very high permeability and nominal permittivity is required under these resonance conditions to achieve very high directivity. The analytical formulation for the antenna far-fields was verified using numerical methods. The significant effects of anisotropic magnetic superstrates on the antenna gain and radiation efficiency were discussed. The design criteria proposed here reduce the total profile of the radiating system by 50% when compared with previous approaches based on highly-reflective superstrate and dielectric-slab superstrate.
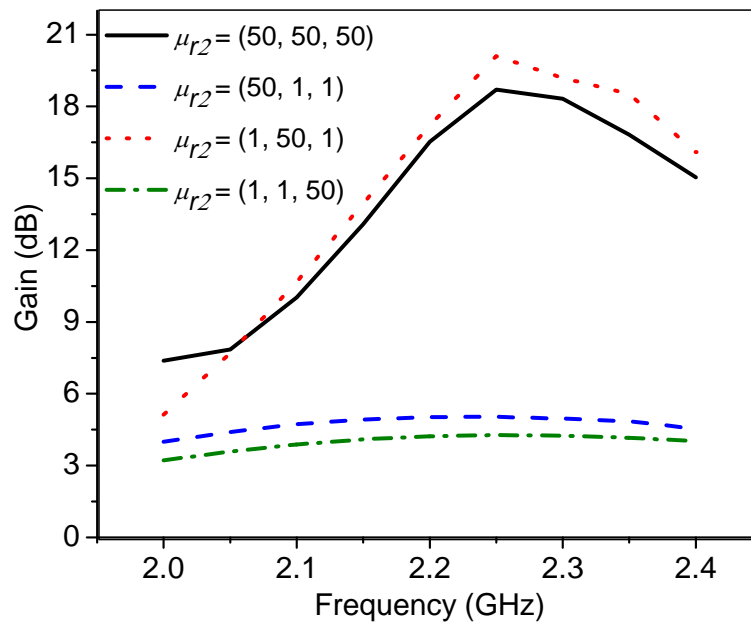
Figure 3.8: The numerically calculated gain of a patch antenna with a superstrate having anisotropic permeability and with thickness of quarter wave length in the medium.

Chapter 4

Theory and Development of Engineered Magneto-Dielectrics

4.1   Introduction

The resonance conditions derived in chapter (3) require a superstrate with very high magnetic permeability and nominal electric permittivity in order to increase the antenna directivity and gain. However, in the microwave region (f > 300 MHz), naturally occurring magnetization cannot occur in materials due to the inertia of the atomic system that is not able to track an electromagnetic field with high frequency [28]. Therefore, designing materials with magnetic properties that do not exist in naturally-occurring materials has become increasingly attractive in recent years [23]–[30]. An engineered magneto-dielectric material is composed of small metallic resonating inclusions embedded periodically into a host dielectric to achieve magnetic permeability and electric permittivity larger than that of the host medium. In this chapter, the mechanism of operation for artificial magnetic materials is theoretically investigated. Analytical and numerical methods are provided to model the behaviour of these materials to be used as superstrates for planar antennas.

Another interesting application of the engineered magneto-dielectric materials is to miniaturize planar antennas [29, 33]. The conventional method for reducing the planar antenna size was to print the antenna over a high dielectric constant substrate. But the high impedance contrast between the substrate (due to its capacitive nature) and the

surrounding free space degrades the efficiency of the radiating system. To overcome this problem, magneto-dielectrics can be used as substrates for planar printed antennas to reduce the size of these antenna without considerable reduction of the antenna impedance bandwidth [33]-[34]. In this case, the impedance mismatch is smaller leading to low losses and high efficiency of the radiating miniaturized system.

When using the magneto-dielectric materials as superstrates for planar antennas, the objective is to increase the permeability of the superstrate and to reduce its thickness and hence reduce the overall size of the composite structure (antenna with superstrate). This is because of the fact that the effective wavelength is reduced in the magneto-dielectric ($\lambda = \lambda_{air}/\sqrt{\mu_r \epsilon_r}$) due to the higher values of the magnetic permeability and electric permittivity of these artificial engineered materials. The magnetic effect in artificial magnetic materials is due to circulating currents induced on split-rings or other similar metal inclusions. These inclusions are small-sized resonators, and the frequency dispersion of their response is a very important factor that cannot be neglected even in the design of narrow-band antennas.

4.2   Magnetism in Natural Magnetic Materials

In electromagnetism, permeability is the degree of magnetization of a material that responds to an applied magnetic field. Magnetic permeability is typically represented by the Greek letter μ. The term was coined in September 1885 by Oliver Heaviside. The bulk permeability of a material is a quantitative description of how readily the material experiences magnetization, which is when an externally applied magnetic field causes the charges in a material to align their motion such that their magnetic moments align parallel or anti-parallel to the external magnetic field. Due to the absence of magnetic monopoles, magnetic fields are described by Ampere's Law as being produced by the motion of charges, either individually or in current form [54]–[57].

The magnetic flux density ($\vec{B}$) is related to the *Lorentz* force on a moving electric charge q [54]–[56]:

$$\vec{F} = q\,(\vec{V}X\vec{B}) \tag{4.1}$$

where,

$\vec{F}$ is the force (in Newtons).

$\vec{B}$ is the magnetic flux density (in teslas or webers/m²).

q is the electric charge of the particle (in coulombs).

$\vec{V}$ is the instantaneous velocity of the particle (in m/s).

By definition, electric current is the flow (movement) of electric charge. Thus, the force applied to a closed circuit carrying current I, can be obtained from integrating the force applied to small current filaments:

$$\vec{F} = I \oint (\vec{dl} X \vec{B}) \qquad (4.2)$$

Using the above equations and definition of the torque, the electromagnetic torque applied to a small closed loop carrying current I, will be equal to:

$$\vec{T} = I\vec{S}X\vec{B} \qquad (4.3)$$

where S is the surface enclosed by the small loop. Due to the similarity between results in (4.3) and the torque applied to a differential electric dipole dp by an electric field $\vec{E}$, which is given by $\vec{T} = \vec{P}X\vec{E}$, differential magnetic dipole moment is defined for a small circulating current shown in Fig. 4.1 as [52]:

$$\vec{m} = I\vec{S} \qquad (4.4)$$

where,

$\vec{m}$ is the magnetic dipole moment, a vector measured in ampere-square meters, or equivalently in joules per tesla.

$\vec{S}$ is the vector area of the current loop.

I is the current in the loop (assumed to be constant), a scalar measured in amperes.

In addition to the current loop as a source of magnetic moment, the electron, among other fundamental particles, has a magnetic dipole moment ($\vec{m}$). This is because it generates a magnetic field which is identical to that generated by a very small current loop, and the magnetic moments of atoms are the building blocks of natural magnetic materials.

$$\vec{m} = I\,\vec{S}$$

I
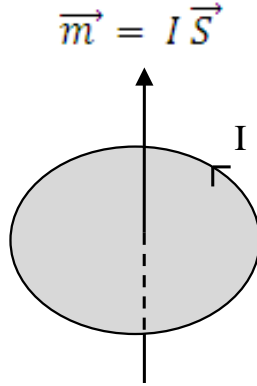
Figure 4.1: Magnetic dipole moment for a small circulating current.

The macroscopic magnetic properties of materials are the consequence of the micro-scopic magnetic moments associated with individual electrons. Due to the much greater nuclear masses, the magnitude of the nuclear magnetic moments produced by the move-ment of protons in the atomic nucleus is much smaller and negligible compared with the magnitude of electron magnetic moments. The motion of each electron in an atom provides two sources of magnetic moments, one originates from the orbital motion of the electron around the nucleus; being a moving charge every electron acts like a small circulating cur-rent producing a very small magnetic field and having a magnetic moment along its axis of revolution as shown in Fig. 4.2. The second source of magnetic moment is related to the spin of electron about its own axis. This spin magnetic moment is directed along the spin axis. Spin magnetic moments may only be in either an "up" direction or in an anti-parallel "down" direction. By these means each electron in an atom may be thought of as being a small magnet having permanent orbital and spin magnetic moments.

The magnetic polarization vector $(\vec{M})$ (Magnetization Vector) of a material is defined as the average of the individual induced magnetic dipole moments of the atoms in response to an externally applied magnetic field H_{ext}. Thus, it is the magnetic dipole moment per unit volume, measured in amperes per meter [57]:

$$\vec{M} = lim_{\Delta v \to 0} \frac{1}{\Delta v} \sum_{i=1}^{n} \vec{m_i} \qquad (4.5)$$

The net magnetic moment for an atom is just the sum of the magnetic moments of

45
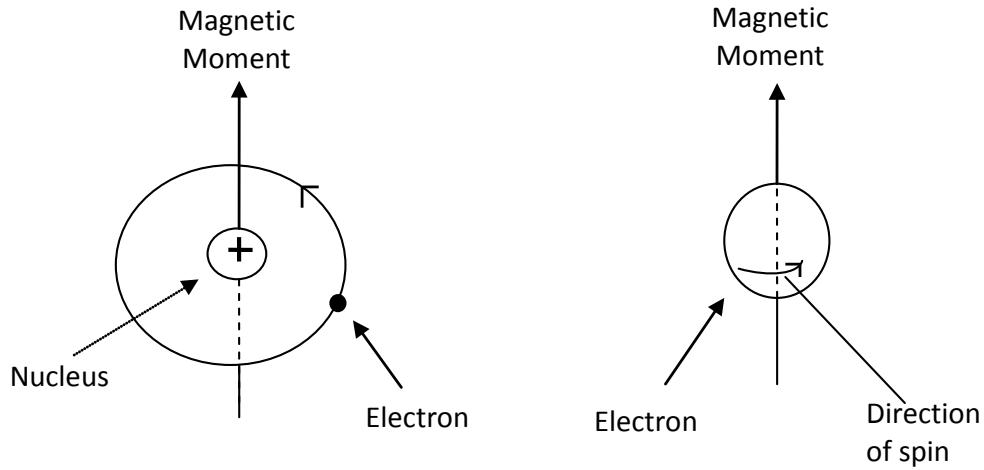
Figure 4.2: Magnetic moment due to (a) the orbital motion of the electron around the nucleus and (b) the electron spin about its own axis.

each electron, including both orbital and spin contributions.

In most of the materials, when no external magnetic field is applied, the net magnetic polarization ($\vec{M}$) is zero due to the total cancelation of the individual magnetic moments of electrons. For example, the spin moment of an electron with spin "Down" will cancel that of one with spin "Up". Also, the orbital magnetic moments of electron pairs cancel each other. For an atom with completely filled electron shells, when all electrons are considered, there is total cancelation of both spin and orbital moments [55].

When an external magnetic field exists, the torque applied to the magnetic dipoles turns the loops such that their magnetic moments align parallel or anti-parallel to the external magnetic field leading to a net value for magnetic polarization vector. The magnetic susceptibility is defined as the degree of magnetization of a material in response to an externally applied magnetic field H_{ext} :

$$\chi_m = \frac{M}{H_{ext}} \tag{4.6}$$

The magnetic field H represents how a magnetic flux density B influences the organization of magnetic dipoles in a given medium, including dipole migration and magnetic dipole reorientation. Its relation to permeability is:

$$\mu = \frac{B}{H_{ext}} = \frac{\mu_0(H_{ext} + M)}{H_{ext}} = \mu_0(1 + \chi_m) \tag{4.7}$$

where the permeability μ is a scalar if the medium is isotropic or a second rank tensor for an anisotropic linear medium. Relative permeability μ_r is the ratio of the permeability of a specific medium to the permeability of free space given by the magnetic constant μ_o:

$$\mu_r = \frac{\mu}{\mu_o} = 1 + \chi_m \tag{4.8}$$

The challenge to microwave applications arises from the inertia of the atomic system. Although the mass of the electron is small, it is not zero and the attempts of the electron magnetic moments to track the external field deteriorate and finally fail as the frequency increases and approaches the microwave region. Thus, for magnetic materials, the upper frequency of operation is limited by the gyromagnetic resonances occurring in the VHF-UHF range. As an example, Fig. 4.3 shows the relative permeability and magnetic loss tangent of Cobalt Hexaferrite, a magnetic material recently developed by Trans-Tech company [58]. As shown in this figure, the maximum useful frequency for this material is below 500 MHz. Since natural magnetization does not occur at microwave frequencies, engineered magnetic materials are designed to provide desirable magnetic properties in these frequencies. The idea of developing artificial magnetic materials is to design a mechanism similar to what happens in natural magnetic materials for microwave operation. In these materials, metallic inclusions are inserted inside the superstrate in which the induced current provides magnetic dipole moments. In the next section, we will introduce this idea and discuss the mechanism of operation of artificial magnetic materials.

4.3   Engineered Magneto-Dielectrics

Due to the difficulties of having low-loss natural magnetic materials at microwave frequencies, development of artificial engineered magnetic materials has recently attracted the attention of many researchers [59]–[61].

An engineered magneto-dielectric material is composed of small metallic resonating particles (inclusions) embedded periodically into a host dielectric to achieve magnetic permeability and electric permittivity larger than that of the host medium. Fig. 4.4 shows an
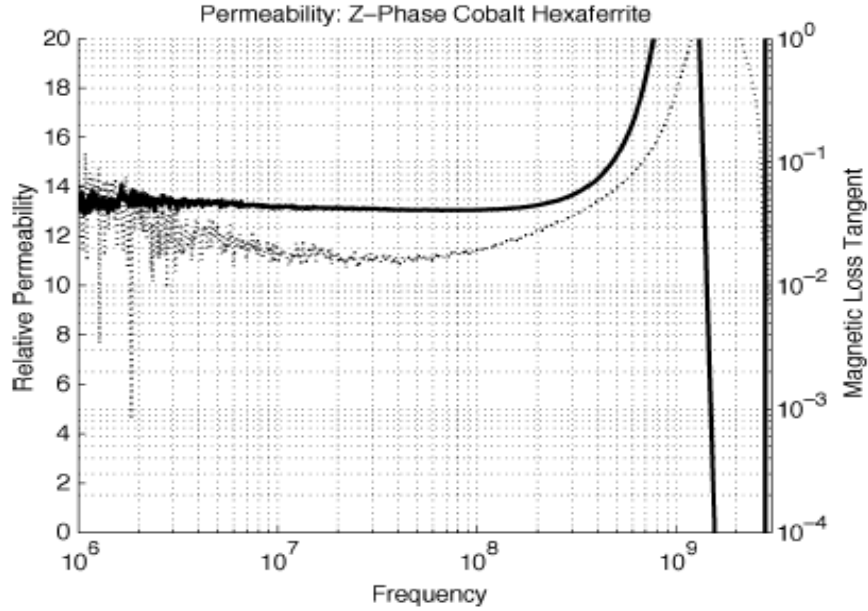
Figure 4.3: Measured magnetic permeability and loss tangent of Cobalt HexaFerrite (solid and dashed lines, respectively).

engineered magnetic superstrate placed over a patch antenna, the superstrate is composed of broadside-coupled split-ring resonator (SRR) particles.

Fig. 4.5 shows different shapes of the embedded circuits used as a unit cell of artificial engineered material [32]–[34]. Regardless of their different structures, the mechanism of operation for all artificial magnetic particles is the same. When an external magnetic field H_{ext} is incident (see Fig. 4.6) normal to the plane of these resonating cells (inclusions), the change in the magnetic flux enclosed by these rings induces an Electromotive Force (emf) in the rings. The emf voltage supplies a current in these metallic elements. This circulating current generates a magnetic moment normal to the inclusion plane and this magnetic moment is the metamaterial equivalent to the atomic magnetic dipole moment of naturally permeable materials.
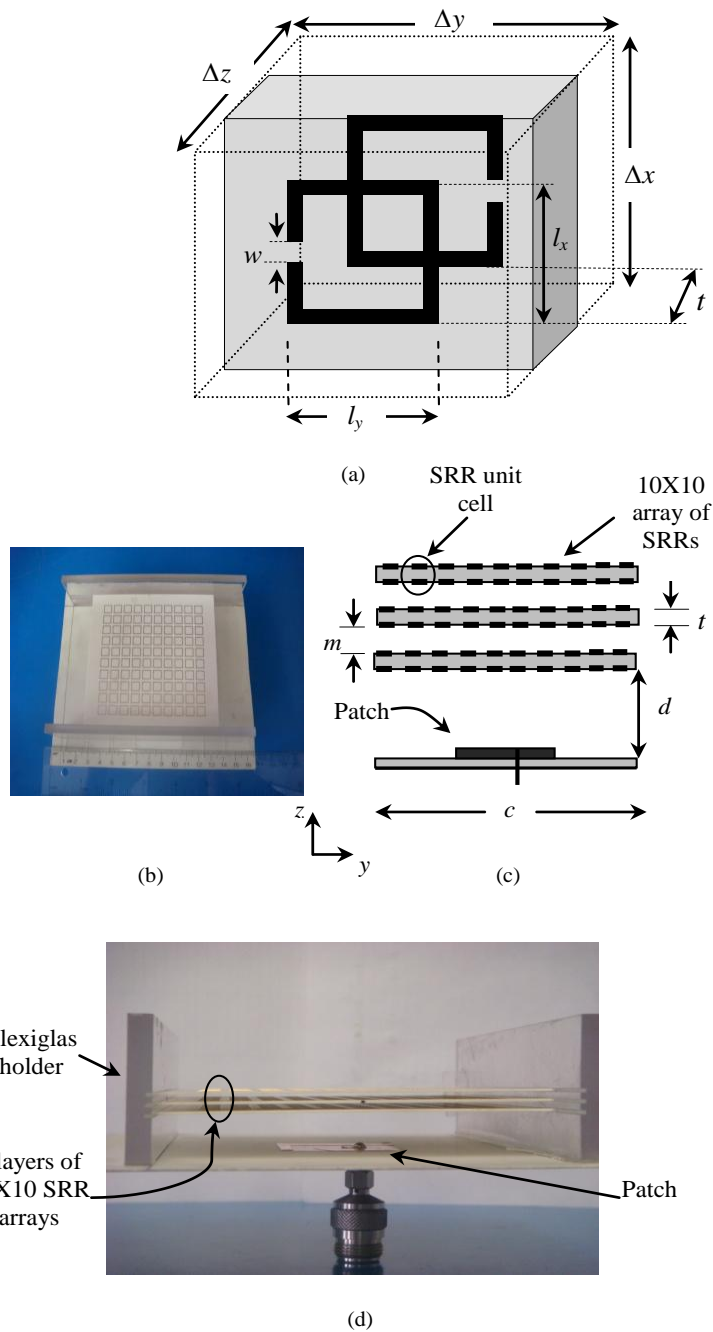
Figure 4.4: Geometry of a patch antenna covered with an engineered magnetic superstrate. (a) SRR unit cell. (b) Photograph of top view. (c) Side view. (d) Experimental prototype ($t = 0.762$ mm, $m = 2$ mm, $c = 85$ mm and $d = 12$ mm).
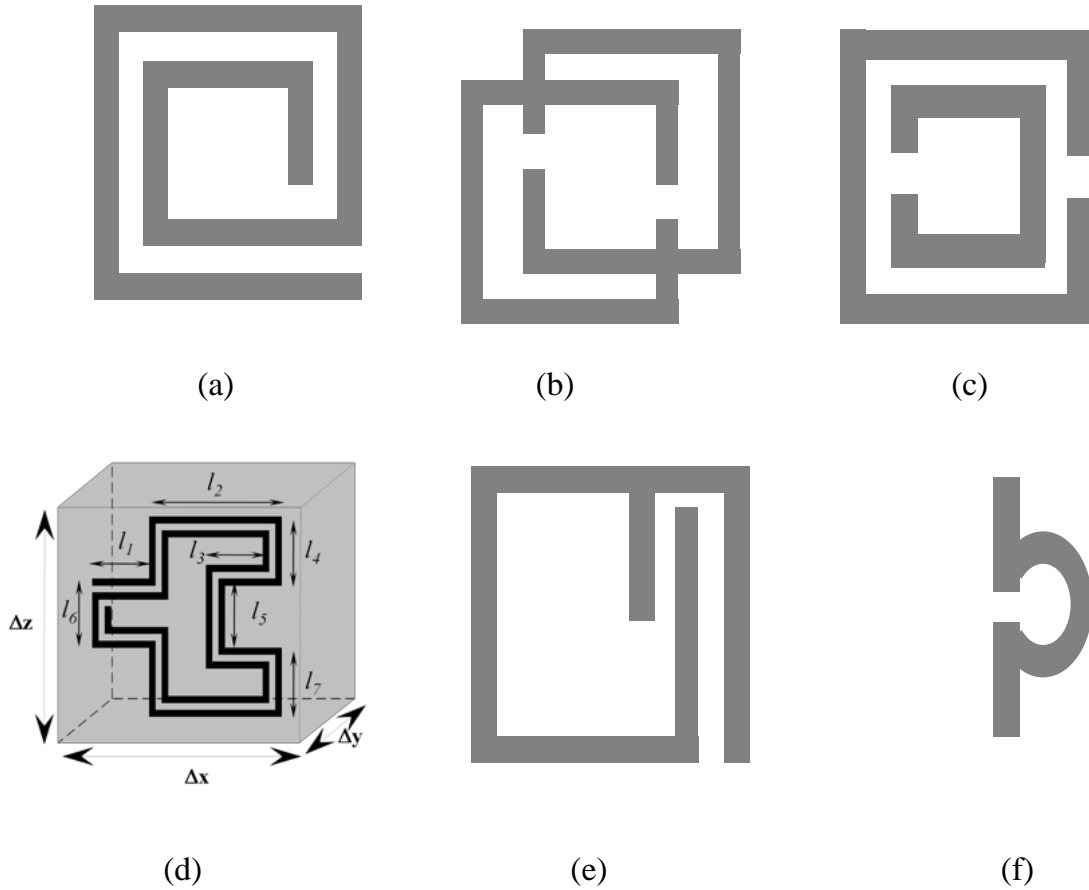
Figure 4.5: Different shapes of the embedded circuits used as a unit cell of artificial engineered material a) Split Spiral b) Broadside-coupled SRR c) Edge-coupled SRR d) Fractal Hilbert Resonator e) Square LC Resonator f) 'Omega' Medium resonator.

4.3.1 Analytical Modeling of the Unit Cell of Metamaterial

As discussed in the previous section, the operational principle of any shape of the artificial magnetic particles (metallic inclusions) shown in Fig. 4.5 is the same.

As a starting point, the analytical model to extract the electromagnetic properties of any shape of the resonating particles will be investigated in details. It is assumed that the particles shown in Fig. 4.5 are excited by an external magnetic field perpendicular to the plane of the particle (see Fig. 4.6); this magnetic field induces an electromotive force

emf^{ext} in the inclusions. Regardless of the shape of these inclusions, near the resonance frequency an effective current is induced in these resonating unit cells due to the external electromotive force emf^{ext}.

Fig. 4.6(a) shows that the unit cell of SRR is composed of two metallic closed loops (rings) with splits in them at opposite locations. The loops can be concentric or circular. The splits in the rings make the structure support resonant wavelengths much larger than the diameter of the rings, this would not happen in closed rings. Also, large capacitance is produced by the small gap between the two rings, this capacitance is important to reduce the the resonating frequency. The dimensions of the SRR (i.e. $\Delta x, \Delta y$ and Δz) are small compared to the resonant wavelength. This results in low radiative losses, and very high quality factors.

The circulating effective current flows across the capacitive gaps introduced in the structures and produces magnetic field which results in an inductive part of the total impedance of an inclusion. The real part of the total impedance represents the loss due to the finite conductivity of metal strips. Hence, the induced effective current for all these structures shown in Fig. 4.5 can be expressed as [32]:

$$I = \frac{emf^{ext}}{Z_{tot}} = \frac{emf^{ext}}{R_{eff} + j\omega L_{eff} + \frac{1}{j\omega C_{eff}}} \qquad (4.9)$$

The effective capacitance in (4.9) is the capacitance formed between every pair of SRR rings due to the symmetry. From (4.9), it is clear that the particles experience a resonant response due to the interaction between the inductance and capacitance of the particle (inclusion). Thus, the unit cell of the metamaterial can be simply modeled as an RLC resonator as shown in Fig. 4.7.

Fig. 4.8 shows the equivalent transmission line model of the host medium with an embedded metallic inclusion, the host medium is represented by the classic RLCG transmission line model and the embedded inclusion is represented by an RLC resonator. At the frequencies lower than the resonant frequency the inductive part of the total impedance Z_{tot} vanishes and the capacitive part dominates.

Using Faraday's law, the external electromotive force emf^{ext} can be expressed as:

$$emf^{ext} = -j\omega\phi = -j\omega BS = -j\omega\mu_0 NSH_{ext} \qquad (4.10)$$
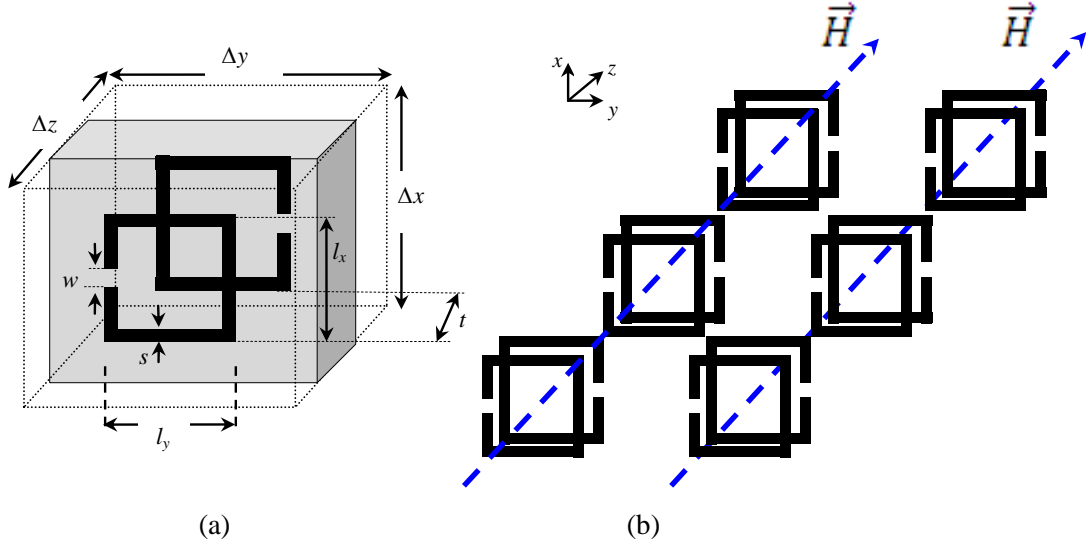
Figure 4.6: An external magnetic field H_{ext} is incident normal to the plane of the SRR acting as resonating cells (inclusions) (a) The unit cell of SRR; (b) Stacked cells in the Z-direction.
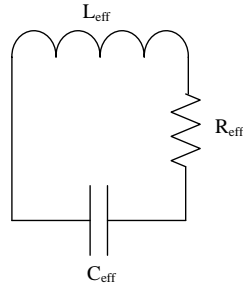
Figure 4.7: Equivalent lumped-element circuit model of the unit cell of metamaterial.

Where S is the surface area of an inclusion penetrated by the external magnetic field H_{ext}, and N is the number of turns [$N = 2$ for the cases (a) and (d), $N = 1$ for the cases (b) and (c) in Fig. 4.5]. The artificial particles shown in Fig. 4.6(b) form a periodic structure with a periodicity of Δz in the Z-direction. One can think of this configuration as a solenoid of stacked particles having any shape of those shown in Fig. 4.5 along the Z-axis. A uniform field distribution can be assumed because of the long-solenoid structure. According to this observation, the inductance of the unit cell having any shape can be expressed as [33]:
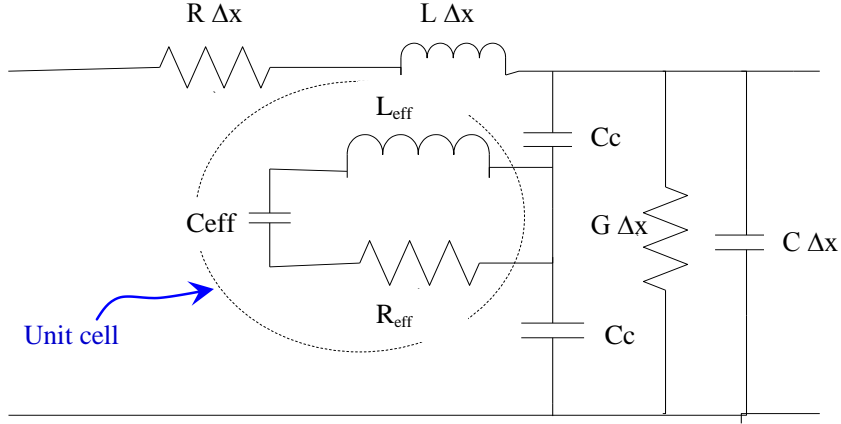
Figure 4.8: Equivalent transmission line model of the engineered metamaterial.

$$L_{eff} = \frac{N^2 S \mu_0}{\Delta z} \tag{4.11}$$

The magnetic polarization $\vec{M}$ of the unit cell which is the average of the induced magnetic dipole moments is obtained as:

$$\vec{M} = lim_{\Delta v \to 0} \frac{1}{\Delta v} \sum_{i=1}^{n} \vec{m_i} \tag{4.12}$$

And the magnetic dipole moment of each turn in the unit cell is:

$$\vec{m} = I\vec{s} = \frac{\omega^2 \mu_0 N S^2 C_{eff} H^{ext}}{1 - \omega^2 L_{eff} C_{eff} + j\omega R_{eff} C_{eff}} \tag{4.13}$$

Substituting (4.13) in (4.12) gives the magnetic polarization $\vec{M}$ as:

$$\vec{M} = \frac{NI\vec{s}}{\Delta x \Delta y \Delta z} = \frac{\omega^2 \mu_0 N^2 S^2 C_{eff} H^{ext}}{\Delta x \Delta y \Delta z (1 - \omega^2 L_{eff} C_{eff} + j\omega R_{eff} C_{eff})} \tag{4.14}$$

where Δx, Δy, and Δz are unit cell dimensions as shown in Figure Fig. 4.6(a).

4.3.2 Analytical Retrieval of the Effective Parameters of the Split-Ring Resonator Inclusions

4.3.3 Effective Permeability

The unit cell of the split-ring resonator SRR inclusion shown in Fig. 4.6(a) is embedded into a host dielectric medium. Assuming that the structure is infinite in the Z-direction and the external magnetic field H_{ext} is applied in the same direction normal to the plane of the inclusion, the external magnetic field induces a current I in the periodic structure which in turn induces another magnetic field H_{ind} in the inclusion. Thus, the total magnetic flux in the unit cell can be expressed as [32]:

$$\phi = BS = \mu_0 NS(H^{ext} + H^{ind}) = \mu_0 NS(H^{ext} + \frac{NI}{\Delta z}) \tag{4.15}$$

where N is the number of wire turns carrying the induced current and $(S=lx{*}ly)$ is the surface area of the inclusion shown in Fig. 4.6(a). The induced magnetic field H_{ind} can be expressed as $NI/\Delta z$ where Δz is the unit cell dimension in the Z-direction.

The voltage drop on the effective loss resistance and the capacitive gap of the unit cell must be equal to the electromotive force produced by the total flux:

$$-j\omega\phi = I(R_{eff} + \frac{1}{j\omega C_{eff}}) \tag{4.16}$$

Substituting (4.15) into (4.16) gives:

$$I = \frac{emf^{ext}}{Z_{tot}} = \frac{-j\omega\mu_o NSH^{ext}}{R_{eff} + j\omega\mu_o \frac{N^2}{\Delta z}S + \frac{1}{j\omega C_{eff}}} \tag{4.17}$$

From (4.17), it is clear that the inductive part of the total impedance of an inclusion L_{eff} is equal to ($\mu_o \frac{N^2}{\Delta z}S$) which is due to the induced magnetic field produced by the circulating effective current I in the structures.

The formula of L_{eff} of the inclusion concluded from (4.17) is consistent with our physical interpretation given in the previous section and equation (4.11). Also, the formula of L_{eff} can be used for any of the shapes of the inclusions given in Fig. 4.5.

The real part R_{eff} of the total impedance of an inclusion represents the loss due to the finite conductivity of metal strips and can be obtained as [57]:

$$R_{eff} = \frac{N'l^{tot}}{s\sigma\delta_s} \tag{4.18}$$

where:

N' is the number of wire turns which contribute to ohmic losses [N'=2 for case (a), (b) and (c) in Fig. 4.5].

l^{tot} is the total length of the metallic strips and equals to $2(lx+lz)$.

σ is the conductivity of the metallic strip.

δ_s is the skin depth.

s is the strip width (trace metallization).

and the skin depth of the metal is defined as [53]:

$$\delta_s = \sqrt{\frac{2}{\sigma\omega\mu}} \tag{4.19}$$

The effective capacitance in (4.17) is the total capacitance of two capacitive gaps connected in series in the SRR unit cell. The effective capacitance can be computed by the following approach [32]. In an infinite array of SRRs, equipotential surfaces are formed between every pair of rings due to the symmetry. Therefore, the effective capacitance of the SRR can be expressed as the capacitance per unit length of a symmetric strip line multiplied by the total overlapping length of two neighboring rings and is given by [32]:

$$C_{eff} = C_o * l^{tot} \tag{4.20}$$

where C_o is the capacitance per unit length of a symmetric strip line:

$$C_o = \frac{1}{4}\varepsilon_{diel}\frac{K(g)}{K(\sqrt{1-g^2})}, \qquad g = \tanh(\frac{\pi s}{2t}) \tag{4.21}$$

where ϵ_{diel} is the permittivity of the host medium in which the unit cells are embedded, s and t are the width of the metallic strips and the spacing between the two rings, respectively (see Fig.4.6(a)). The elliptical integral $K(g)$ can be obtained as:

$$K(g) = \int\limits_{0}^{\pi/2} \frac{d\theta}{\sqrt{1 - g^2 \sin^2 \theta}} \tag{4.22}$$

Substituting (4.11), (4.18) and (4.20) into (4.17), the magnetic polarization vector $\vec{M}$ can be obtained as:

$$\vec{M} = \frac{NI\vec{S}}{\Delta x \Delta y \Delta z} = \frac{-j\omega\mu_o N^2 S^2 H^{ext}}{\Delta x \Delta y \Delta z (R_{eff} + j\omega\mu_o \frac{N^2}{\Delta z} S + \frac{1}{j\omega C_{eff}})} \tag{4.23}$$

Using (4.23), the effective relative permeability of the SRR unit cell can be obtained as:

$$\mu_{r_{eff}} = 1 + \chi_m = 1 + \frac{M}{H_{ext}} \tag{4.24}$$

It is clear from the previous equation that the resultant effective enhanced permeability is provided only in the direction of the external magnetic field which is perpendicular to the plane of the SRR unit cell (Z- direction in our case as shown in Fig. 4.6. Any incident magnetic field in X or Y direction will not couple to the SRR inclusion resulting in a permeability equal to that of free-space. Hence, the artificial engineered material composed of the SRR inclusions will experience anisotropic magnetic permeability having this tensor form:

$$\bar{\bar{\mu}} = \mu_o \begin{bmatrix} 1 & 0 & 0 \\ 0 & 1 & 0 \\ 0 & 0 & \mu_{r_{eff}} \end{bmatrix} \tag{4.25}$$

4.3.4 Effective Permittivity

Consider an X-directed electric field incident on the SRR unit cell shown in Fig. 4.6. Inter-cell capacitors are formed in the gap regions between the metallic inclusions (unit cells) due to the incident X-directed electric field. Therefore, an effective X-directed permittivity of (4.26) is provided by the stored electrical energy in these inter-cell capacitors. The same phenomenon is observed for an Y-directed incident electric field. But, in case of Z-directed

electric field, the metamaterial will experience an effective permittivity equal to that of its host dielectric as the electric field is perpendicular to the plane of the unit cell in this case. Hence, the artificial engineered material composed of the SRR inclusions will experience anisotropic electric permittivity of (4.28) [33]:

$$\varepsilon_{r_{eff}} \;\; = \;\; \varepsilon_{r_{diel}} \left[1 + \frac{\Delta z l_x}{\Delta x \Delta y} \frac{K(\sqrt{1-g^2})}{K(g)} \right], \qquad g = \tanh(\frac{\pi s}{2t}) \qquad (4.26)$$

$$K(g) \;\; = \;\; \int_{0}^{\pi/2} \frac{d\theta}{\sqrt{1-g^2 \sin(\theta)}} \qquad (4.27)$$

$$\overline{\overline{\varepsilon}} \;\; = \;\; \varepsilon_o \begin{bmatrix} \varepsilon_{r_{eff}} & 0 & 0 \\ 0 & \varepsilon_{r_{eff}} & 0 \\ 0 & 0 & \varepsilon_{r_{diel}} \end{bmatrix} \qquad (4.28)$$

Unlike the effective permeability, the effective permittivity is not frequency dependent as indicated by (4.26). The effective permittivity is a function of the inter-cell capacitance, which is calculated by means of the same elliptical integral that was used to find the SRR capacitance (4.21)).

As this analytical study has indicated, this artificial engineered material will experience strong anisotropic behavior. Permeability improvement will be achieved for Z-directed magnetic fields only. Permittivity improvement will occur only for X- or Y-directed electric fields. This combination of orientation-dependent permeability and permittivity should match the orientations needed to support the modes of a microstrip patch antenna when covered by the metamaterial superstrate.

Using (4.18)-(4.28), the effective relative permeability and permittivity of the SRR unit cell of Fig. 4.6 are calculated and illustrated in Fig. 4.9. The design parameters of the SRR used in this calculation are: $\Delta x = \Delta y = 8.5$ mm, $\Delta z = 2.762$ mm, $lx = ly = 6.5$ mm, $s = w = 0.3$ mm, host dielectric has $\epsilon_r = 3.48$, and strips are assumed to be made of copper. The SRR unit cell of Fig. 4.6 can be simply modeled as an RLC resonator as shown in Fig. 4.7. Therefore, its resonance frequency can be estimated from:

$$F_{res} = \frac{1}{2\pi \sqrt{L_{eff} C_{eff}}} \qquad (4.29)$$

57
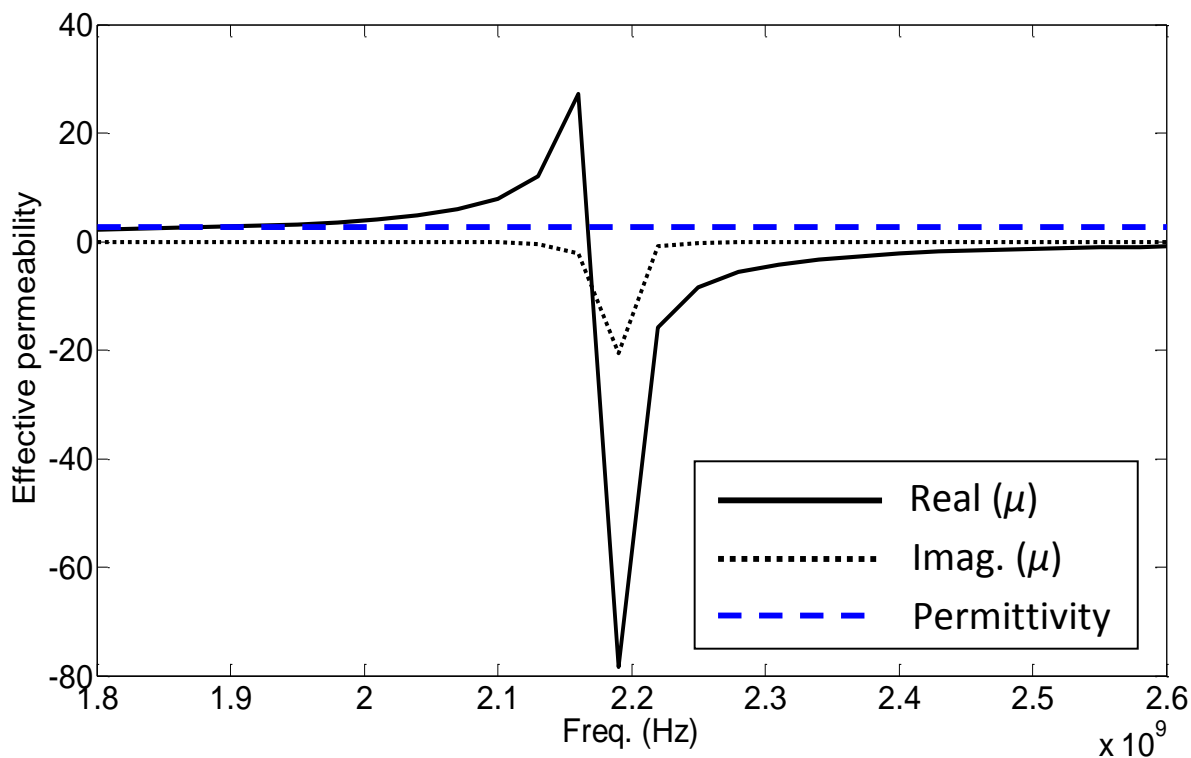
Figure 4.9: Analytically calculated relative permeability and permittivity of the SRR inclusion shown in Fig. 4.6.

From (4.11) and (4.20), the effective inductance and capacitance of the SRR inclusion are found to be 88.059 nH and 0.060369 pF, respectively. Hence, from (4.29) the resonance frequency is 2.18 GHz which is very close to that indicated by Fig. 4.9 where the real part of permeability reaches its maximum absolute value.

Fig. 4.10 shows the possible values of the permeability and permittivity of metamaterials and their corresponding applications.

For the purpose of assessing the accuracy of this characterization technique, the retrieved parameters shown in Fig. 4.9 will be validated numerically in the next section
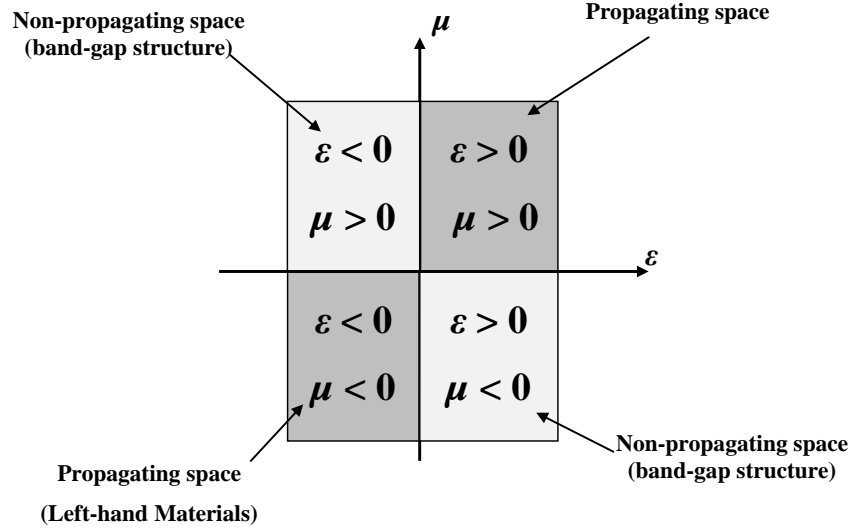
Figure 4.10: Possible values of the permeability and permittivity of metamaterials and their corresponding applications.

4.4 Numerical Retrieval of the Effective Parameters of Metamaterials

In this section, the effective constitutive parameters $\mu_{r_{eff}}$, $\epsilon_{r_{eff}}$ of artificial engineered materials are extracted using numerical full-wave analysis. The commercial EM solver HFSS based on the finite-element method is used to perform this analysis. The retrieval of the effective permittivity and permeability of a slab of metamaterial is based on characterizing it as an effective homogeneous slab. In this case, the reflection and transmission coefficients (S-parameters) calculated for a wave incident normally on a unit cell of metamaterial are used to calculate the effective index of refraction $n_{eff} = \sqrt{\mu_{r_{eff}} \epsilon_{r_{eff}}}$ and the relative characteristic impedance $\eta_{eff} = \sqrt{\mu_{r_{eff}}/\epsilon_{r_{eff}}}$ of the metamaterial unit cell [56, 59].

The simulation of an infinite periodic structure is less computationally expensive than the simulation of a finite metamaterial structure. So, it is numerically more efficient to work with the unit cell of the metamaterial to characterize its effective constitutive parameters $\mu_{r_{eff}}$, $\epsilon_{r_{eff}}$ by using the periodic boundary condition (PBC) as shown in Fig. 4.11.

One way to characterize metamaterials is to examine their reflection and transmission responses as functions of the frequency. To derive these reflection and transmission char-
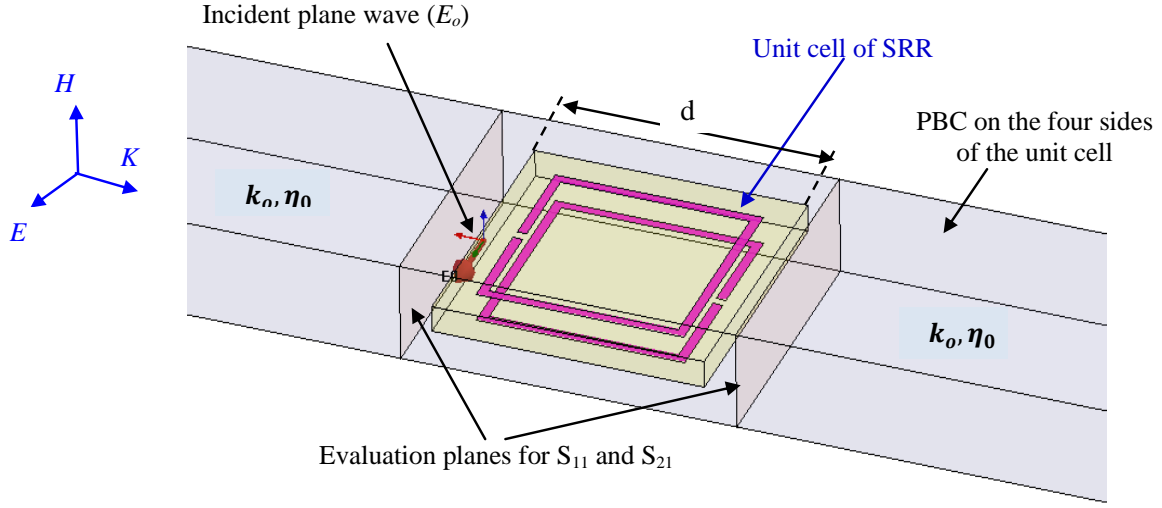
Figure 4.11: Simulation geometry for numerical retrieval of the effective parameters of metamaterials using plane wave incidence on the metamaterial unit cell.

acteristics (S_{11} and S_{21}), the metamaterial unit cell is illuminated with a plane wave from the left side as shown in Fig. 4.11. Then, the reflection and transmission coefficients are computed by the HFSS EM solver with the PBC applied to the four sides of the unit cell, and the radiation type of absorbing boundaries for the right and left sides of the unit cell [56]-[57]. Using the classic transmission line analogy, the S-parameters are related to refractive index n_{eff} and impedance η_{eff} by [59]:

$$S_{11} = \frac{R_{o1}(1 - e^{j2n_{eff}k_o d})}{1 - R_{01}^2 e^{j2n_{eff}k_o d}} \tag{4.30}$$

$$S_{21} = \frac{(1 - R_{01}^2)e^{jn_{eff}k_o d}}{1 - R_{01}^2 e^{j2n_{eff}k_o d}} \tag{4.31}$$

where,

$$R_{o1} = \frac{\eta_{eff} - 1}{\eta_{eff} + 1}$$

η_{eff} is the effective characteristic impedance of the metamaterial unit cell (relative to the characteristic impedance of free-space).

d is thickness of the metamaterial unit cell.

60

From the previous two equations, the effective constitutive parameters of the metamaterial unit cell can be obtained as:

$$\eta_{eff} = \pm\sqrt{\frac{(1 + S_{11})^2 - S_{21}^2}{(1 - S_{11})^2 - S_{21}^2}} \tag{4.32}$$

$$e^{jn_{eff}k_o d} = X \pm j\sqrt{1 - X^2}, \quad X = \frac{1 - S_{11}^2 + S_{21}^2}{2S_{21}} \tag{4.33}$$

$$\mu_{r_{eff}} = \eta_{eff}\, n_{eff}, \qquad \varepsilon_{r_{eff}} = \frac{n_{eff}}{\eta_{eff}} \tag{4.34}$$

Since the metamaterial under consideration is a passive medium, the signs in (4.32) and (4.33) are determined by the requirement [59]:

$$Re(\eta_{eff}) \geq 0, \quad Im(n_{eff}) \geq 0$$

For the purpose of assessing the accuracy of this characterization technique, the retrieval technique has been validated based on simulated scattering data obtained from a slab of a homogeneous isotropic material with known properties. Rogers R04003 dielectric material with relative permittivity of 3.38, relative permeability of 1 and thickness d of 10 mm has been used as a sample for this purpose. The retrieved constitutive parameters of this material are shown in Fig. 4.12 and Fig. 4.13. Both of the extracted results are in good agreement with the known values, indicating that the retrieval method works very well.

For the purpose of assessing the accuracy of the analytical characterization technique presented in the previous section, the retrieved parameters shown in Fig. 4.9 of the SRR will be validated numerically using the simulation setup shown in Fig. 4.11. The split-ring resonator SRR unit cell being numerically characterized has the same dimensions and the same host dielectric used in the previous section. Fig. 4.14 shows a comparison between the numerically and analytically calculated relative permeability and permittivity of the SRR inclusion shown in Fig. 4.6. The discrepancy between both methods (see Fig. 4.14) is due to the fact that the accuracy of the analytical method is not high as it is based on several approximations in finding the lumped circuit equivalent elements of the unit cell as discussed in the previous section. It is worth mentioning that the analytical method of characterization is very fast in extracting the effective parameters compared with the numerical technique based on transmission line modeling of the metamaterial unit cell.
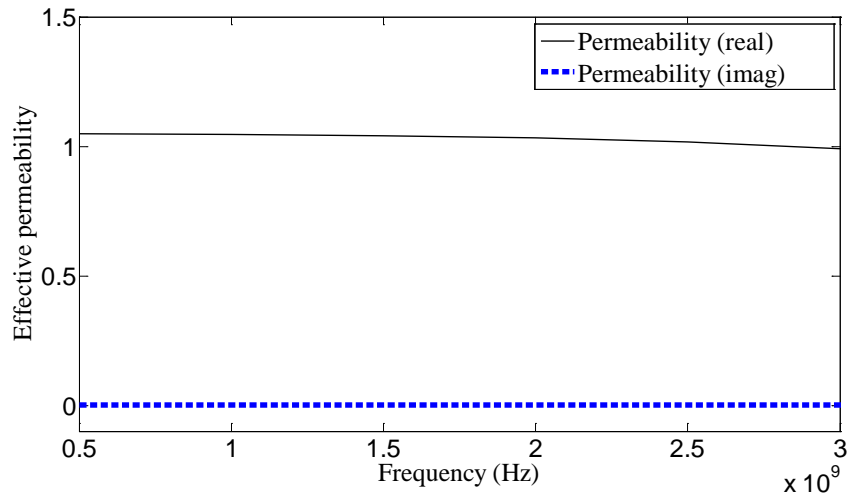
Figure 4.12: Numerically retrieved permeability of Rogers R04003 dielectric material.
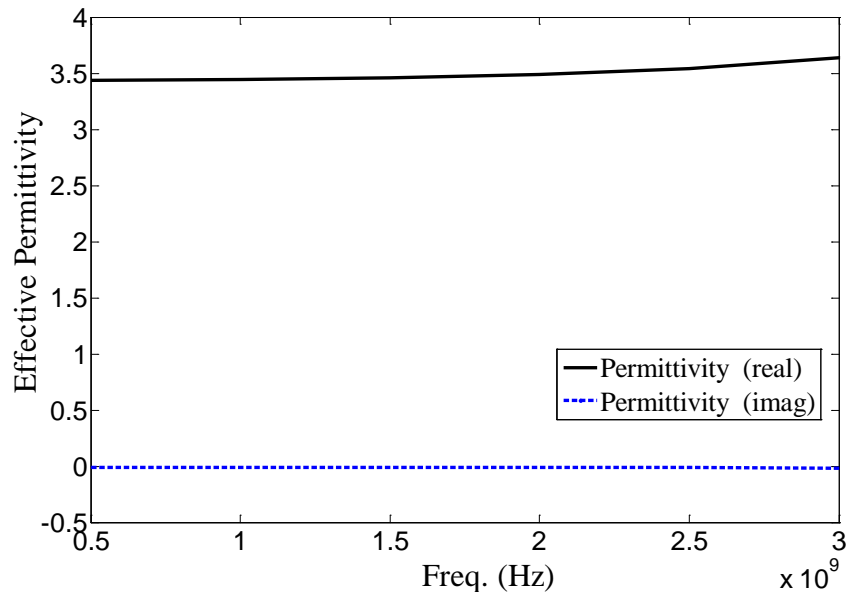
Figure 4.13: Numerically retrieved permittivity of Rogers R04003 dielectric material.

The SRR-based metamaterial presented here is designed to work at 2.2 GHz which makes it useful as a superstrate for planar antennas working in the UMTS (Universal Mobile Telecommunications System) band.

As shown in Fig. 4.14 and according to the numerically extracted permeability, the
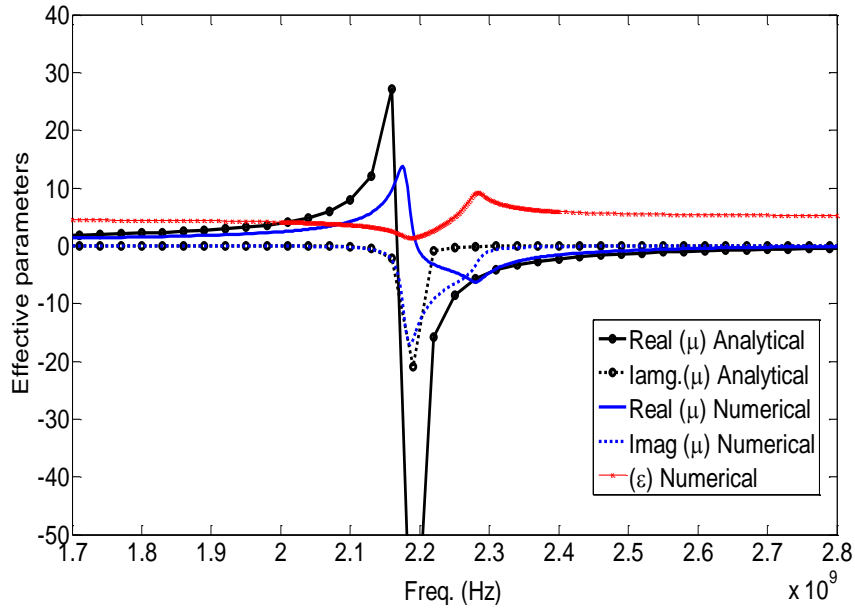
Figure 4.14: Comparison between the numerically and analytically calculated relative permeability and permittivity of the SRR inclusion shown in Fig. 4.6.

value of the real part of the permeability is greater than one in the range 1.7 - 2.19 GHz and the imaginary part of it is close to zero (means low losses) in this range. As resonance is approached both the magnetic permeability and the magnetic loss mechanism μ_{imag} increases significantly, and in the region immediate above resonance the magnetic permeability is negative. As shown in Fig. 4.14, the maximum value of the permeability (real) is 16 at 2.18 GHz and the permittivity is 2.0 at same frequency. Also, the permeability (imaginary) is -11.2 at the same frequency of 2.18 GHz.

Based on the resonance conditions derived in chapter (3) which require a superstrate with very high magnetic permeability and nominal electric permittivity in order to increase the antenna gain, the SRR-based metamaterial presented in this chapter is useful as a superstrate for planar antennas working in the UMTS band.

4.5 Concluding Remarks

In this chapter, the operational principle of the artificial engineered materials has been investigated as an emulation of the magnetization occurred in natural magnetic materials. The analytical model of the split-ring resonator SRR unit cell acting as a building block of the metamaterial has been presented and the analytically calculated effective permeability and permittivity have been found to be in a good agreement with the numerically calculated parameters using a plane wave incident on the metamaterial SRR unit cell. The SRR-based metamaterial is designed to work at 2.2 GHz which makes it useful as a superstrate for planar antennas working in the UMTS band.

It is worth mentioning that the analytical method of characterization is very fast in extracting the effective parameters compared with the numerical technique based on transmission line modeling of the metamaterial. However, the accuracy of the analytical method is not as high as the numerical technique, this is because the analytical method is based on several approximations in finding the equivalent lumped circuit elements of the unit cell.

Chapter 5

Enhanced-Gain Planar Antennas Using Artificial Magnetic Superstrates

5.1   Introduction

Based on the resonance conditions derived in Chapter 3 which require a high permeability superstrate to increase the antenna gain, this chapter presents a novel engineered magnetic superstrate designed to enhance the gain of planar antennas without any substantial increase in the profile of the whole structure (the antenna with the superstrate). The broadside-coupled split ring resonator inclusions (which was studied in previous chapter) are used herein in the design of the engineered magnetic superstrate. Numerical full-wave simulations as well as experiments are used to analyze the entire radiating system. Also, the fast analytical formulation for the far field explained in Chapter (2), will be used to calculate the radiation field of the antenna with and without superstrate.

Considering as an example a microstrip patch antenna (MPA) operating within the Universal Mobile Telecommunications System (UMTS) band, the broadside gain of the antenna is improved by 3.8 dBi and the efficiency is improved by 14% when using the engineered superstrate. The total height of the proposed structure, antenna with superstrate, is $\lambda_o/7$ where λ_o is the free-space wavelength at the resonance frequency of the antenna.

Furthermore, the application of the same artificial superstrate for microstrip antenna array and planar inverted-F antenna (PIFA) will be investigated in details. The proposed antenna with superstrate can be used in cellular base stations working in the UMTS.

5.2 Single Patch Antenna with Artificial Magnetic Superstrates

Fig. 5.1(a) illustrates a broadside-coupled split ring resonator (SRR) unit cell acting as a building block of the artificial magnetic superstrate. The SRR inclusion consists of two parallel broken square loops. The host dielectric is made of Rogers RO4350 with a thickness of 0.762 mm, relative permittivity of $\epsilon_r = 3.48$, and loss tangent of $tan\delta = 0.004$. A planar 10 X 10 array of SRRs is printed on the host dielectric layer to provide an engineered magnetic material when illuminated by a magnetic field perpendicular to the plane of the SRR (in Z-direction). The superstrate used herein consists of 3 layers of printed magnetic inclusions. The layers are separated by 2 mm of air layers (see Fig. 5.1(c)). The reason of having these air layers is to reduce the effective permittivity of the superstrate as required by the resonance conditions deduced in Chapter (3).

The SRR unit cell used herein was analytically characterized and the extracted effective parameters (permeability and permittivity) were numerically verified in the previous chapter (see Fig. 4.14). The SRR was designed to work at 2.2 GHz as shown in Fig. (4.14). The dimensions of the SRR unit cell are:

$\Delta x = \Delta y = 8.5$ mm, $\Delta z = 2.762$ mm, $l_x = l_y = 6.5$ mm, $w = 0.3$ mm. The width of metallic strips (s) is equal to 0.3 mm, and the metallic strips are assumed to be made of copper. Since the SRRs inclusions are aligned in the x-y plane, the resultant effective enhanced permeability is provided only in the z direction as clarified in the previous chapter. Any incident magnetic field in the x or y direction will not couple to the SRRs inclusions resulting in a permeability equal to that of free-space in those directions.

The patch antenna used herein (see Fig. 5.1(c))has dimensions of 36 mm x 36 mm, and is printed on a substrate of Rogers RO4350 having a relative permittivity of 3.48, loss tangent of 0.004 and a thickness of 0.762 mm. This antenna is designed to operate within the frequency band of 2190-2210 MHz (downlink band of UMTS) at which the
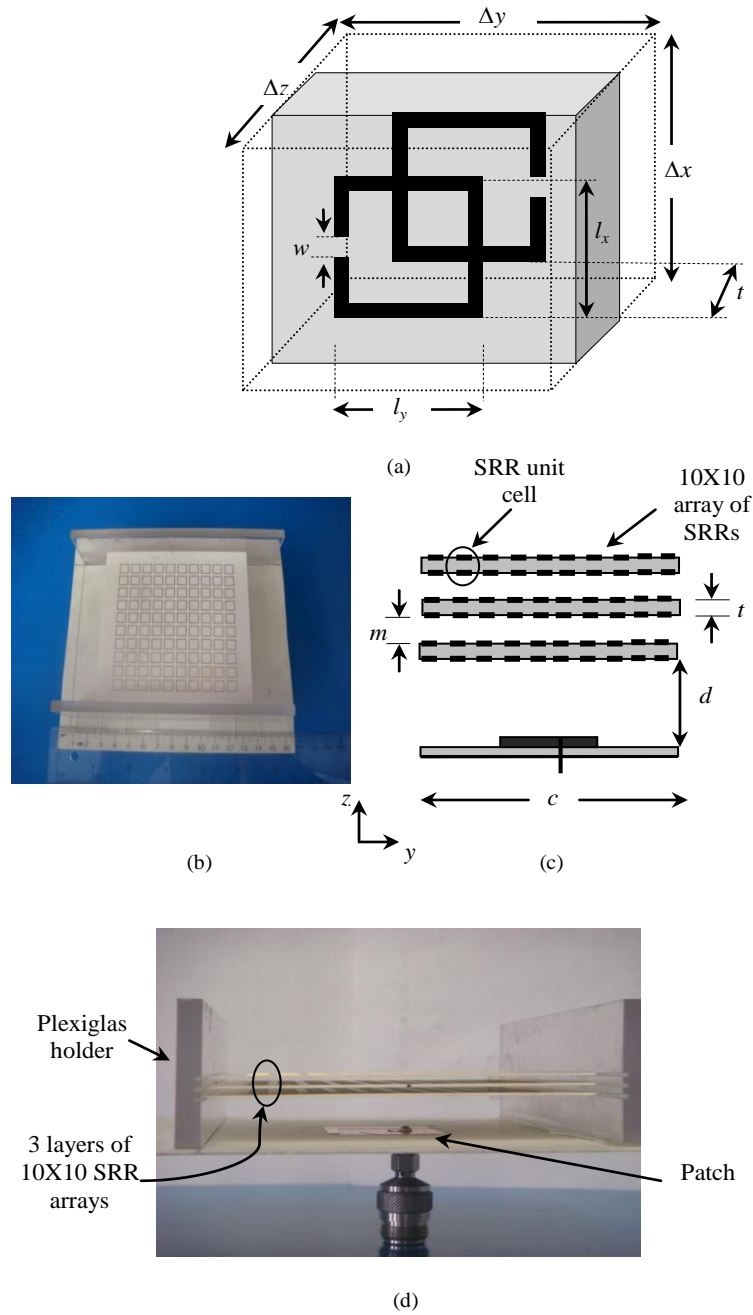
Figure 5.1: Geometry of a patch antenna covered with an engineered magnetic superstrate. (a) SRR unit cell. (b) Photograph of top view. (c) Side view. (d) Experimental prototype ($t = 0.762$ mm, $m = 2$ mm, $c = 85$ mm and $d = 12$ mm).

magnetic superstrate has an effective permeability of about 16 (real part) and an effective permittivity of 2.0 (see Fig. 4.14).

The distance between the patch antenna and superstrate was chosen such that a strong magnetic field exists to excite the SRRs achieving the required high permeability of the artificial superstrate and hence a high gain of the antenna. This distance was determined by parametric analysis using CST to be 12 mm. Fig. 5.2 shows that the magnetic field vectors plotted on a surface at the superstrate location are pointed in Z-direction. This means that the SRRs should be aligned in the XY plane as the resultant effective enhanced permeability is provided only in the direction of the external magnetic field. Note that the resonant spacing between the antenna and the superstrate (i.e. quarter wavelength) is not used herein to avoid enlarging the structure significantly and also due to the lack of strong magnetic field at this distance from the patch antenna.

The proposed analytical solution explained in Chapter 2 is used herein to calculate the radiation field of the MPA loaded with an artificial magnetic superstrate. Substituting the
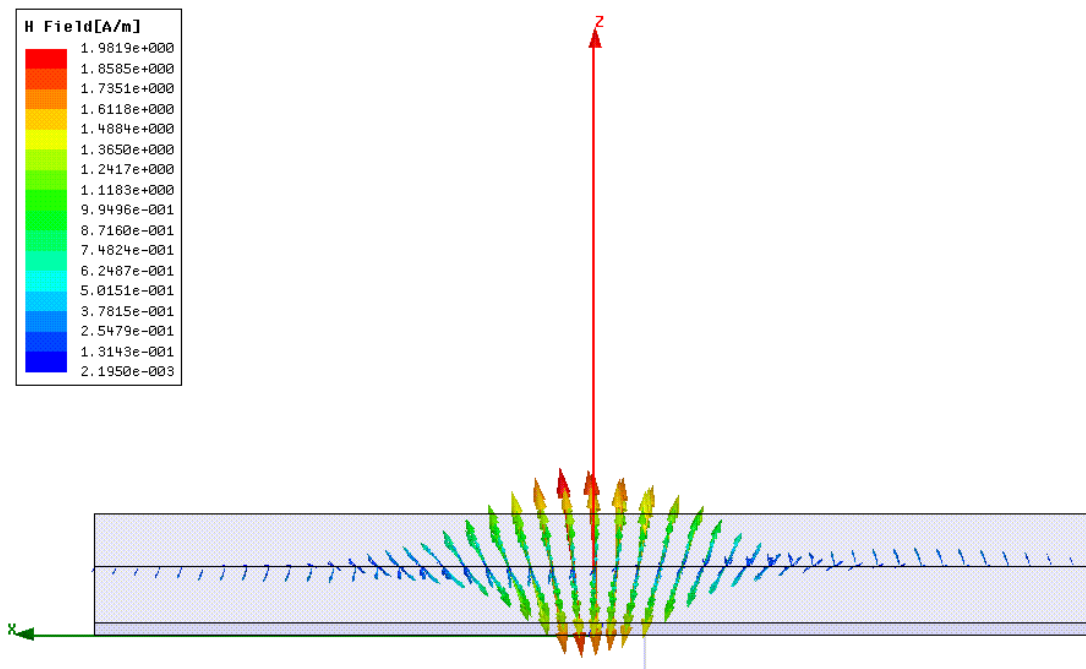
Figure 5.2: A snapshot of the magnetic field vectors plotted on a surface at the superstrate location when the superstrate is removed.

value of permeability and permittivity from (4.34) in the equations presented in Chapter 2, the electric field of the MPA is calculated at the desired frequency using (2.19) and (2.21) and then integrated to calculate the antenna directivity using (2.22). It is worth mentioning that the proposed analytical solution requires only 2.0% of the time required by the commercial software CST.

Fig. 5.3 shows a comparison between the analytical (Eq. 2.22), numerical (CST) and experimental results of the E-plane directivity radiation pattern at the antenna resonance frequency of 2.2 GHz. A good agreement is observed between the three methods despite the vast difference in the computational resources utilized by both methods (analytical method and CST). The H-plane directivity radiation pattern of the same structure is shown in Fig. 5.4, where the discrepancy in the measured results is believed to be due to the finite size of the superstrate used herein. The analysis of the MPA covered with engineered superstrate are performed using Intel(R) Core(TM)2 Quad CPU @2.83GHz machine, the proposed analytical technique (Eq. 2.22) requires 6 minutes and 280 megabytes of RAM using MATLAB, while the CST simulations for the same structure requires about 6 hours and 2 gigabytes of RAM when 45 cells/wavelength with total of 2.6 M mesh-cells were used for the entire structure. However, the analytical technique as presented in this work is not capable of determining the input impedance.

Figs. 5.5 and 5.6 show the reflection coefficient in dB of the MPA with and without the artificial magnetic superstrate, respectively. Good agreement is observed between the CST and the measured results. We note that the feed location had to be slightly adjusted to achieve good matching after using the superstrate due to the loading effect of the superstrate. The overall height of the structure is only $\lambda_o/7$ where λ_o is the free-space wavelength at the resonance frequency.

The reason for using CST to calculate the results in Figs 5.5 and 5.6 is that the time domain simulation module in CST stimulates the structure using a broadband signal. Broadband stimulations calculate the S-parameters for the entire desired frequency range and the radiation patterns at various desired frequencies from only one calculation run. On the other hand, frequency domain solvers such as HFSS perform a new simulation run for each frequency sample. Hence, the relationship between calculation time and frequency steps is linear unless special methods are applied to accelerate subsequent frequency domain solver runs. Therefore, the time-domain solver is usually the fastest when a large number of frequency samples need to be calculated.
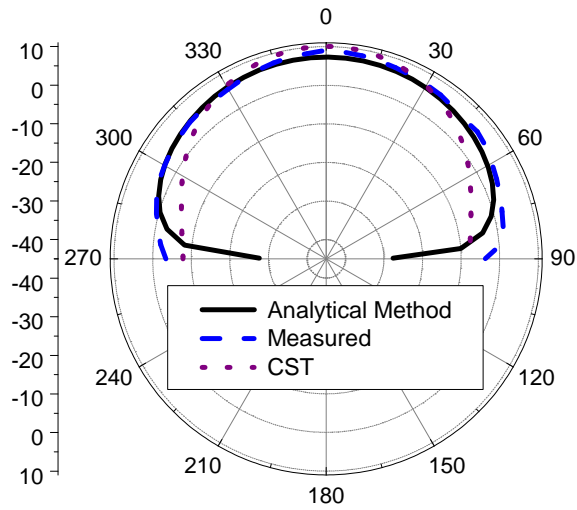
Figure 5.3: The E-plane directivity radiation pattern at 2.2 GHz of the patch antenna covered with the engineered magnetic superstrate.
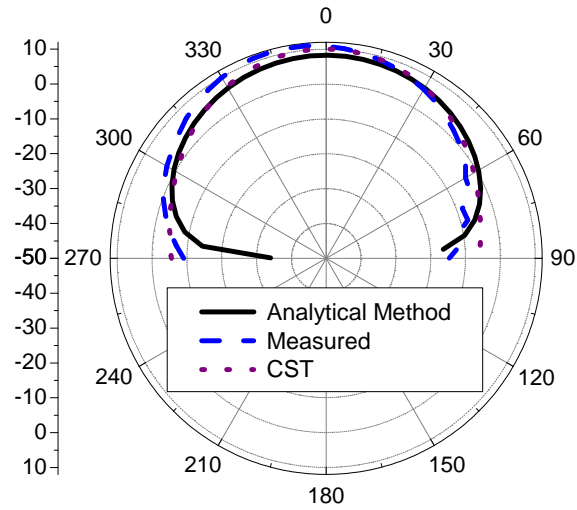
Figure 5.4: The H-plane directivity radiation pattern at 2.2 GHz of the patch antenna covered with the engineered magnetic superstrate.
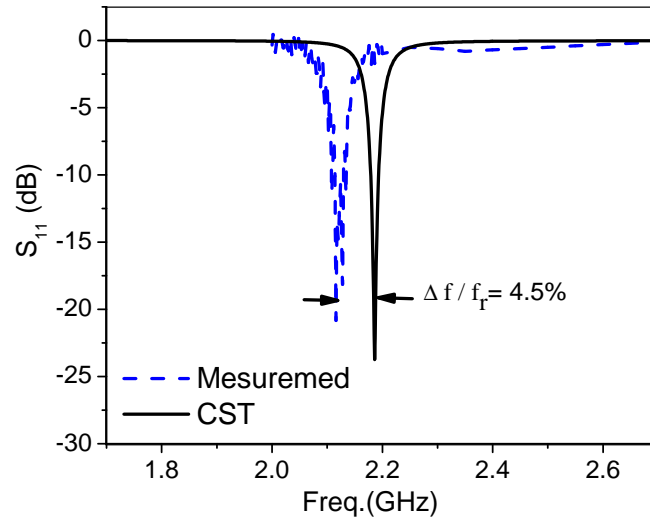
Figure 5.5: The return loss of the microstrip antenna before using the artificial magnetic superstrate.
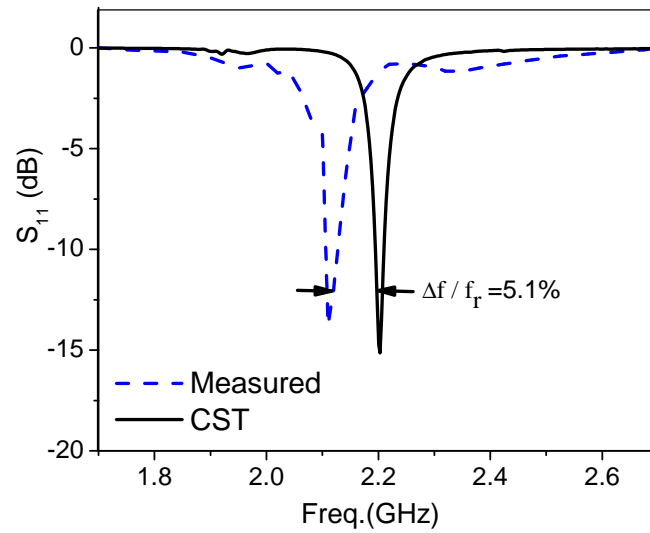
Figure 5.6: The return loss of the microstrip antenna covered with the artificial magnetic superstrate.

Fig. 5.7 shows the gain of the microstrip antenna before and after using the artificial magnetic superstrate. Two different approaches were adopted to calculate the gain of the antenna with superstrate, the first approach was to simulate the antenna with the SRR based superstrate (realistic structure) using HFSS and CST. The second approach was to simulate the antenna with an effective superstrate with the same stack up and dimensions of Fig. 5.1(c) using a dielectric material with relative permeability of 16 and relative permittivity of 2.0 which are the same effective values for the SRR unit cell, this approach shows the effect of the high permeability on the gain of the antenna. Good agreement is shown between the two approaches as shown in Fig. 5.7. The gain is improved by 3.8 dBi at the resonance frequency after using the engineered superstrate. The 3-dB beamwidth for the patch antenna only is 80° compared with 57° for the patch antenna covered with the artificial superstrate. The reduction in the 3-dB beamwidth is an indication of the improved directivity in the broadside direction and the sharpening of the radiation pattern's main lobe.

Fig. 5.8 shows the radiation efficiency of the microstrip antenna before and after using the artificial magnetic superstrate. Both CST and HFSS were used to calculate the radiation efficiency. It is clear that the radiation efficiency was improved over the relevant range of frequencies. Notice that the radiation efficiency is increased by 14% at the resonant frequency once the superstrate is used. The enhanced efficiency is believed to be a consequence of the increase in the antenna gain due to the direct proportionality between the gain and efficiency. The SRR unit cells were simulated as copper in the CST and HFSS simulations in order to mimic the realistic structure and to include the conductor losses due to the artificial superstrate.

The effect of the superstrate's panel size on the antenna performance is presented in Table 5.1. As the panel size increases, the gain increases (notice that as the panel size increases, the effective aperture of the antenna increases, hence the increase in the gain and efficiency). To avoid enlarging the antenna size, we have chosen a panel size of 10X10 array to consider herein as it is approximately 2.3 times the patch size.
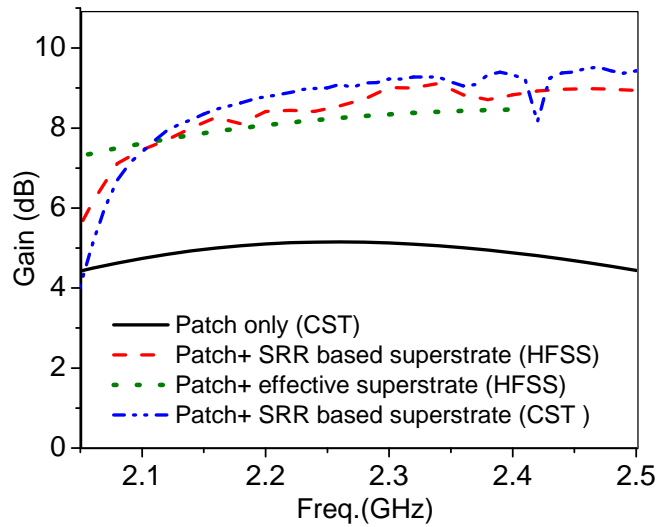
Figure 5.7: The gain of the microstrip antenna before and after using the artificial magnetic superstrate at $d = 12$ mm.
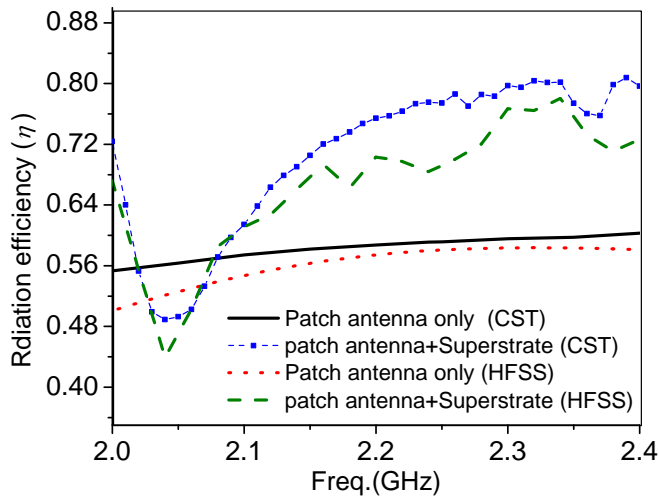
Figure 5.8: The radiation efficiency of the microstrip antenna covered with the artificial magnetic superstrate.

Table 5.1: The performance of the antenna with the magnetic superstrate at the resonance frequency of 2.2 GHz for different panel sizes (L is the patch antenna size)

Panel size	Gain (dBi)	Efficiency (%)
4X4 array (0.9 L)	6.3	65
6X6 array (1.4 L)	7.2	69
8X8 array (1.9 L)	8.15	74
10X10 array (2.3 L)	8.8	76
12X12 array (2.8 L)	9.14	73

5.3 Microstrip Antenna Array Covered With Artificial Magnetic Superstrates

In this section, we present two contributions. The first one is the application of the aforementioned SRR based superstrate to cover a planar antenna array for the enhancement of the gain and efficiency keeping the low-profile attractive feature of the microstrip circuits. The second contribution is modifying the analytical formulation explained in Chapter 2) to calculate the radiation field of the planar antenna array with and without the artificial superstrate. To validate the analytical results, numerical full-wave simulations will be presented. The simulation results will show a gain enhancement of about 3.5 dBi and an efficiency improvement of 10% for antenna array working in the UMTS band. As a practical perspective, high gain planar antenna arrays are used in sectorized cellular base stations to increase the frequency reuse factor and to reduce the co-channel interference. The proposed method (array with superstrate) is anticipated to combat some of the downsides of microstrip antenna arrays such as feed network losses and gain reduction due to surface waves.

As shown in Fig. 5.9(b), one layer of the superstrate is constructed by arranging a 44 X 24 array of SRRs. The superstrates consists of three layers of the SRR arrays, aligned in the x-y plane and separated from each other by 2 mm air layers, as depicted in Fig. 5.9(c). It may be noted that only z-directed magnetic fields are coupled to the superstrates layers.

The 4x1 antenna array used to demonstrate the gain and efficiency enhancement is shown in Fig. 5.9(d). The antenna elements (patches) are printed on a substrate of Rogers RO4350 with a thickness of 0.762 mm, relative permittivity of $\epsilon_r = 3.48$, and loss tangent of
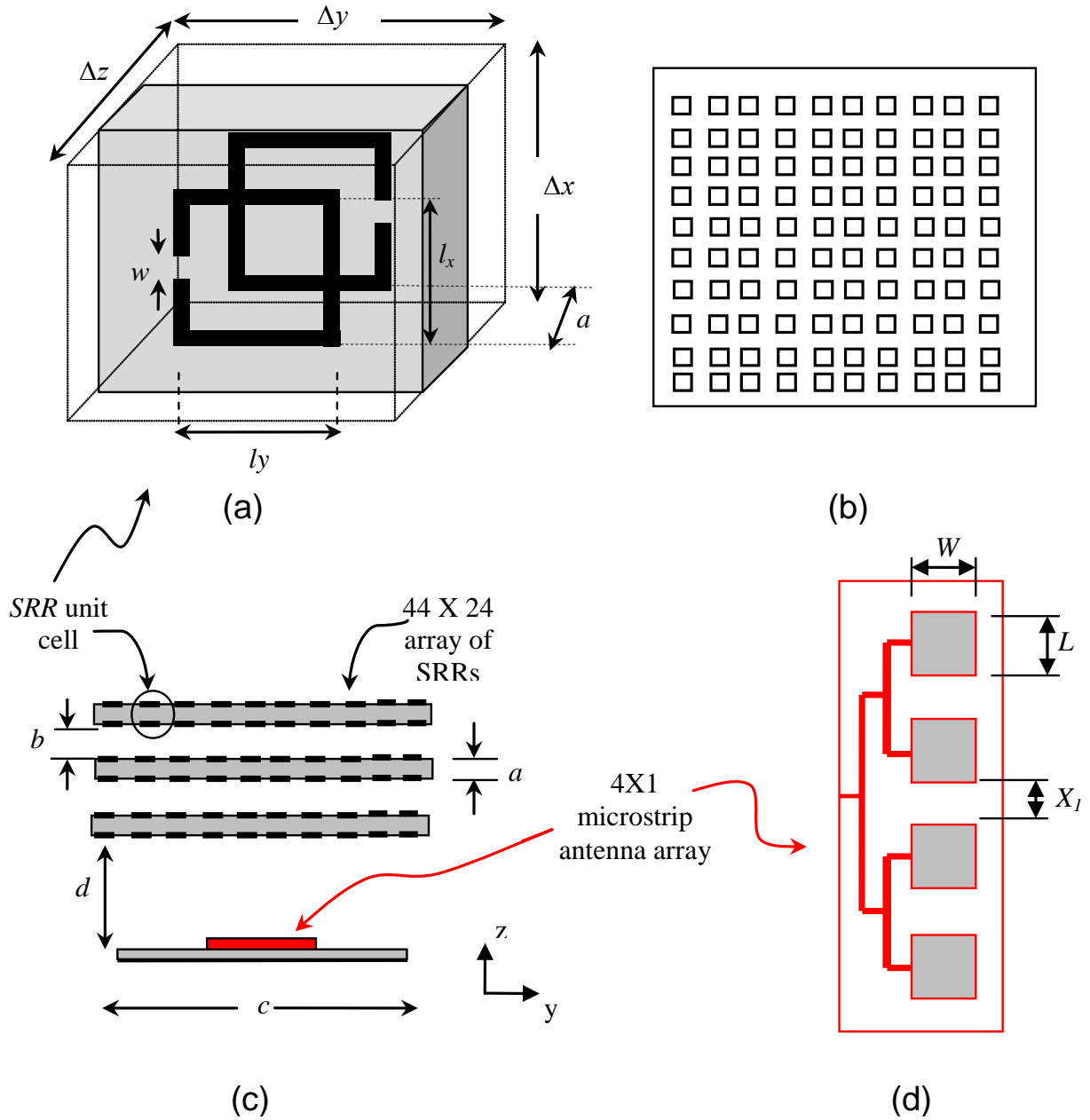
Figure 5.9: Geometry of a 4X1 microstrip antenna array covered by an engineered magnetic superstrate. (a) SRR unit cell. (b) Top view of the whole structure. (c) Side view of the whole structure. (d) Top view of a conventional 4X1 microstrip antenna array with $L = 45.5$ mm, $W = 36.4$ mm and $X_1 = 24.5$ mm. ($a = 0.762$ mm, $b = 2$mm, $c = 210$ mm and $d = 12$ mm)

$tan\delta = 0.004$. The separation between adjacent antenna elements is optimized for obtaining the highest gain. The antenna array is designed to operate at a resonance frequency of 2.18 GHz which lies in the UMTS band. The feeding network provides a zero progressive phase to the antenna elements to obtain broadside radiation. At the operating frequency, $\mu_{r_{eff}}$ and $\epsilon_{r_{eff}}$ of the superstrate are calculated using (4.24) and (4.26) to be 16 and 2.0, respectively.

The analytical formulation proposed in Chapter 2 is extended herein to calculate the radiation field of the 4X1 antenna array with and without the artificial superstrate. The electric field of a *single* patch antenna is calculated at the desired frequency using (2.19) and (2.21) and then integrated and multiplied by the array factor (AF) to find the directivity of any configuration of planar antenna arrays:

$$Directivity(\theta, \phi) = \frac{4\pi \ I \ [AF]^2}{\int_0^{2\pi} \int_0^{\frac{\pi}{2}} I \ [AF]^2 \ \ \sin(\theta)d\theta d\phi} \tag{5.1}$$

Where,

$$I = \cos^2(X)\frac{\sin^2(Y)}{Y^2} * (\sin^2(\phi)|N(\theta)|^2 + \cos^2(\phi)|Q(\theta)|^2) \tag{5.2}$$

$$X = \frac{K_0 L}{2}\sin(\theta)\cos(\phi), \qquad Y = \frac{K_o W}{2}\sin(\theta)\sin(\phi) \tag{5.3}$$

where L and W are the patch dimensions in the x and y directions, respectively (see Fig. 5.9(d)). The functions $N(\theta)$ and $Q(\theta)$ depend on θ only and they represent the current at $z = h$ in the transmission line analogy (Fig. 2.4) due to an incident current wave of strength $\cos(\theta)$ and 1, respectively.

In case of using (5.1) to calculate the directivity of *4X1 antenna array* covered with superstrate, the AF in this case would be:

$$AF = \cos(k_o \ y_1 \ \sin\theta \ \sin\varphi) + \cos(k_o \ y_2 \ \sin\theta \ sin\varphi) \tag{5.4}$$

Where y_1 and y_2 are design parameters of the 4X1 antenna array shown in Fig. 5.9(d):

$$y_1 = 1.5(X_1 + L), \quad y_2 = 0.5(X_1 + L) \tag{5.5}$$

A comparison study of the radiation patterns generated by the proposed analytical model (Eq. (5.1)) and CST software are depicted in Figs. 5.10, 5.11, 5.12 and 5.13. A good agreement between the two simulations methods is achieved despite the vast difference in the computational resources utilized by both methods. The analysis of the antenna array covered with engineered superstrate are performed using Intel(R) Core(TM)2 Quad CPU @2.83GHz machine, the proposed analytical technique requires 12 minutes and 370 megabytes of RAM using MATLAB, while the CST simulations for the same structure requires about 8 hours and 6 gigabytes of RAM when 45 cells/wavelength with total of 4.6 M mesh-cells were used for the entire structure. Hence, The proposed formulation (Eq. (5.1)) requires only 2.5% of the time acquired by full-wave analysis.

As discussed in the previous section, the distance between the antenna array and the superstrate was chosen such that a strong z-directed magnetic filed exists to excite the SRRs achieving the required high permeability of the superstrate. As shown in the gain plot given in Fig. 5.14, the gain in the broadside direction is improved by 3.5 dBi at the antenna resonance. The return loss, also depicted in Fig. 5.14, shows that the antenna array is matched to the feed-line, before and after the application of the superstrates. A slight change in the resonant frequency and the antenna bandwidth is observed because of the change in the near field properties of the antenna when the superstrates is added.

Fig. 5.15 provides the radiation efficiency of the antenna before and after the addition of the engineered superstrates. A 10% increase in efficiency shows that the losses due to surface waves are reduced. This can be understood by considering the inherent anisotropy of the band gap structure. To further illustrate the effect of superstrate on the antenna gain, a comparison of the E-plane and H-plane radiation patterns are provided in Figs. 5.16 and 5.17 , respectively. The overall radiation pattern shapes before and after the addition of superstrates are identical showing that the radiation in the principle planes of the antenna array is not disturbed.
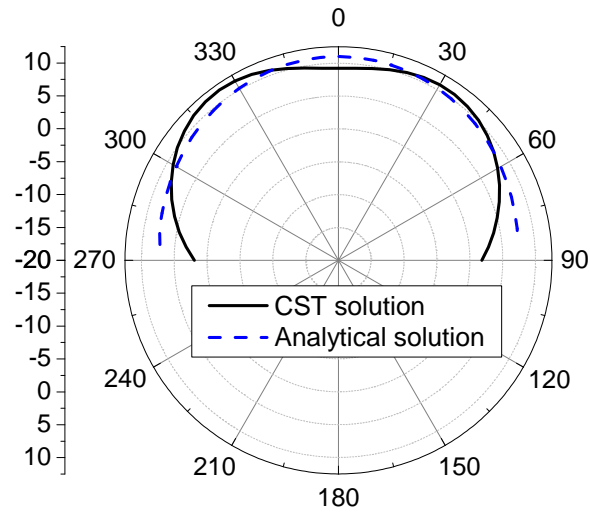
Figure 5.10: The E-plane directivity radiation pattern at 2.17 GHz of the 4X1 patch antenna array.
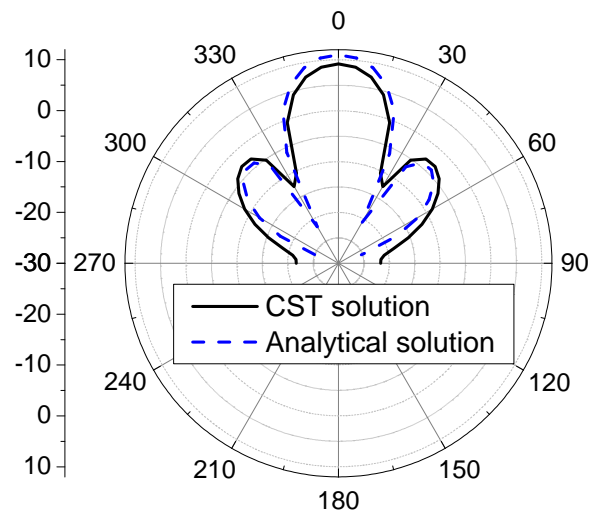
Figure 5.11: The H-plane directivity radiation pattern at 2.17 GHz of the 4X1 patch antenna array.
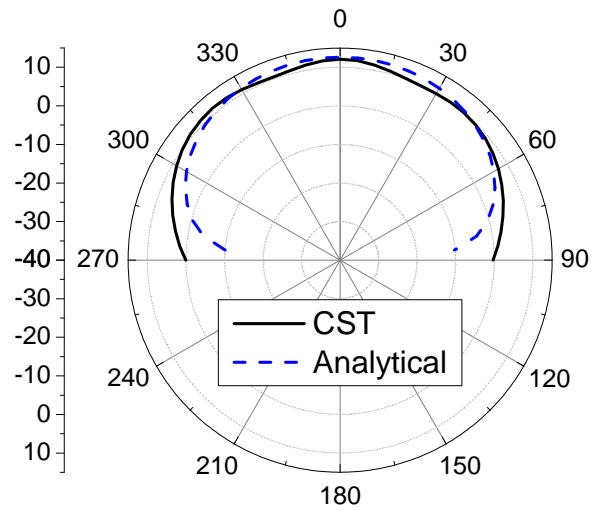
Figure 5.12: The E-plane directivity radiation pattern at 2.17 GHz of the 4X1 patch antenna array with the artificial magnetic superstrate.
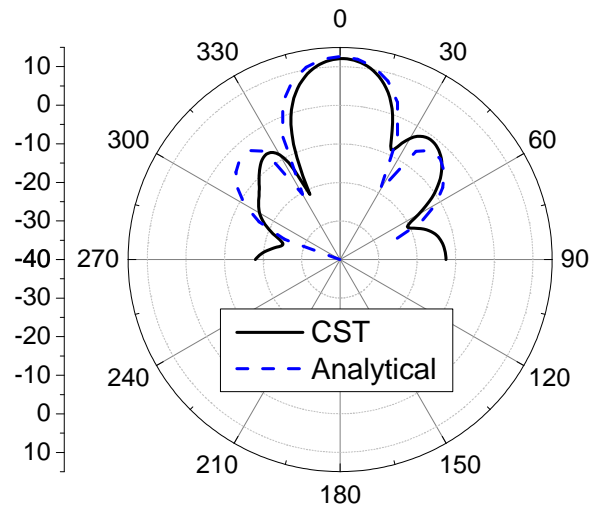
Figure 5.13: The H-plane directivity radiation pattern at 2.17 GHz of the 4X1 patch antenna array with the artificial magnetic superstrate.
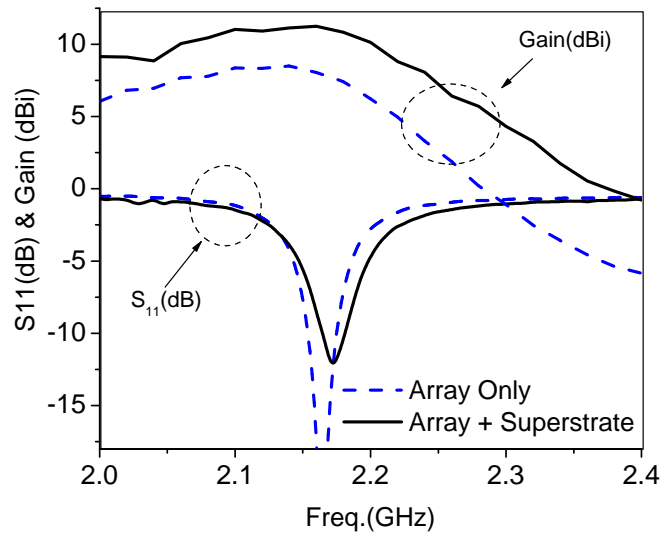
Figure 5.14: The return loss and gain of the microstrip antenna array before and after using the artificial magnetic superstrate.
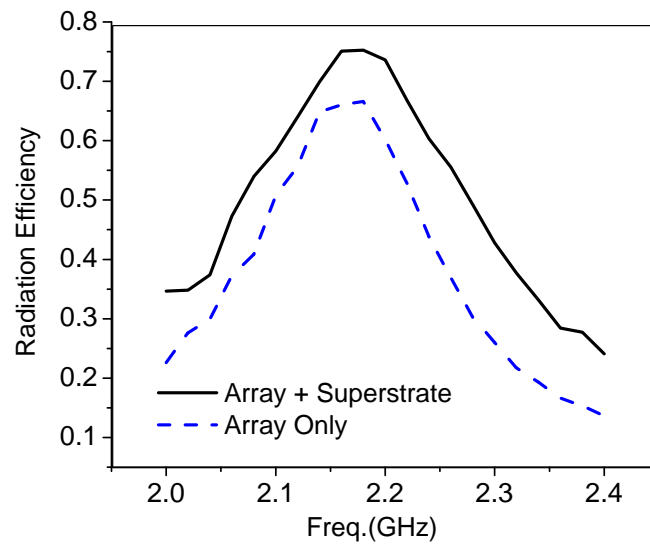
Figure 5.15: The radiation efficiency of the microstrip antenna array before and after using the artificial magnetic superstrate. (10% increase in the efficiency is achieved at 2.18 GHz)
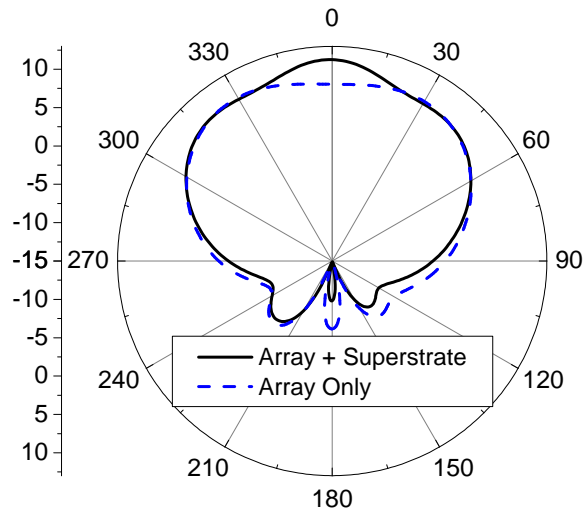
Figure 5.16: The E-plane radiation pattern of the microstrip antenna array before and after using the artificial superstrate.
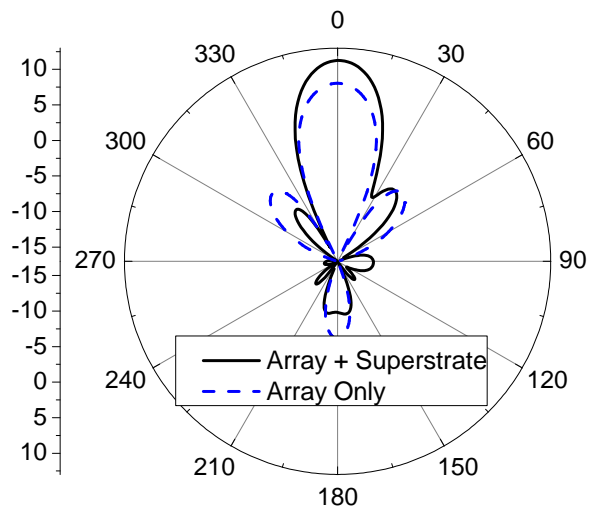
Figure 5.17: The H-plane radiation pattern of the microstrip antenna array before and after using the artificial superstrate.

5.4 Enhanced Gain Planar Inverted-F Antenna with Metamaterial Superstrate for UMTS Applications

One of the design constraints on the new mobile handset generation is antenna-size miniaturization, as more antennas need to be integrated in the same handset to support multiple standards. Furthermore, antennas need to maintain good performance in terms of bandwidth, gain, and radiation pattern. Planar inverted-F antennas (PIFA) are widely used in wireless hand-held devices due to their small-size, moderate bandwidth and radiation patterns [62]–[66].

Size reduction of PIFA antennas can be achieved using several techniques [67]–[70]. In [67], a small-size PIFA antenna operated at its one-eighth wavelength ($\lambda/8$) mode was proposed, the proposed PIFA constituted by two radiating strips of length about ($\lambda/8$) was fed using a coupling feed. Du et al. [68] used the idea of high-impedance surface to construct a photonic bandgap type (PBG-type) ground plan for a PIFA antenna in order to reduce the planar size of the antenna, the (PBG-type) ground plan was composed of a dielectric substrate on a metallic plate and an upper plate with periodically metallic patch overlays on the substrate. In [69], the impedance bandwidth of a miniature PIFA antenna was enhanced using very high permittivity superstrate ($\epsilon_r > 35$) without considering physical realization of the proposed superstrate. Another mechanism to miniaturize PIFA antenna is to have slots in the ground plane [70] to make the ground plane appear electrically longer. Although the slotted ground plane reduced the height of the antenna, this will add complexity in the design and housing of the mobile handset. Further, bandwidth becomes extremely narrow as antenna height is reduced. In [71], it was shown that the emitted power from current handset phones results in significant power loss absorbed by user's human head; thus decreasing the efficiency and possibly the gain of the antennas. While reducing the size of PIFA antennas is important, what is typically neglected is the consequential effects on the antenna gain and radiation patterns.

In this work, the engineered magnetic superstrate explained in the previous sections is used herein for gain enhancement of PIFA antennas. The designed artificial magnetic superstrate along with the PIFA antenna is numerically simulated, and the effect of the superstrate on gain, impedance bandwidth, and radiation patterns of the antenna is investigated. The total height of the proposed superstrate over the antenna is only $\lambda_0/14$

where λ_0 is the free-space wavelength at antenna's resonance frequency. Thus, the antenna structure remains low profile, and is advantageous in cell-phone applications.

The SRR unit cell has the same dimensions as mentioned in the previous section. A planar 12 x 12 array of SRRs was printed on the host dielectric layer to provide the engineered magnetic material as shown in Fig. 5.18. The PIFA antenna considered herein (see Fig. 5.19) consists of a rectangular planar element located above a ground plane, a short-circuiting plate or pin, and a feeding mechanism for the planar element. The planar radiating element used herein has dimensions of 24 mm x 8 mm, and is suspended on air substrate with a thickness of 8.5 mm. The antenna is fed using a coaxial probe feed and is shorted to the ground plane using a short-circuiting metallic pin of radius 0.35 mm. This metallic pin introduces inductance to antenna's equivalent circuit and hence reduces the planar size of the PIFA antenna to be used in cell-phones applications. The antenna is designed to operate within the frequency band of UMTS at which the magnetic superstrate has an effective permeability of about 16 (real part) and an effective permittivity of 2.0 (see Fig. 4.14).

The full-wave EM solver CST Microwave Studio was used to simulate the proposed antenna with and without superstrate. Fig. 5.20 shows the reflection coefficient of the PIFA
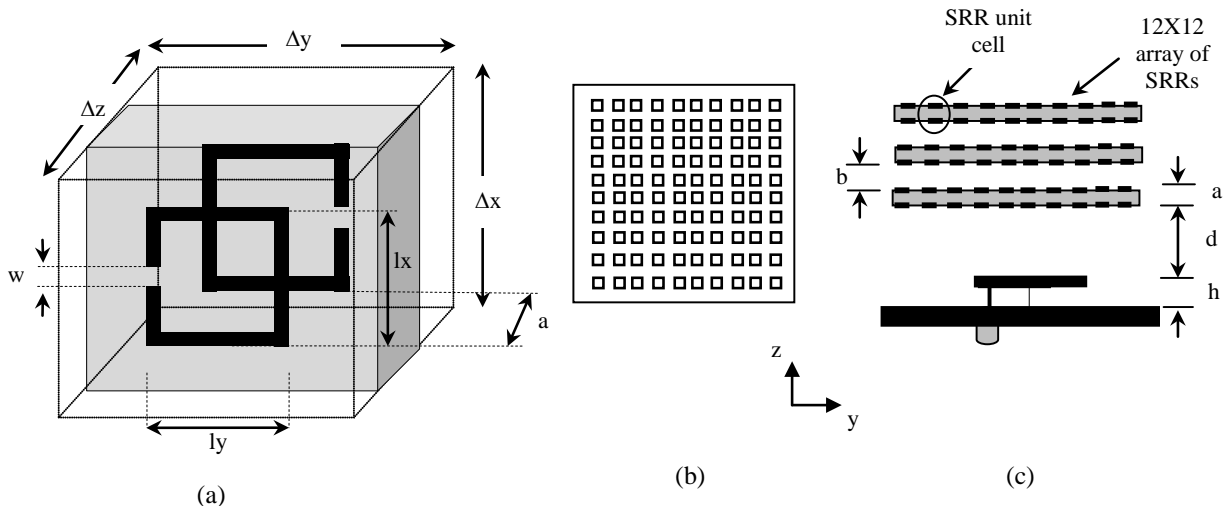
Figure 5.18: The proposed PIFA antenna covered with an engineered magnetic superstrate: (a) Unit cell. (b) Top-view. (c) Side-view. ($a = 0.762$ mm, $b = 2$ mm, $d = 4$ mm, and $h = 8.5$ mm)
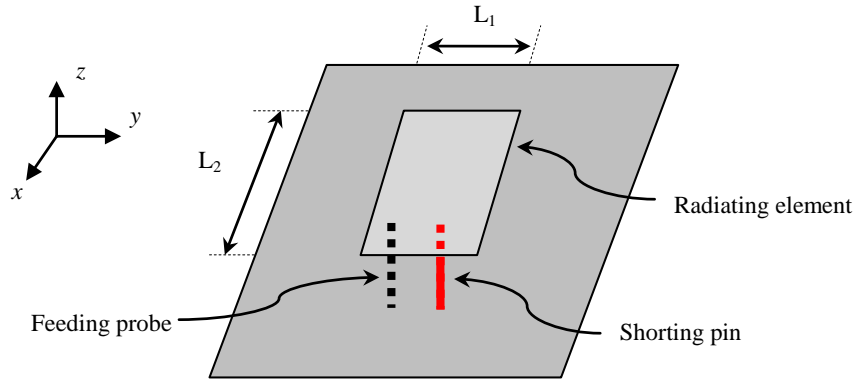
Figure 5.19: Geometry of the Planar PIFA antenna. ($L_1 = 8$ mm and $L_2 = 24$ mm)

antenna before and after using the artificial magnetic superstrate at the optimized distance of 4 mm from the substrate. The overall height of the superstrate above the antenna is only $\lambda_0/14$ where λ_0 is the free-space wavelength at the resonance frequency. As shown in Fig. 5.20, the antenna impedance bandwidth ($S_{11} < $ -10 dB) and the resonance frequency of 2.2 GH are slightly changed after using the metamaterial superstrate in comparison to the case without superstrate.

The distance between the PIFA antenna and superstrate was optimized numerically using CST to achieve the highest possible gain. Fig. 5.21 shows the gain of the PIFA antenna in the maximum radiation direction before and after using the artificial magnetic superstrate for different distances between the antenna and superstrate. It is observed that the gain is improved by 3.2 dBi at the resonance frequency after using the engineered superstrate at d = 4mm.

Figs. 5.22 and 5.23 show the E-plane and H-plane radiation patterns, respectively, these patterns are calculated at the resonance frequency (2.10 GHz) of the PIFA antenna before and after using the engineered magnetic superstrate at $d = 4$ mm, it is observed that the gain of the PIFA antenna is enhanced in the direction of maximum radiation after using the artificial magnetic superstrate.
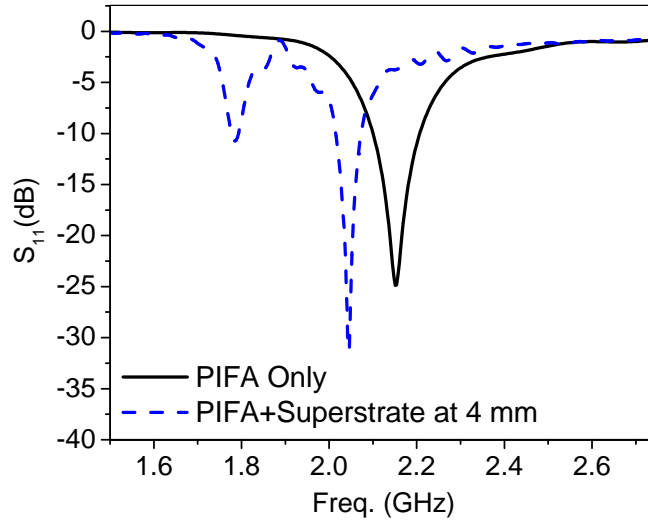
Figure 5.20: The return loss of the PIFA antenna before and after using the artificial magnetic superstrate.
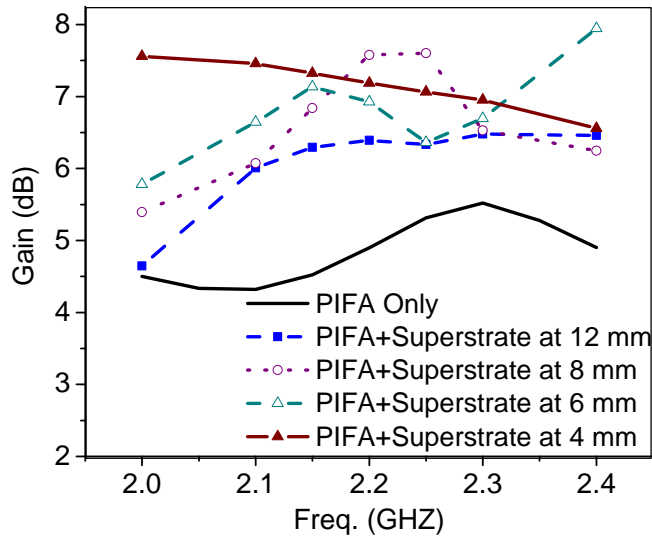
Figure 5.21: The gain of the PIFA antenna before and after using the artificial magnetic superstrate for different distances between the antenna and superstrate.
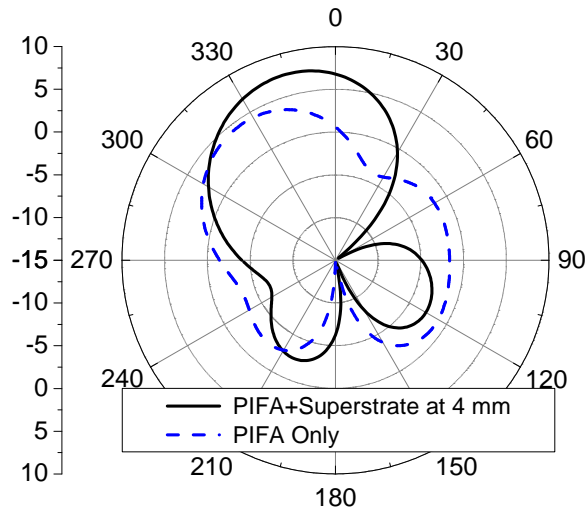
Figure 5.22: The E-plane ($\phi = 0^o$) gain radiation pattern at 2.10 GHz of the PIFA antenna before and after using the artificial magnetic superstrate at d=4 mm.
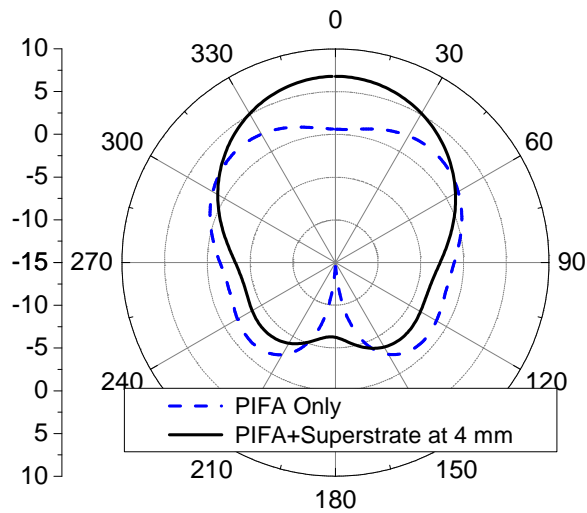

Figure 5.23: The H-plane ($\phi = 90^o$) gain radiation pattern at 2.10 GHz of the PIFA antenna before and after using the artificial magnetic superstrate at d=4 mm.

5.5   Concluding Remarks

An engineered magnetic superstrate was introduced for gain and efficiency enhancement of low-profile antenna. The engineered superstrate based on the broadside coupled split ring resonator SRR was analytically designed and characterized. The patch antenna covered with the engineered superstrate was experimentally and numerically investigated, and compared with the case of patch without superstrate. It was shown that for a patch antenna resonating at 2.2GHz, using the engineered magnetic superstrate results in a 3.8 dBi enhancement in gain and 14% enhancement in efficiency, while maintaining an antenna profile of $\lambda_0/7$. The planar size of the radiating system was only 2.3 times the patch size. These improvements were achieved while having an insignificant effect on the impedance bandwidth of the antenna.

Furthermore, a very fast and accurate analytical technique was developed to calculate the radiation field of a microstrip antenna covered with an artificial magnetic superstrate. The analytical formulation is based on using the cavity model to replace the patch antenna by two magnetic line sources. Then, the reciprocity theorem and transmission line analogy were used to calculate the far-field of these two magnetic line sources representing the patch antenna. The proposed analytical model was implemented and verified by a comparison with experiments and full-wave simulations. It is worth mentioning that the proposed analytical solution requires only 2.0% of the time acquired by the commercial software CST.

To further investigate the effect of superstrate on the performance of planar printed antennas, the aforementioned engineered magnetic superstrate constructed by split-ring-resonators was used to cover a 4x1 linear microstrip array to enhance its far-field properties. The distance between the patches and the superstrates is optimized to achieve a gain enhancement of about 3.5 dBi. The antenna properties such as radiation patterns and the return loss characteristics are not significantly affected by the superstrates. However, there is an improvement in efficiency of about 10%. An overall profile of $\lambda_0/7$ resulted when the superstrates is added, which is appreciably better than the other techniques of gain enhancements such as EBG based superstrates. The superstrate-based gain enhancement method can be used in commercial antenna arrays to combat some of the downsides of the existing systems such as gain decrease due to surface waves and dielectric losses. The analytical method based on reciprocity theorem and transmission line model was extended

to calculate the radiation field of the antenna array covered with artificial superstrate, the radiation patterns results are compared with the full-wave simulator CST and good agreement was achieved. The proposed formulation requires only 2.5% of the time acquired by full-wave analysis.

Another application for the SRR-based artificial superstrate is to enhance the gain of planar inverted-F Antenna (PIFA) which is commonly used in cell-phones applications. The PIFA antenna covered with the artificial superstrate was numerically investigated. It was shown that using the engineered magnetic superstrate, gain enhancement of 3.2 dBi is attainable, while maintaining a superstrate profile of $\lambda_0/14$ where λ_0 is the free-space wavelength at the PIFA's resonance frequency.

Chapter 6

Beam Steering of Patch Antennas Using High Refractive Index Superstrate

6.1 Introduction

In the previous chapter, a patch antenna *fully* covered with a superstrate was designed to enhance the gain and efficiency. In this chapter, we consider a novel implementation of the antenna-superstrate configuration in order to steer the antenna's main beam. As shown in Fig. 6.1(b) , the superstrate is displaced along the E-plane (x-y plane) of the patch such that it covers only one of the radiation slots of the patch antenna (according to the cavity model [50, 72]). In effect, the electromagnetic radiation from the covered radiating slot reaches the far-field with an additional phase with respect to the uncovered slot, resulting in an inclined beam whose angle depends on the superstrate's refractive index and thickness.

As shown in Fig. 6.1(b), the partial superstrate creates a phase-imbalance between the fields emitted by the two radiation slots in free space, thereby producing an off-broadside main beam. Thus the antenna-superstrate system acts as a two element phased array in which the phase is controlled by the refractive index and thickness of the superstrate. The off-broadside beam deflection is demonstrated using a superstrate with a high permittivity
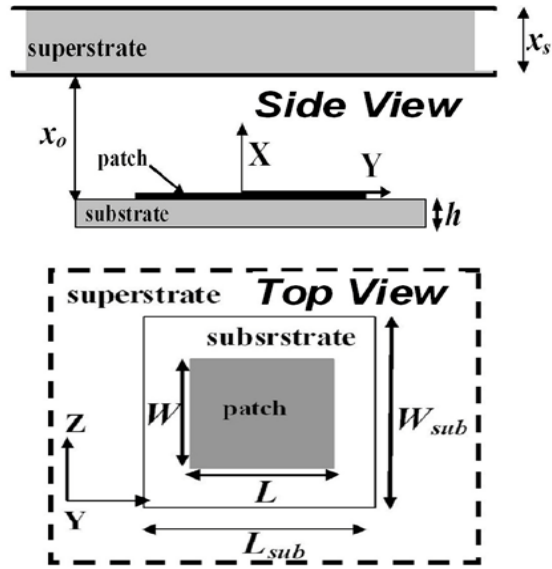
(a) Full-covered Patch
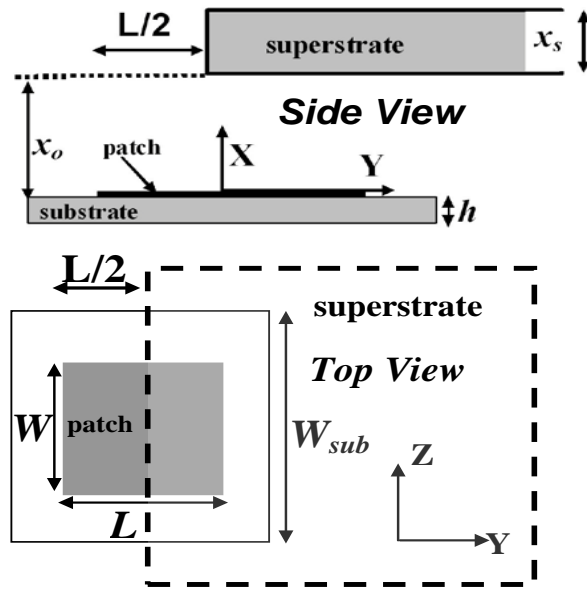
(b) Partially-covered Patch

Figure 6.1: The geometry of a microstrip antenna ($L = W = 36$ mm) which is (a) fully covered by a high refractive index superstrate and (b) partially covered by same superstrate.

that partially covers a microstrip patch antenna.

Beam steering has been traditionally implemented in antenna arrays using phase shifters which result in complex structures and suffer from high loss and mass [73]–[77]. On the other hand, the proposed method of beam steering is cheaper and easier to implement by partially covering the patch with a high refractive index superstrate. Moreover; the antenna directivity and gain are enhanced. Full-wave simulations are employed to show beam deflections up to 37 degrees in the presence of high refractive index superstrates. Analytically, the beam angle is predicted by using plane-wave approximations and ray-tracing technique which is very fast method to calculate the radiation patterns of such radiating systems. Experimentally, a beam deflection of 25 degrees is achieved when a microstrip patch is partially covered with a superstrate having a dielectric constant of 10.

It should be noted here that the beam steering that was demonstrated in the contemporary superstrate-covered antennas [78] takes place due to the secondary radiation by the unit cells forming the superstrate layer. On the other hand, the proposed configuration utilizes the dual-aperture radiation mechanism of the microstrip antenna and the superstrate only produces a phase difference between the two radiation slots. With the possibility of tunable artificial superstrates, which can be developed by implementing varactors in metamaterial structures [79]], a novel method of beam steering can be implemented as an alternate solution to the phase shifting networks.

6.2   Fully-Covered Patch Antenna

Consider first a single patch element (see Fig. 6.1(a)) which is fully covered by a superstrate of relative permeability of μ_2 and relative permittivity of ϵ_2. The patch is designed to resonate at 2.18 GHz when placed on a substrate of 0.762 mm thickness and 3.48 dielectric constant. The superstrate has thickness $x_s = 6.28$ mm and is placed at $x_o = 12$ mm (corresponding to $\lambda_o/11$, where λ_o is the free-space wavelength). It follows from the cavity model [48] that the two radiation slots of the microstrip antenna (located along the y-axis) can be modeled as two magnetic dipole sources separated by the effective patch length forming a two element array.

The plane wave propagation geometry depicted in Fig. 6.2 shows the equivalent array geometry when the ground plane is replaced by the images of the magnetic sources. Since
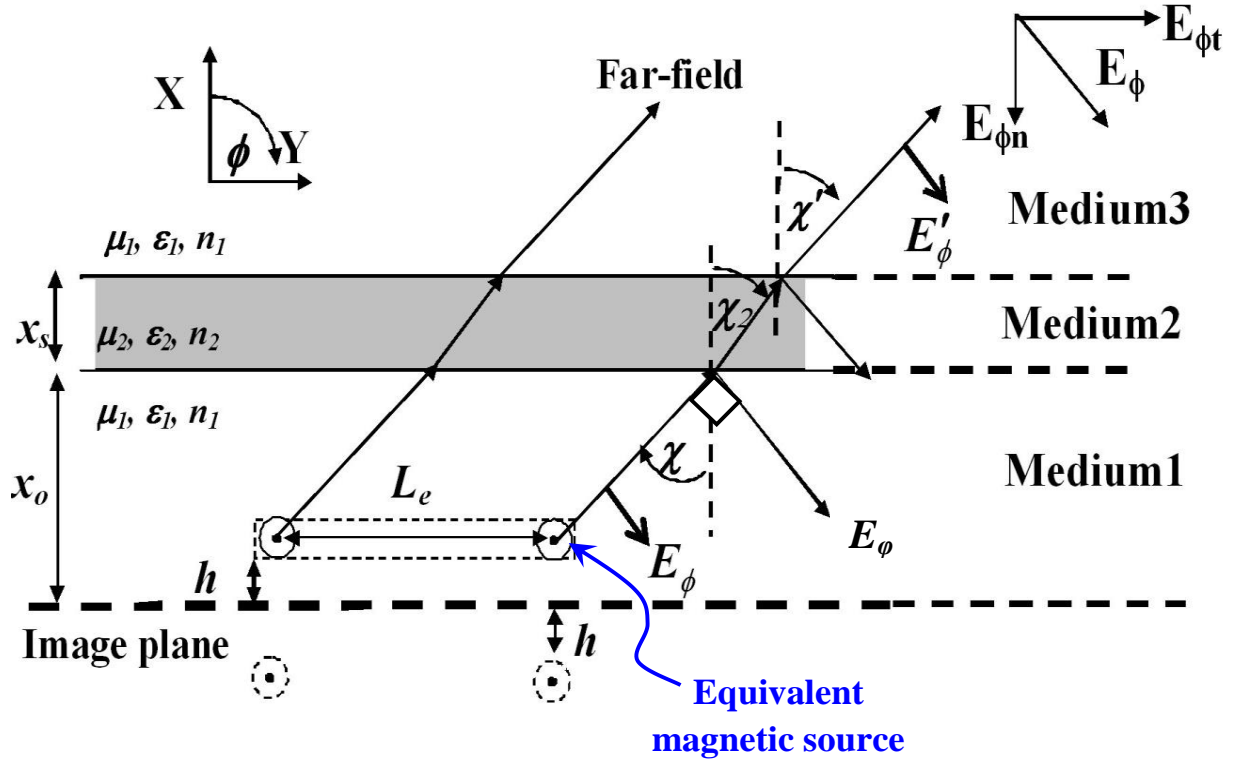
Figure 6.2: Equivalent plane-wave geometry of a microstrip patch antenna fully covered by a superstrate. The microstrip antenna is replaced by two equivalent magnetic sources and ground plane is replaced by their images.

$h << \lambda_o$, the fields of the source and image can be added in phase, resulting in the following value for the normalized far-field in the principal E-plane *in the presence of the superstrate* [72]:

$$E_{\phi t} = j \frac{k_1 W h E_o e^{-j k_1 r}}{\pi r} \; \frac{\sin \frac{k_1 h}{2} \cos \phi}{\frac{k_1 h}{2} \cos \phi} \; \left[\frac{1 + e^{j k_1 L_e sin(\phi)}}{2} \right] \; T_{TM} \qquad (6.1)$$

The term in the square brackets represents the array factor. E_o is the amplitude of electric field in the radiation slot, K_1 is the propagation constant of the free space, and L_e is the effective length of the microstrip antenna with the fringing effects taken into account. Noting that the plane waves incident upon the superstrate have a transverse magnetic polarization (TM) in the plane of incidence (E-plane) [72]. (T_{TM}) in the above equation is the angle-dependent *overall transmission response* from medium 1 to medium

3 and is obtained by imposing the matching conditions on the transverse phase and electric field-vectors at the interfaces [80]:

$$T_{TM} = \frac{E'_\phi \cos \chi'}{E_\phi \cos \chi} = \frac{\tau_1 \tau_2 e^{-jk_{2n}x_s}}{1 + \rho_1 \rho_2 e^{-j2k_{2n}x_s}} \tag{6.2}$$

where χ and χ' are the angles which the incident and transmitted rays respectively make with the normal. x_s is the thickness of the superstrate. k_{2n} is the component of the phase constant that is normal to the medium 2 - medium 3 interface and is given by $\omega.n_2.\cos(\chi_2)/c$ (where ω is the angular frequency, c is the speed of light in free space and rest of the parameters are defined in Fig. 6.2). ρ_1 and ρ_2 are the reflection coefficients of the transverse fields at the medium 1 - medium 2 and medium 2 - medium 3 interfaces respectively and are defined by (in case of TM wave):

$$
\begin{aligned}
\rho_1 &= \frac{\eta_2 \cos \chi_2 - \eta_1 \cos \chi}{\eta_2 \cos \chi_2 + \eta_1 \cos \chi} \\
\rho_2 &= \frac{\eta_3 \cos \chi' - \eta_2 \cos \chi_2}{\eta_3 \cos \chi' + \eta_2 \cos \chi_2}
\end{aligned}
\tag{6.3}
$$

where η_1, η_2 and η_3 are the intrinsic impedance of medium 1, 2 and 3, respectively. In the case of having medium 1 and medium 3 as air then $\eta_1 = \eta_3$.

τ_1 and τ_2, given by $\tau_1 = \rho_1 + 1$ and $\tau_2 = \rho_2 + 1$, are the transmission coefficients on the above mentioned interfaces. The angle of refraction (χ_2) is obtained by applying Snell's law ($n_3 \sin \chi' = n_2 \sin \chi_2$) at the medium 2 - medium 3 interface. Also, as medium 1 and medium 3 are assumed to be free space, $n_1 = n_3 = 1$ which implies that the angle $\chi = \chi'$. Equation (6.2) then provides the relationship between the total transmitted and incident fields (through the superstrate). Also, note that in case of ($\eta_1 = \eta_3$ and $\chi = \chi'$) then $\rho_1 = -\rho_2$.

The *overall reflection response* through the superstrate (medium 2) can be calculated as [80]

$$R_{TM} = \frac{\rho_1 + \rho_2 \ e^{-j2k_{2n}x_s}}{1 + \rho_1 \rho_2 e^{-j2k_{2n}x_s}} \tag{6.4}$$

The transmission and reflection responses (Eqs. 6.2 and 6.4) of the superstrate slab are plotted with respect to the angle of incidence (χ) in Fig. 6.3. As shown, the transmission
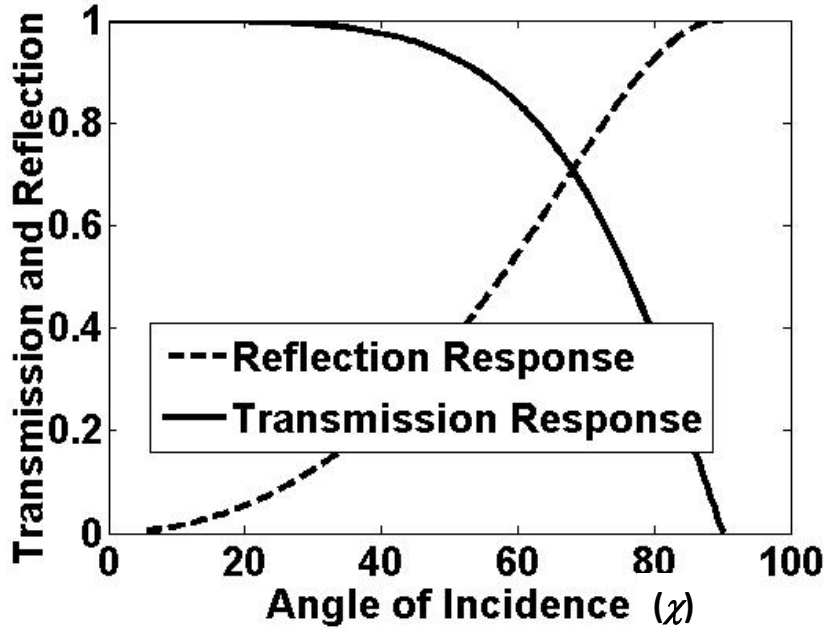
Figure 6.3: Dependence of the transmission and reflection responses of the superstrate on the angle of incidence (χ)

response decreases as the angle of incidence increases. At angles close to end-fire, when the reflection response maximizes, the transmission response is almost negligible. This angle-dependent transmission response (T_{TM}) constitutes towards the directivity increase of the antennas covered with a high refractive index superstrates.

The far-zone electric field calculated by the HFSS simulator and the plane-wave approximation (Eq. 6.1) are compared in Fig. 6.4. A slight directivity enhancement that increases with the refractive index is observed which is caused due to the nature of the transmission response of the air-superstrate. In effect, the radiated fields are suppressed in end-fire directions resulting in the enhanced directivity in the broadside direction. Further increase in directivity is possible with higher values of intrinsic impedance of superstrate or by optimizing the antenna-superstrate separation. Note that the electric fields along the end-fire directions in the HFSS model decay rapidly due to the finite ground plane resulting in the E-plane pattern that appears more directive.
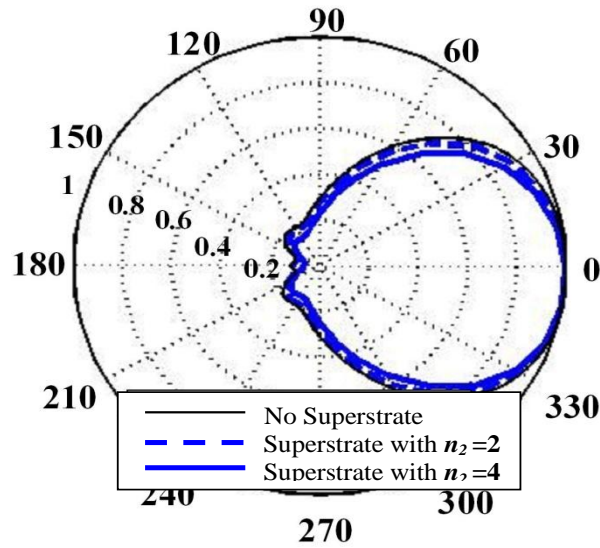
(a) HFSS Simulation
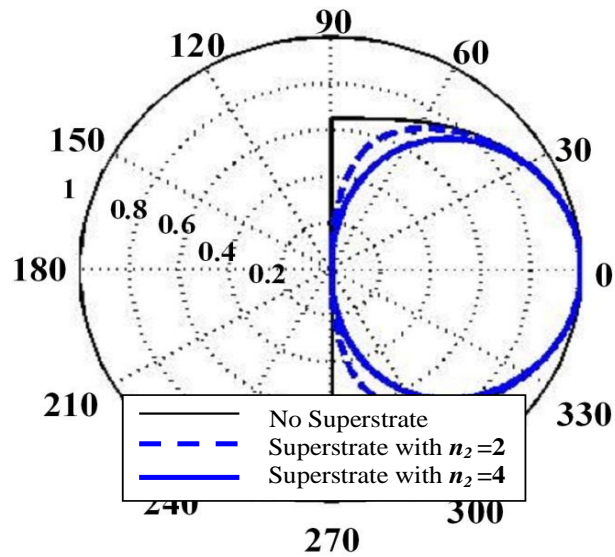
(b) Plane-wave model

Figure 6.4: E-plane radiation patterns of a microstrip antenna that is fully covered with a superstrate showing directivity increase with increase in the superstrate's refractive index.

6.3 Partially-Covered Patch Antenna

Consider next the case when the superstrate is shifted along the E-plane (x-y plane) to cover only half of the patch, as depicted in Fig. 6.1(b). Along certain observation angles (ϕ) in the far-field, the plane-waves arriving from the two sources travel through the superstrate and hence are phase delayed by an angle that is dependent on the refractive index and thickness of the superstrate. The superstrate is assumed to be semi-infinitely extended along ($+y$) axis to simplify the derivation of the radiation field in this case when the patch is partially covered with the superstrate.

Considering three angular ranges for the angle (ϕ) which cover the upper half space in order to explore the phased-array effect of the patch partially covered by a superstrate. These three ranges are explained as follows:

In the ***first angular range*** ($\phi_2 \leq \phi \leq \phi_1$), the radiation from equivalent source No. 1 (see Fig. 6.5 where ϕ_1 and ϕ_2 are defined) does not travel through the superstrate and hence does not suffer any extra phase shift. On the other hand, radiation from source No. 2 travels through the superstrate and hence suffers from an extra phase shift needed for the phased-array effect. Fig. 6.6 shows the ray-tracing geometry for this angular range of ϕ.

In the ***second angular range*** ($\phi_1 < \phi < \pi/2$), the radiation from *both* sources travels through the superstrate and hence suffers from an extra phase shift needed for the phased-array effect. Fig. 6.7 shows the ray-tracing geometry for this angular range of ϕ.

In the ***third angular range*** ($3\pi/2 < \phi < \phi_2$), the radiation from *both* sources does not travel through the superstrate and hence does not suffer from any extra phase. Fig. 6.8 shows the ray-tracing geometry for this angular range of ϕ.
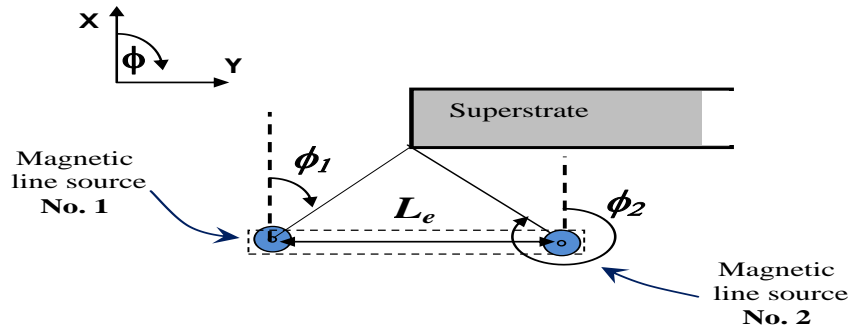
Figure 6.5: The geometric definitions of angles ϕ_1 and ϕ_2 which define the angular range in which the array-effect takes place in the far-field.
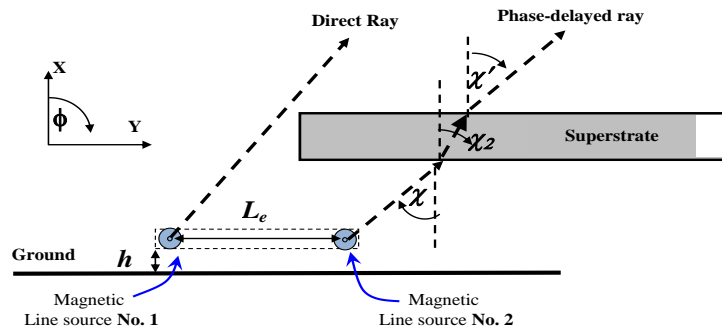
Figure 6.6: The ray-tracing geometry of the phased-array effect when the radiation from one source is phase delayed from that of the other source due to the presence of superstrate.
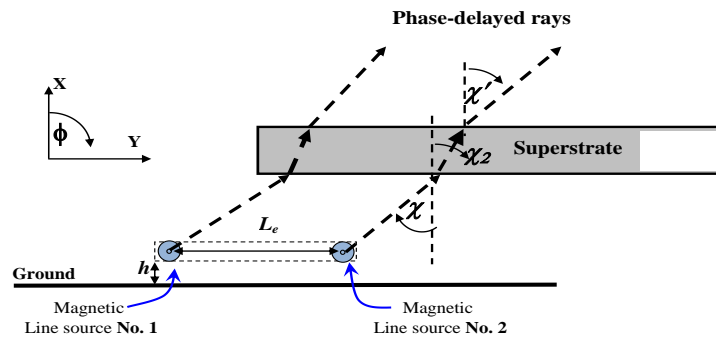
Figure 6.7: The ray-tracing geometry when radiation emitted by both of the sources passes through the superstrate before reaching the far-field.
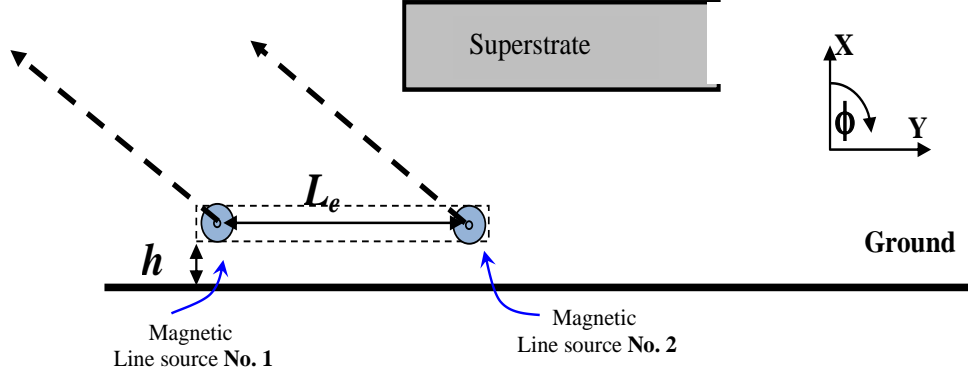
Figure 6.8: The ray-tracing geometry when radiation emitted by both of the sources does not suffer an additional phase shift.

Enforcing the plane-wave approximations and ignoring the diffraction and scattering from the superstrate edges, the radiation field in the above three angular ranges can thus be written as:

$$
\begin{aligned}
E_{\phi t} &= E_{\phi s}\left(e^{-j\ k_{1N}\ x_s} + T_{TM}\ e^{jk_1 L_e \sin\phi}\right), & \phi_2 \leq \phi \leq \phi_1 \\
E_{\phi t} &= T_{TM}\ E_{\phi s}\left(1 + e^{jk_1 L_e \sin\phi}\right), & \phi_1 < \phi < \pi/2 \\
E_{\phi t} &= 0, & \pi/2 < \phi < 3\pi/2 \\
E_{\phi t} &= E_{\phi s}\left(1 + e^{jk_1 L_e \sin\phi}\right), & 3\pi/2 < \phi < \phi_2
\end{aligned}
\tag{6.5}
$$

where $E_{\phi s}$ is the field emitted by single radiation slot and k_{1N} is the normal component of the propagation constant in free space and equals $k_1 cos(\chi)$.

We note in (6.5) that along certain observation angles, the electromagnetic waves emitted by the covered slot undergo an additional phase shift equal to the product of the superstrate's thickness x_s and the normal component of the propagation constant inside the superstrate. From the array theory, this phase difference between the slots translates into the main-beam deflection, as depicted in the field patterns of Fig. 6.9. The beam angle increases as the refractive index of the superstrate is increased and more phase shift incurs inside the superstrate layer. In particular, the direction of the main lobe is given by 23° and 37° from HFSS simulation and 10° and 28° from the plane-wave method (Fig. 6.9(b)) for the refractive indices of 2 and 4, respectively. The plane-wave model predicts

lower beam tilts and less-directive broader patterns due to the semi-infinite superstrate assumption. Furthermore, sharp edges are seen in the plane-wave model patterns which are partly due to the omission of near field effects in the model (such as scattering and diffraction from the superstrate).

The finite ground effect can be incorporated in (6.5) by obtaining the single slot pattern $E_{\phi s}$ from the full wave simulations. Hence, the radiation field in the last two angular limits of (6.5) can then be combined to give:

$$E_{\phi t} = E_{\phi s} \left(1 + e^{jk_1 L_e \sin \phi}\right), \qquad \qquad \pi/2 < \phi_1 < \phi_2 \qquad (6.6)$$

With finite ground plane assumption (see Fig. 6.9(c)), radiation patterns are more directive and the beam angles are closer to those obtained using the full-wave simulation HFSS (Fig. 6.9(a)). This good agreement between the proposed plane-wave model and HFSS is obtained despite the huge difference in computational resources used by the two methods. The proposed model consumed only 1/100 of the time taken by HFSS.

(a) HFSS

(b) Plane-wave model infinite ground plane

(c) Plane-wave model finite ground plane
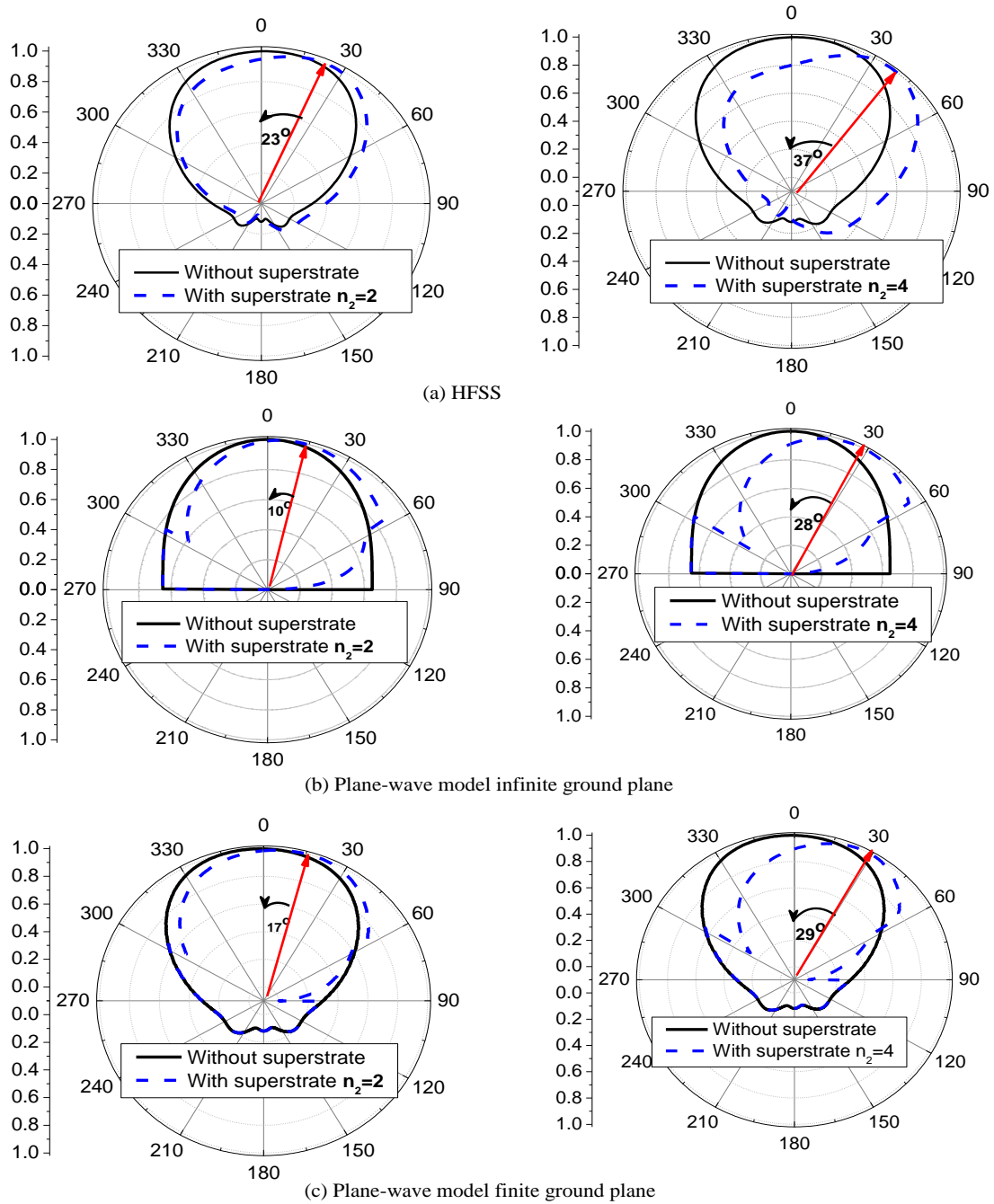
Figure 6.9: E-plane patterns of a patch antenna partially covered by a superstrate, obtained from (a) HFSS simulations (b) Plane-wave model (Eq. 6.5) assuming infinte ground plane and (c) Plane-wave model (Eqs. 6.5 and 6.6) assuming finite ground plane.

A comparison of electric field distributions (near fields) detected above the superstrate (provided in Fig. 6.10) corroborates the above mentioned concepts. Intense fields in the center and rapid roll-off show higher directivity for the fully-covered patch ($n_2 = 4$) when compared with the patch-only case. With the partially-covered patch ($n_2 = 4$), the high-intensity spot moves in the direction of the superstrate's displacement, signifying the moving of the main beam.

No Superstrate **Fully-Covered Patch n_2=4**

Partially-Covered Patch n_2=4
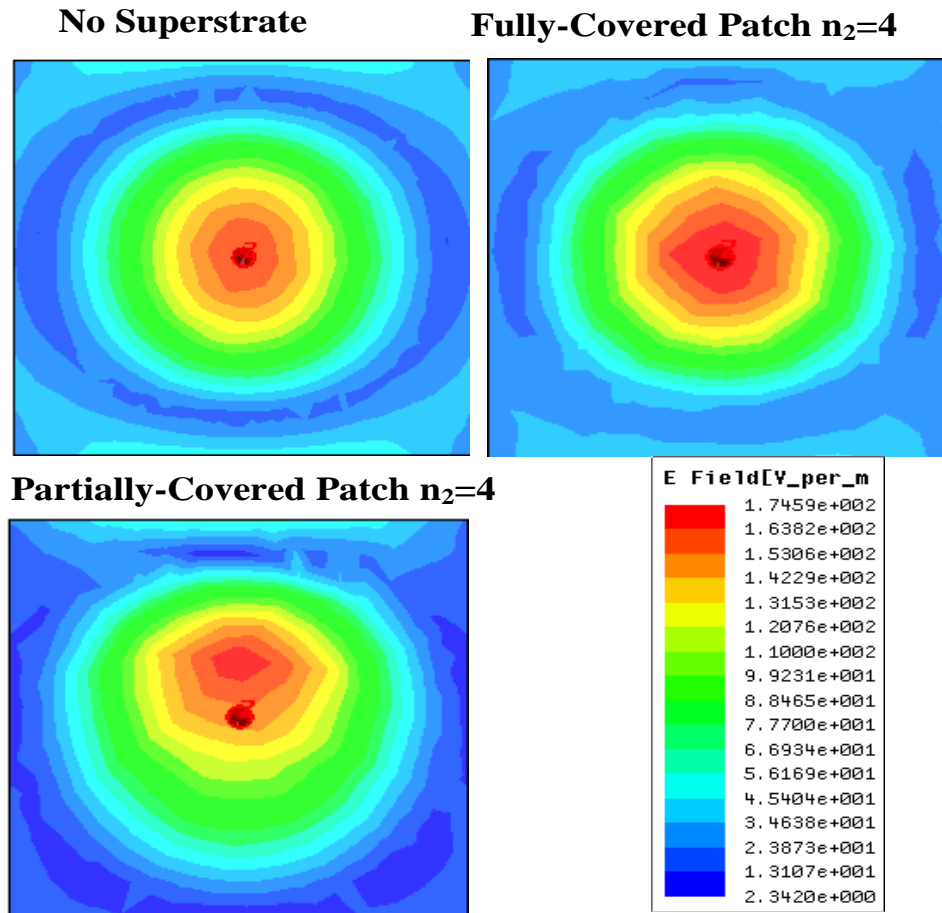
Figure 6.10: A comparison of electric field distributions detected at 57 mm (λ_o / 2.4) above the patch.

To observe the matching characteristics of the antenna-superstrate configuration, the reflection coefficient (S_{11}) plots for the three cases are provided in Fig. 6.11. The S_{11} plots show that the patch antenna remains matched under all three situations. However, a

slight displacement in the resonant frequency indicates the variation in the input impedance because the superstrate then perturbs the antenna's near-field.
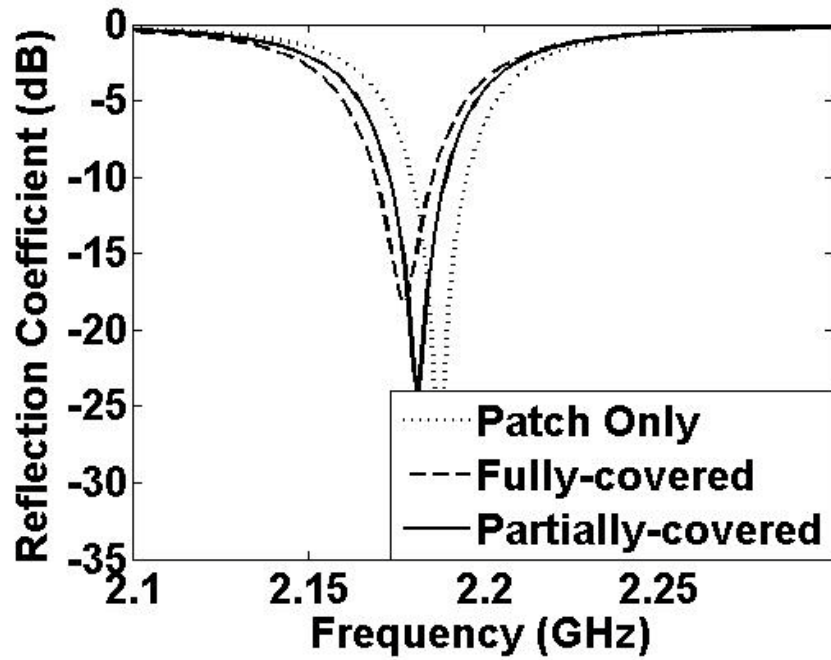
Figure 6.11: Reflection coefficient of the patch without superstrate and with superstrate showing good matching.

6.4 Experimental Results

The concept of beam steering is verified by fabricating a microstrip patch antenna that is resonant at 2.2 GHz. The dimensions of the patch and the substrate are similar to the one used in the HFSS simulations in the previous sections. As shown in Fig. 6.12, *half* of the patch is covered with a superstrate of Rogers RO3010 having a relative permittivity of 10.2, loss tangent of tan = 0.0035 and a thickness of 6.4 mm. The superstrate was fabricated by stacking five layers of Rogers RO3010 having standard thickness of 1.28 mm. The partial superstrate was placed at 12 mm from the patch antenna. The photographs of the experimental set-up are provided in Fig. 6.12.

The gain radiation patterns are measured using Agilent E5062A ENA Series RF Network Analyzers in an anechoic chamber. A comparison between the radiation patterns obtained from HFSS and measurement is depicted in Fig. 6.13 for the patch antenna before and after using the superstrate. A strong deflection of 25^0 in the E-plane (plane of superstrate displacement) is observed after using the superstrate. The HFSS results agree well with the measurement. Furthermore, the gain in the direction of main beam (highest radiation) was *increased* by 3.14 dBi after using the superstrate (see Fig. 6.13).

In the E-plane pattern shown in Fig. 6.13, the 3-dB beam-width for the patch antenna is 92° compared with 59° for the patch antenna partially covered with the superstrate. The reduction in the 3-dB beam-width is an indication of the improved directivity in the direction of main beam (highest radiation) and the sharpening of the radiation pattern's main lobe.

Fig. 6.14 shows a comparison of E-plane gain radiation pattern obtained from HFSS and experiment for a patch antenna *fully* covered with a superstrate of Rogers RO3010 at distance of 12 mm from the patch. By comparing Fig. 6.13(a) and Fig. 6.14, it is obvious that the gain at $\theta=0$ is *improved* by 4.3 dBi after fully covering the patch with a superstrate of Rogers RO3010. Also, no beam deflection is observed due to the fully coverage mechanism.
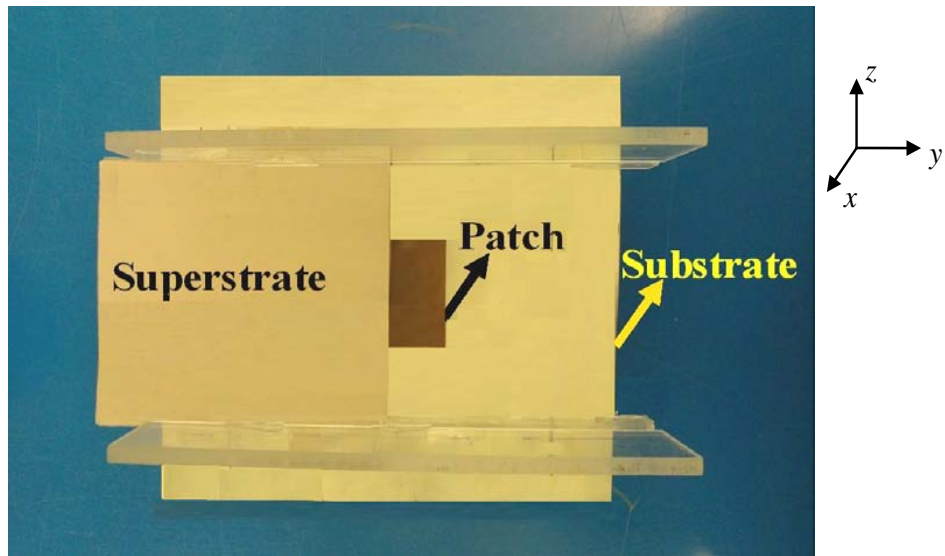
(a) Top View
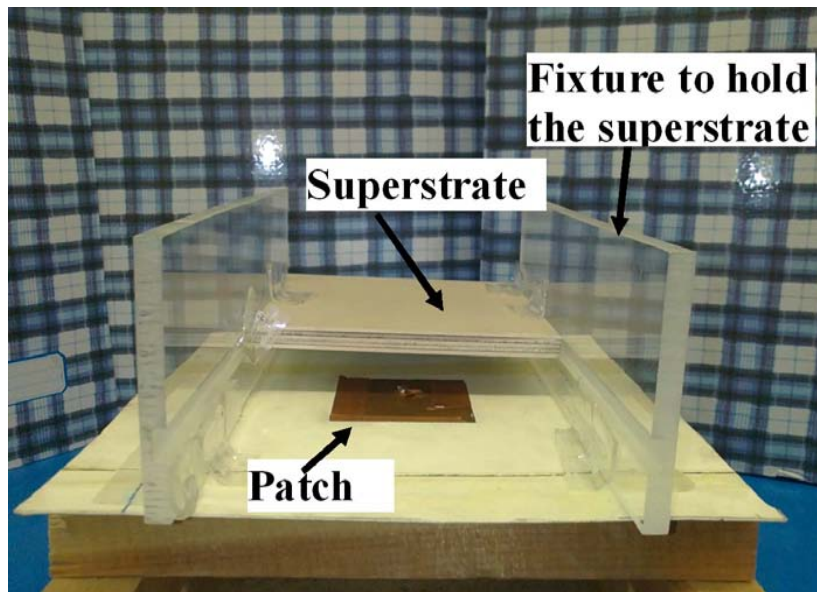
(b) Side View

Figure 6.12: Set-up of the beam steering experiment. (a) Top view of the superstrate partially covering a microstrip patch (b) side view.
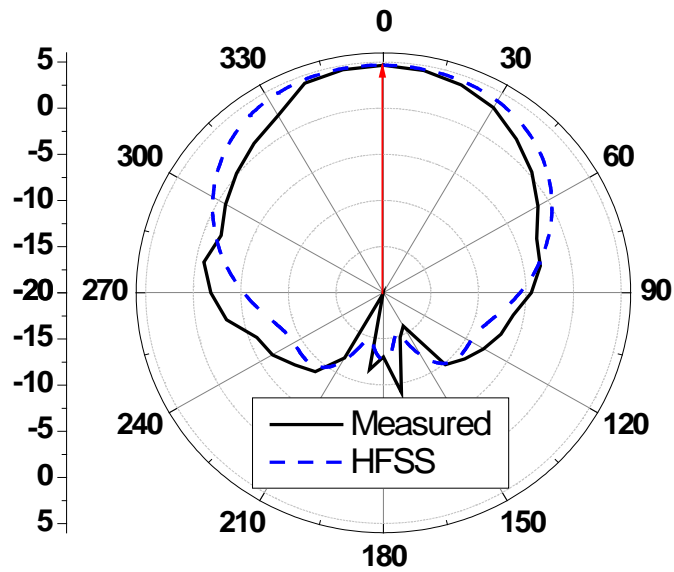
(a) Patch antenna only
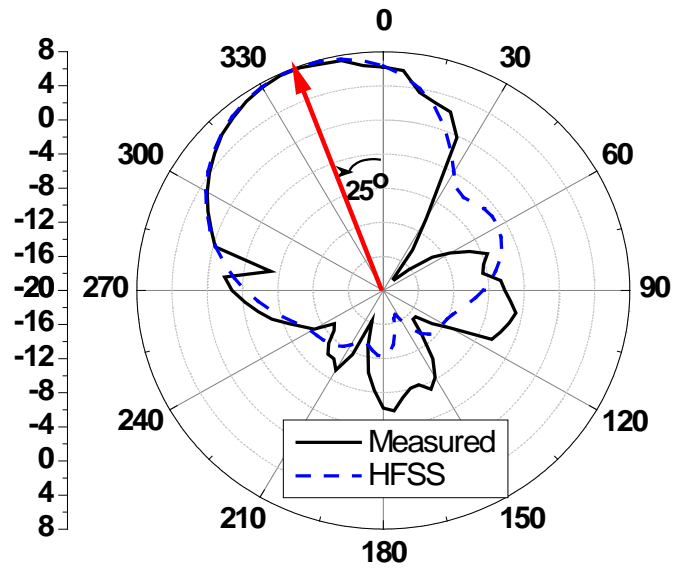
(b) Patch partially covered with superstrate

Figure 6.13: Comparison of E-plane gain radiation pattern obtained from HFSS and experiment. (a) Patch antenna only. (b) Patch antenna partially covered with a superstrate of Rogers RO3010 at distance of 12 mm from the patch.
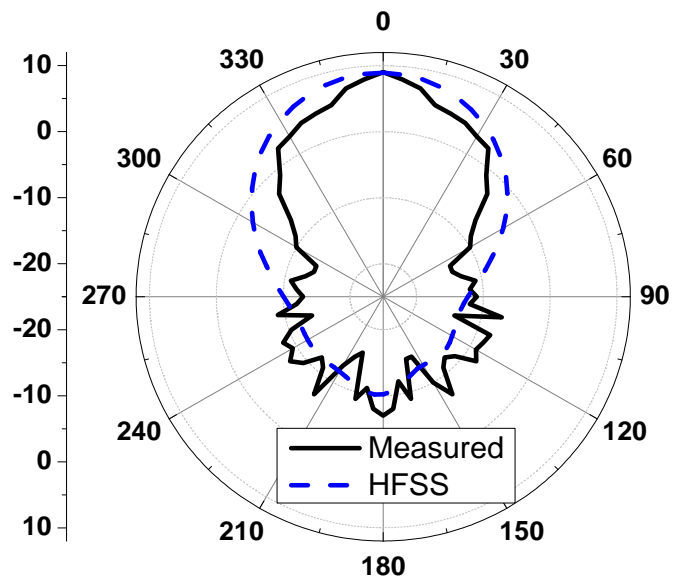
Figure 6.14: Comparison of E-plane gain radiation pattern obtained from HFSS and experiment for a patch antenna *fully* covered with a superstrate of Rogers RO3010 at distance of 12 mm from the patch.

6.5   Concluding Remarks

A novel mechanism of steering the main beam of a microstrip antenna, using high refractive index superstrate, was presented. Moreover; the antenna gain and directivity were enhanced. The proposed configuration consists of the high refractive index superstrate partially covering the patch such that one of the radiation slots is exposed. Through full-wave simulations, the main beam of the antenna is shown to deflect to higher angles as the refractive index of the superstrate is elevated.

The radiation mechanism was investigated by plane wave approximations and antenna array theory, the two radiation slots act as a two element array with a phase disparity that is created by the placing of the superstrate layer on one of the slots. A good agreement between the proposed plane-wave model and HFSS was obtained despite the huge difference in computational resources used by the two methods. The proposed model consumed only 1/100 of the time taken by HFSS.

Experimental results were presented to support the proposed mechanism of beam steering which can be of commercial value when used in antenna array systems for radar applications. With tuneable superstrate, a reconfigurable beam steerable microstrip patch can be obtained.

Chapter 7

Conclusions and Future Work

7.1 Summary and Contributions

In this dissertation, several advances to the present state of the art of gain enhancement and beam steering techniques of planar antennas have been developed and presented. These advances include introducing of a new approach to improve the radiation properties of planar antennas using artificial magnetic superstrates and the development of a very fast analytical solution for the radiation field of planar antennas when embedded in multilayered artificial periodic structure.

In summary, this dissertation presented the following contributions in the area of planar antennas integrated with artificial magnetic materials:

- A very fast and accurate analytical solution for the radiation field of a microstrip antenna loaded with a generalized superstrate was developed using the cavity model of microstrip antennas in conjunction with the reciprocity theorem and the transmission line analogy. The proposed analytical formulation for the antenna's far-field is much faster when compared to full-wave numerical methods. It only needs 2% of the time required by full-wave analysis. Therefore the proposed method can be used for design and optimization purposes. The method was verified using both numerical and experimental results. This verification was done for both conventional isotropic dielectric superstrates, and also for artificial periodic superstrates. The analytical

formulation introduced here can be extended for the case of a patch antenna embedded in a multilayered artificial dielectric structure. To the best of our knowledge, the proposed analytical technique is applied for the first time for the case of a practical microstrip patch antenna working in the Universal Mobile Telecommunications System (UMTS) band and covered with a superstrate made of an artificial periodic metamaterial with dispersive permeability and permittivity.

- The transmission line theory and the cavity model of a patch antenna were used to derive the resonance conditions for a high gain patch antenna covered with a superstrate. The resonance conditions require that the substrate-superstrate spacing and the superstrate thickness should equal to quarter wave length in the respective medium. A superstrate with very high characteristic impedance is required under these resonance conditions to achieve very high gain. The theoretical formulation for these resonance conditions were verified using numerical methods. The significant effects of anisotropic magnetic superstrates on the antenna gain and radiation efficiency were discussed. The design criteria proposed here reduces the total profile of the radiating system by 50% when compared with previous trends based on using highly-reflective superstrate and dielectric slabs superstrate.

- An engineered magnetic superstrate was introduced for gain and efficiency enhancement of low-profile antenna. The engineered superstrate based on the broadside coupled split ring resonator SRR was analytically designed and characterized. The patch antenna covered with the engineered superstrate was experimentally and numerically investigated, and compared with the case of patch without superstrate. It was shown that for a patch antenna resonating at 2.2 GHz, using the engineered magnetic superstrate results in a 3.8 dBi enhancement in gain and 14% enhancement in radiation efficiency, while maintaining an antenna profile of $\lambda_0/7$. The planar size of the radiating system was only 2.3 times the patch size. These improvements were achieved while having an insignificant effect on the impedance bandwidth of the antenna.

- To further investigate the effect of superstrate on the performance of planar printed antennas, the aforementioned engineered magnetic superstrate constructed by split-ring-resonators was used to cover a 4x1 linear microstrip array to enhance its far-field properties. The distance between the patches and the superstrates is optimized to

109

achieve a gain enhancement of about 3.5 dBi. The antenna properties such as radiation patterns and the return loss characteristics are not significantly affected by the superstrates. However, there is an improvement in efficiency of about 10%. An overall profile of $\lambda_0/7$ resulted when the superstrates is added, which is appreciably better than the other techniques of gain enhancements such as electromagnetic band gap EBG based superstrates. The superstrate-based gain enhancement method can be used in commercial antenna arrays to combat some of the downsides of the existing systems such as gain decrease due to surface waves and dielectric losses. The analytical method based on reciprocity theorem and transmission line model was extended to calculate the radiation field of the antenna array covered with artificial superstrate, the radiation patterns results are compared with the full-wave simulator CST and good agreement was achieved. The proposed formulation requires only 2.5% of the time acquired by full-wave analysis.

Another application for the SRR-based artificial superstrate is to enhance the gain of planar inverted-F Antenna (PIFA) which is commonly used in cell-phones applications. The PIFA antenna covered with the artificial superstrate was numerically investigated. It was shown that using the engineered magnetic superstrate, gain enhancement of 3.2 dBi is attainable, while maintaining a superstrate profile of $\lambda_0/14$ where λ_0 is the free-space wavelength at the PIFA's resonance frequency.

- A novel mechanism of steering the main beam of a microstrip antenna, using high refractive-index superstrate, was presented. Moreover; the antenna gain was enhanced. The proposed configuration consists of a high refractive-index superstrate partially covering the patch such that one of the radiation slots is exposed. Through full-wave simulations, the main beam of the antenna was shown to deflect to higher angles as the refractive-index of the superstrate is elevated.

The radiation mechanism was investigated by plane wave approximations and antenna array theory, the two radiation slots act as a two element array with a phase disparity that is created by the placing of the superstrate layer on one of the slots. A good agreement between the proposed plane-wave model and HFSS was obtained despite the huge difference in computational resources used by the two methods. The proposed model consumed only 1/100 of the time taken by HFSS.

Experimental results were presented to support the proposed mechanism of beam

steering and gain enhancement which can be of commercial value when used in antenna array systems for radar applications. With tuneable artificial superstrate, a reconfigurable beam steerable microstrip patch can be obtained.

7.2   Future Work

None of the research presented herein is the last word on any subject. This work lays the foundations for possible directions of further research that includes:

- **High gain and efficiency Superstrate-Antenna for Millimeter-wave technology:**
  The 60-GHz frequency band is very promising band for future wideband commercial communications as this band is announced as unlicensed all over the world [81]–[86]. Millimeter-wave technology is one approach to provide up to multi-Gb/s wireless connectivity for short distances between electronic devices. The data-transfer rate is expected to be 40-80 times faster than contemporary wireless LAN systems, transmitting an entire DVDs data in roughly 14 s. However, this novel technology will require miniaturized and high-efficiency millimeter front-ends and antennas. Hence, it is essential to design artificial magnetic superstrates working in the 60 GHz band to increase the gain and efficiency of planar antennas used in such high speed communication system.

- **Engineered magnetic structures as a substrate and superstrate of miniaturized planar antenna:**
  In the case of using metamaterials as a substrate for planar printed antennas [87]–[90], the antenna radiation efficiency and gain is degraded because of the high value of the substrate relative permittivity and the associated surface wave effects. For this reason, it is quite important to develop a technique to compensate for the reduction in the antenna efficiency and gain. Hence, using metamaterial as a substrate and a superstrate of planar antenna help reduce the size of the antenna and maintain a practical value for the gain and radiation efficiency.

- **Fast and accurate analytical solution for the radiation fields of a patch antenna partially covered with a superstrate:**

We note in Chapter (6) that for a patch antenna partially covered with a superstrate, the beam angle increases as the refractive-index of the superstrate is increased and more phase shift incurs inside the superstrate layer. Analytically, the beam angle was predicted by using plane-wave approximations in conjunction with the ray-tracing techniques. However, discrepancies and sharp edges were seen in the resultant radiation patterns which are mainly due to the omission of near field effects in the model (such as scattering and diffraction from the superstrate). Hence, taking these effects into account should help increase the accuracy of the radiation patterns calculated using this fast analytical method.

- **The development of high permeability low-loss artificial magnetic materials:**
It was shown in Chapter (3) that the higher the permeability of the superstrate the more the gain of the patch antenna. It is also shown that inclusions with larger surface area result in higher value of permeability [28, 91]. However, there is a tradeoff between increasing the permeability and decreasing the loss on the one hand and reducing dispersion, on the other hand. So, it is an attractive point of research to provide such metamaterial inclusion with high permeability, low dispersion and low-loss to help increase the gain of planar antennas.

- **Development of tunable artificial superstrate for beam steering of planar antennas:**
Another important extension to our work in Chapter (6) is to design a tunable artificial superstrate to steer the beam of patch antennas. We showed that the beam angle is proportional to the refractive-index of the superstrate. Hence, integrating a lumped-element inside the metamaterial unit cell, through the use of a varactor diode, enables us to vary the refractive-index of the superstrate in an interesting range. This tunable metamaterial superstrate is then used with a patch antenna permitting to steer the beam in different directions of the elevation plane.

APPENDICES

Appendix A

Published Work

Journal Papers:

- **Hussein Attia**, L. Yousefi, M. M. Bait-Suwailam, M. Said Boybay and O. M. Ramahi, "Enhanced-Gain Microstrip Antenna using Engineered Magnetic Superstrates," IEEE Antennas and Wireless Propagation Letters, vol. 8, pp. 1198-1201, 2009.

- **Hussein Attia**, L. Yousefi, O. Siddiqui and O. M. Ramahi, "Analytical formulation of the radiation field of printed antennas in the presence of artificial magnetic superstrates," Journal of Applied Physics A: Materials Science; Processing, Springer Berlin / Heidelberg, pp. 1-4, 2011.

- **Hussein Attia**, L. Yousefi and O. M. Ramahi, "Analytical Model for Calculating the Radiation Field of Microstrip Antennas with Artificial Magnetic Superstrates: Theory and Experiment," in press, IEEE Transaction on Antennas and Propagation.

- L. Yousefi, **Hussein Attia**, and O. M. Ramahi, "Broadband Experimental Characterization Of artificial Magnetic Materials Based on a Microstrip Line Method," Journal of Progress in Electromagnetic Research (PIER), vol. 90, pp. 1-13, 2009.

- **Hussein Attia**, O. Siddiqui and O. M. Ramahi, "High Gain and Efficiency Planar Antenna Array with Metamaterial Superstrate for UMTS Applications," Progress in Electromagnetics Research (PIER) Letters (under revision).

114

- O. Siddiqui, **Hussein Attia**, and O. M. Ramahi, "Beam Steering of a Single Patch Antenna Using High Refractive Index Superstrate," IEEE Antennas and Wireless Propagation Letters (under revision).

Conference Proceedings(peer reviewed):

- **Hussein Attia**, O. Siddiqui, and O. M. Ramahi, "Theoretical and Experimental Demonstration of Beam Steering of Patch Antenna Partially Covered with High-Index Superstrate," Submitted to IEEE Microwave Theory and Techniques Society (MTT-S) International Microwave Symposium (IMS2011), Baltimore, Maryland, USA, June 5-10, 2011.

- **Hussein Attia**, L. Yousefi, and O. M. Ramahi, "High Gain Microstrip Antennas Loaded with High Characteristic Impedance Superstrates," Submitted to IEEE Microwave Theory and Techniques Society (MTT-S) International Microwave Symposium (IMS2011), Baltimore, Maryland, USA, June 5-10, 2011.

- **Hussein Attia** and O. M. Ramahi, "Transmission Line Model to Characterize Microstrip Antennas Capped with Dielectric Superstrates," Proceeding of the 9th International Symposium on Antenna, Propagation, and EM Theory, Guangzhou, China, Nov. 29-Dec. 2, 2010.

- O. Siddiqui, **Hussein Attia** and O. M. Ramahi, "Antenna Beam Control Using High Refractive Index Superstrates," Proceeding of the 9th International Symposium on Antenna, Propagation, and EM Theory, Guangzhou, China, Nov. 29-Dec. 2, 2010.

- **Hussein Attia**, O. Siddiqui, and O. M. Ramahi, "Artificial Magneto-Superstrates for Gain and Efficiency Improvement of Microstrip Antenna Arrays," Proceeding of the 28th PIER Symposium, pp. 878-881, Cambridge, MA, USA, July 5-8, 2010.

- **Hussein Attia**, L. Yousefi, and O. M. Ramahi, "Theoretical and Experimental Investigation of Patch Antennas Loaded with Engineered Magnetic Superstrates," Proceeding of The European Wireless Technology Conference 2010 (EuWiT), Paris, France, Sept. 26-Oct. 01, 2010.

- **Hussein Attia**, L. Yousefi, and O. M. Ramahi, "Analytical Formulation of the Radiation Field of Printed Antennas in the Presence of Artificial Magnetic Superstrates,"

proceeding of META'10, the 2nd International Conference on Metamaterials, Photonic Crystals and Plasmonics, pp. 587-591, Cairo, Egypt, February 2010.

- **Hussein Attia**, Mohammed M. Bait-Suwailam, and Omar M. Ramahi, "Enhanced Gain Planar Inverted-F Antenna with Metamaterial Superstrate for UMTS Applications," Proceeding of the 28th PIER Symposium, pp. 494-497, Cambridge, MA, USA, July 5-8, 2010.

- **Hussein Attia**, L. Yousefi, and O. M. Ramahi, "High-Gain Low-profile Antenna Using Artificial Magnetic Superstrates," Proceeding of IEEE Antennas and Propagation Society International Symposium, Toronto, Ontario, Canada, July 11-17, 2010.

- O. M. Ramahi, M. S. Boybay, O. Siddiqui, L. Yousefi, A. Kabiri, **Hussein Attia**, M. Bait-Suwailam and Z. Ren, "Metamaterials: An Enabling Technology for Wireless Communications," Proceeding of International Conference on Communication Technologies ICCT2010, Riyadh, Saudi Arabia, Jan. 18-20, 2010 (Invited and keynote presentation).

- **Hussein Attia** and O. M. Ramahi, "EBG Superstrate for Gain and Bandwidth Enhancement of Microstrip Array Antennas," Proceeding of IEEE Antennas and Propagation Society International Symposium, pp. 1 - 4, San Diego, CA, USA, July 5-12, 2008.

- **Hussein Attia**, Leila Yousefi, and Omar M. Ramahi, "Analytical Calculation and Measurements of the Far-Field of Planar Antennas with Metamaterial Superstrates," The 2010 Graduate Student Research Conference, University of Waterloo, Waterloo, Canada, April 26-30, 2010.

- **Hussein Attia**, A. A. Shaalan, S. H. Zainud-Deen, and K. H. Awadalla, "Compact wideband overlapped patches microstrip antenna," proceeding of the 23rd National Radio Science Conf., Faculty of Electronic Engineering, Menouf, Egypt, March 2006.

References

[1] R. Munson, "Conformal microstrip antennas and microstrip phased arrays," *IEEE Trans. Antennas Propagat.*, vol. 22, no. 1, pp. 74 – 78, Jan. 1974. 1

[2] A. Krall, J. McCorkle, J. Scarzello, and A. Syeles, "The omni microstrip antenna: a new small antenna," *IEEE Trans. Antennas Propagat.*, vol. 27, no. 6, pp. 850 – 853, Nov. 1979.

[3] A. Derneryd, "Analysis of the microstrip disk antenna element," *IEEE Trans. Antennas Propagat.*, vol. 27, no. 5, pp. 660 – 664, Sep. 1979.

[4] ——, "A theoretical investigation of the rectangular microstrip antenna element," *IEEE Trans. Antennas Propagat.*, vol. 26, no. 4, pp. 532 – 535, Jul. 1978.

[5] P. Agrawal and M. Bailey, "An analysis technique for microstrip antennas," *IEEE Trans. Antennas Propagat.*, vol. 25, no. 6, pp. 756 – 759, Nov. 1977.

[6] P. Hammer, D. Van Bouchaute, D. Verschraeven, and A. Van de Capelle, "A model for calculating the radiation field of microstrip antennas," *IEEE Trans. Antennas Propagat.*, vol. 27, no. 2, pp. 267 – 270, Mar. 1979. 1

[7] G. V. Trentini, "Partially reflecting sheet arrays," *IRE Transactions on Antennas and Propagation,*, vol. 4, no. 4, pp. 666–671, 1956. 1, 3

[8] D. Jackson and N. Alexopoulos, "Gain enhancement methods for printed circuit antennas," *IEEE Trans. Antennas Propagat.*, vol. 33, no. 9, pp. 976–987, Sep. 1985. 1, 3, 4, 6, 12, 13

[9] N. Alexopoulos and D. Jackson, "Fundamental superstrate (cover) effects on printed circuit antennas," *IEEE Trans. Antennas Propagat.*, vol. 32, no. 8, pp. 807–816, Aug. 1984. 3, 12, 13

[10] H. Yang and N. Alexopoulos, "Gain enhancement methods for printed circuit antennas through multiple superstrates," *IEEE Trans. Antennas Propagat.*, vol. 35, no. 7, pp. 860–863, Jul. 1987. 1, 3, 4, 6

[11] W. Choi, C. Pyo, Y. H. Cho, J. Choi, and J. Chae, "High gain and broadband microstrip patch antenna using a superstrate layer," in *Proceeding of IEEE AP-S Int. Symp. Antennas Propagat.*, vol. 2, 2003, pp. 292 – 295. 1, 4

[12] F. Kaymaram and L. Shafai, "Enhancement of microstrip antenna directivity using double-superstrate configurations," *Canadian Journal of Electrical and Computer Engineering*, vol. 32, no. 2, pp. 77–82, 2007. 3, 4

[13] C. Cheype, C. Serier, M. Thevenot, T. Monediere, A. Reineix, and B. Jecko, "An electromagnetic bandgap resonator antenna," *IEEE Trans. Antennas Propagat.*, vol. 50, no. 9, pp. 1285 – 1290, Sep. 2002. 4

[14] Y. J. Lee, J. Yeo, R. Mittra, and W. S. Park, "Application of electromagnetic bandgap (EBG) superstrates with controllable defects for a class of patch antennas as spatial angular filters," *IEEE Trans. Antennas Propagat.*, vol. 53, no. 1, pp. 224–235, Jan. 2005. 5, 12, 29, 30

[15] H. Attia and O. M. Ramahi, "EBG superstrate for gain and bandwidth enhancement Of microstrip array antennas," in *Proceeding of IEEE AP-S Int. Symp. Antennas Propagat.*, San Diego, CA, 2008, pp. 1–4. 5

[16] A. Pirhadi, M. Hakkak, F. Keshmiri, and R. Baee, "Design of Compact Dual Band High Directive Electromagnetic Bandgap (EBG) Resonator Antenna Using Artificial Magnetic Conductor," *IEEE Trans. Antennas Propagat.*, vol. 55, no. 6, pp. 1682–1690, 2007. 5

[17] L. H. Lee, Y. J. Lee, J. Yeo, R. Mittra, and W. Park, "Design of novel thin frequency selective surface superstrates for dual-band directivity enhancement," *IET Microwaves, Antennas Propagation*, vol. 1, no. 1, pp. 248–254, 2007. 1, 4, 5

118

[18] W. R. Deal, N. Kaneda, J. Sor, Y. Qian, and T. Itoh, "A new quasi-yagi antenna for planar active antenna arrays," *IEEE Trans. Microwave Theory Tech.*, vol. 48, no. 6, pp. 910–918, Jun. 2000. 1

[19] S. Yang, Y.-B. Gan, and P. K. Tan, "Linear antenna arrays with bidirectional phase center motion," *IEEE Trans. Antennas Propagat.*, vol. 53, no. 5, pp. 1829 – 1835, May 2005.

[20] Y. Zhang, A. Kishk, A. Yakovlev, and A. Glisson, "Analysis of wideband dielectric resonator antenna arrays for waveguide-based spatial power combining," *IEEE Trans. Microwave Theory Tech.*, vol. 55, no. 6, pp. 1332 –1340, 2007.

[21] T. Seki, N. Honma, K. Nishikawa, and K. Tsunekawa, "Millimeter-wave high-efficiency multilayer parasitic microstrip antenna array on teflon substrate," *IEEE Trans. Microwave Theory Tech.*, vol. 53, no. 6, pp. 2101 – 2106, 2005.

[22] D. Browne, M. Manteghi, M. Fitz, and Y. Rahmat-Samii, "Experiments with compact antenna arrays for MIMO radio communications," *IEEE Trans. Antennas Propagat.*, vol. 54, no. 11, pp. 3239 –3250, 2006. 1

[23] R. A. Pucel and D. J. Masse, "Microstrip propagation on magnetic substrates," *IEEE Trans. Microwave Theory Tech.*, vol. 20, pp. 304–313, 1972. 6, 42

[24] O. Acher and A. L. Adenot, "Bounds on the dynamic properties of magnetic materials," *Phys. Rev. B*, vol. 62, no. 17, pp. 11 324–11 327, 2000.

[25] A. F. Starr, P. M. Rye, D. R. Smith, and S. Nemat-Nasser, "Fabrication and characterization of a negative-refractive-index composite metamaterial," *Physical Review B*, vol. 70, p. 113102, 2004.

[26] A. Buerkle, and K. Sarabandi, "A circularly polarized magneto-dielectric resonator antenna with wideband, multi-resonant response," in *Proceeding of IEEE AP-S Int. Symp. Antennas Propagat.*, Jul. 2005, pp. 487–490.

[27] D. R. Smith, D. Schurig, and J. J. Mock, "Characterization of a planar artificial magnetic metamaterial surface," *Physical Review E*, vol. 74, p. 036604, 2006.

[28] A. Kabiri, L. Yousefi, and O. Ramahi, "On the fundamental limitations of artificial magnetic materials," *IEEE Trans. Antennas Propagat.*, vol. 58, no. 7, pp. 2345 –2353, 2010. 42, 112

[29] L. Yousefi and O. M. Ramahi, "Artificial magnetic materials using fractal hilbert curves," *IEEE Trans. Antennas Propagat.*, vol. 58, no. 8, pp. 2614–2622, 2010. 42

[30] J. B. Pendry, A. J. Holden, D. J. Robbins, and W. J. Stewart, "Magnetism from conductors and enhanced nonlinear phenomena," *IEEE Transactions on Microwave Theory and Techniques*, vol. 47, no. 11, pp. 2075–2084, 1999. 6, 42

[31] H. Mosallaei and K. Sarabandi, "Magneto-dielectrics in electromagnetics: Concept and applications," *IEEE Trans. Antennas Propagat.*, vol. 52, no. 6, pp. 1558–1567, Jun. 2004.

[32] S. Maslovski, P. Ikonen, I. Kolmakov, and S. Tretyakov, "Artificial magnetic materials based on the new magnetic particle: Metasolenoid," *Journal of Progress in Electromagnetic Research (PIER)*, vol. 54, no. 9, pp. 61–81, Sept. 2005. 48, 51, 54, 55

[33] K. Buell, H. Mosallaei, and K. Sarabandi, "A substrate for small patch antennas providing tunable miniaturization factors," *IEEE Trans. Antennas Propagat.*, vol. 54, no. 1, pp. 135–146, Jan. 2006. 6, 39, 42, 43, 52, 57

[34] P. M. T. Ikonen, S. I. Maslovski, C. R. Simovski, and S. A. Tretyakov, "On artificial magnetodielectric loading for improving the impedance bandwidth properties of microstrip antennas," *IEEE Trans. Antennas Propagat.*, vol. 54, no. 6, pp. 1654–1662, 2006. 6, 43, 48

[35] A. Foroozesh and L. Shafai, "Size reduction of a microstrip antenna with dielectric superstrate using meta-materials: Artificial magnetic conductors versus magneto-dielectrics," in *Proceeding of IEEE AP-S Int. Symp. Antennas Propagat.*, Albuquerque, NM, Jul. 2006, pp. 11–14. 6

[36] E. Saenz, R. Gonzalo, I. Ederra, J. C. Vardaxoglou, and P. de Maagt, "Resonant meta-surface superstrate for single and multifrequency dipole antenna arrays," *IEEE Trans. Antennas Propagat.*, vol. 56, no. 4, pp. 951–960, 2008. 7

[37] M. Latrach, H. Rmili, C. Sabatier, E. Seguenot, and S. Toutain, "Design of a new type of metamaterial radome for low frequencies," in *Proceeding of META08 and NATO Adv. Rese. Workshop: Metamater. Secure Inf. Commun. Technol.*, Marrakesh, Morocco, May 2008, p. 202211. 6, 7

[38] N. Krejic, J. M. Martinez, M. Mello, and E. A. Pilotta, "Validation of an augmented Lagrangian algorithm with a Gauss-Newton Hessian approximation using a set of hard-spheres problems," *Computational Optimization and Applications*, vol. 16, no. 3, pp. 247–263, 2000. 7, 33

[39] D. R. Jackson, A. A. Oliner, and A. Ip, "Leaky-wave propagation and radiation for a narrow-beam multiple-layer dielectric structure," *IEEE Trans. Antennas Propagat.*, vol. 41, no. 3, pp. 344 –348, Mar. 1993. 12, 13, 30

[40] T. Zhao, D. R. Jackson, J. T. Williams, H. Y. D. Yang, and A. A. Oliner, "2-D periodic leaky-wave antennas-part I: metal patch design," *IEEE Trans. Antennas Propagat.*, vol. 53, no. 11, pp. 3505 – 3514, Nov. 2005.

[41] G. Lovat, P. Burghignoli, and D. R. Jackson, "Fundamental properties and optimization of broadside radiation from uniform leaky-wave antennas," *IEEE Trans. Antennas Propagat.*, vol. 54, no. 5, pp. 1442 –1452, May. 2006.

[42] X. H. Wu, A. A. Kishk, and A. Glisson, "A transmission line method to compute the far-field radiation of arbitrarily directed hertzian dipoles in a multilayer dielectric structure: Theory and applications," *IEEE Trans. Antennas Propagat.*, vol. 54, no. 10, pp. 2731–2741, Oct. 2006. 13

[43] ——, "A transmission line method to compute the far-field radiation of arbitrary hertzian dipoles in a multilayer structure embedded with pec strip interfaces," *IEEE Trans. Antennas Propagat.*, vol. 55, no. 11, pp. 3191–3198, Nov. 2007. 13

[44] A. Foroozesh and L. Shafai, "Effects of artificial magnetic conductors in the design of low-profile high-gain planar antennas with high-permittivity dielectric superstrate," *IEEE Antenna Wireless Propagat. Lett.*, vol. 8, pp. 10 –13, 2009. 12, 13

[45] ——, "Investigation into the effects of the patch-type FSS superstrate on the high-gain cavity resonance antenna design," *IEEE Trans. Antennas Propagat.*, vol. 58, no. 2, pp. 258–270, Feb. 2010. 12, 29, 30

[46] H. Vettikalladi, L. L. Coq, O. Lafond, and M. Himdi, "Wideband and high efficient aperture antenna with superstrate for 60 GHz indoor communication systems," in *Proceeding of IEEE AP-S Int. Symp. Antennas Propagat.*, 2010, pp. 1–4. 12, 30

[47] R. Mittra, Y. Li, and K. Yoo, "A comparative study of directivity enhancement of microstrip patch antennas with using three different superstrates," *Microwave and Optic. Tech. Letts.*, vol. 52, no. 2, pp. 327–331, Feb. 2010. 12

[48] Y. Lo, D. Solomon, and W. Richards, "Theory and experiment on microstrip antennas," *IEEE Trans. Antennas Propagat.*, vol. 27, no. 2, pp. 137–145, Mar. 1979. 14, 15, 91

[49] R. E. Collin, *Antennas and radiowave propagation.* Mcgraw-Hill College, 1985.

[50] K. Carver and J. Mink, "Microstrip antenna technology," *IEEE Trans. Antennas Propagat.*, vol. 29, no. 1, pp. 2–24, Jan. 1981. 23, 89

[51] W. Richards, Y. T. Lo, and D. Harrison, "An improved theory for microstrip antennas and applications," *IEEE Trans. Antennas Propagat.*, vol. 29, no. 1, pp. 38–46, Jan. 1981. 14

[52] R. F. Harrington, *Time-Harmonic electromagnetic fields.* McGraw-Hill, 1961. 14, 44

[53] D. M. Pozar, *Microwave Engineering*, 2nd ed. John Wiley, 1998. 18, 55

[54] K. Buell, *Development of engineered magnetic materials for antenna applications.* Ph.D. Thesis, University of Michigan, 2005. 43

[55] W. D. Callister, *Materials science and engineering: an introduction.* John Wiley Sons, Inc, 2000. 46

[56] L. Yousefi and O. M. Ramahi, "New artificial magnetic materials based on fractal hilbert curves," in *International Workshop on Antenna Technology: Small and Smart Antennas Metamaterials and Applications*, 2007. 43, 59, 60

[57] ——, "Engineered magnetic materials with improved dispersion using multi-resonator structures," in *Canadian Conference on Electrical and Computer Engineering*, 2007, pp. 966–969. 43, 45, 55, 60

[58] "Trans-Tech company, http://www.trans-techinc.com/." 47

[59] X. Chen, T. M. Grzegorczyk, B. Wu, J. Pacheco, and J. A. Kong, "Robust method to retrieve the constitutive effective parameters of metamaterials," *Phys. Rev. E*, vol. 70, no. 1, p. 016608, Jul. 2004. 47, 59, 60, 61

[60] N. G. Alexopoulos, C. A. Kyriazidou, and H. F. Contopanagos, "Effective parameters for metamorphic materials and metamaterials through a resonant inverse scattering approach," *IEEE Transactions on Microwave Theory and Techniques*, vol. 55, no. 2, pp. 254–267, 2007.

[61] A. Alu and N. Engheta, "Pairing an epsilon-negative slab with a mu-negative slab: resonance, tunneling and transparency," *IEEE Trans. Antennas Propagat.*, vol. 51, no. 10, pp. 2558–2571, 2003. 47

[62] Q. Wang, D. Plettemeier, H. Zhang, K. Wolf, and E. Ohlmer, "Design and diversity performance of optimized dual-element PIFA antennas for MIMO handsets," in *A2010 International Workshop on ntenna Technology (iWAT)*, 2010, pp. 1 –4. 82

[63] Y.-S. Wang, M.-C. Lee, and S.-J. Chung, "Two PIFA-related miniaturized dual-band antennas," *IEEE Trans. Antennas Propagat.*, vol. 55, no. 3, pp. 805 –811, 2007.

[64] L. Feldner, C. Rodenbeck, C. Christodoulou, and N. Kinzie, "Electrically small frequency-agile PIFA-as-a-package for portable wireless devices," *IEEE Trans. Antennas Propagat.*, vol. 55, no. 11, pp. 3310 –3319, 2007.

[65] C. Y. Chiu, K. M. Shum, and C. H. Chan, "A Tunable via-patch loaded PIFA with size reduction," *IEEE Trans. Antennas Propagat.*, vol. 55, no. 1, pp. 65 –71, 2007.

[66] K.-L. Wong, C.-H. Chang, and Y.-C. Lin, "Printed PIFA EM compatible with nearby conducting elements," *IEEE Trans. Antennas Propagat.*, vol. 55, no. 10, pp. 2919–2922, 2007. 82

[67] C.-H. Chang and K.-L. Wong, "Printed $\lambda/8$ -PIFA for penta-band WWAN operation in the mobile phone," *IEEE Trans. Antennas Propagat.*, vol. 57, no. 5, pp. 1373–1381, May 2009. 82

[68] Z. Du, K. Gong, J. Fu, B. Gao, and Z. Feng, "A compact planar inverted-F antenna with a PBG-type ground plane for mobile communications," *IEEE Transactions on Vehicular Technology*, vol. 52, no. 3, pp. 483 – 489, May 2003. 82

[69] T.-C. Lo and Y. Hwang, "Bandwidth enhancement of PIFA loaded with very high permittivity material using FDTD," in *Proceeding of IEEE AP-S Int. Symp. Antennas Propagat.*, vol. 2, Jun. 1998, pp. 798–801. 82

[70] M. F. Abedin and M. Ali, "Modifying the ground plane and its effect on planar inverted-F antennas (PIFAs) for mobile phone handsets," *IEEE Antenna Wireless Propagat. Lett.*, vol. 2, pp. 226 – 229, 2003. 82

[71] M. A. Jensen, and Y. Rahmat-Samii, "Em interaction of handset antennas and a human in personal communications," in *Proceedings of the IEEE*, no. 1, 1995, pp. 7 –17. 82

[72] C. A. Balanis, *Antenna theory: analysis and design*, 2nd ed. John Wiley, 1997. 89, 92

[73] E. Ojefors, S. Cheng, K. From, I. Skarin, P. Hallbjorner, and A. Rydberg, "Electrically steerable single-layer microstrip traveling wave antenna with varactor diode based phase shifters," *IEEE Trans. Antennas Propagat.*, vol. 55, no. 9, pp. 2451–2460, 2007. 91

[74] R. R. Romanofsky, "Advances in scanning reflectarray antennas based on ferroelectric thin-film phase shifters for deep-space communications," *Proceedings of the IEEE*, vol. 95, no. 10, pp. 1968–1975, 2007.

[75] K. Topalli, O. A. Civi, S. Demir, S. Koc, and T. Akin, "A Monolithic phased array using 3-bit distributed RF MEMS phase shifters," *IEEE Trans. Microwave Theory Tech.*, vol. 56, no. 2, pp. 270–277, 2008.

[76] M. Abdalla, K. Phang, and G. Eleftheriades, "A Planar electronically steerable patch array using tunable PRI/NRI phase shifters," *IEEE Trans. Microwave Theory Tech.*, vol. 57, no. 3, pp. 531–541, 2009.

[77] T.-Y. Chin, S.-F. Chang, J.-C. Wu, and C.-C. Chang, "A 25-GHz compact low-power phased-array receiver with continuous beam steering in CMOS technology," *IEEE Journal of Solid-State Circuits,*, vol. 45, no. 11, pp. 2273–2282, 2010. 91

[78] H. Griguer, M. Drissi, E. Marzolf, H. Lalj, and F. Riouch, "Design and characterization of a tunable DNG metamaterial superstrate for small beam steering antennas," in *Proceeding of META'10, the 2nd International Conference on Metamaterials, Photonic Crystals and Plasmonics*, Cairo, Egypt, 2010, pp. 255–259. 91

[79] F. Bayatpur and K. Sarabandi, "A tunable metamaterial frequency-selective surface with variable modes of operation," *IEEE Trans. Microwave Theory Tech.*, vol. 57, no. 6, pp. 1433–1438, Jun. 2009. 91

[80] S. Orfanidis, *Electromagnetic, waves, and antennas.* online edition at www.ece.rutgers.edu/ orfanidi/ewa, 2008. 93

[81] A. Nesic, D. Nesic, V. Brankovic, K. Sasaki, and K. Kawasaki, "Antenna solution for future communication devices in mm-wave range," in *5th International Conference on Telecommunications in Modern Satellite, Cable, and Broadcasting Service, TELSIKS 2001*, vol. 1, 2001, pp. 194–202. 111

[82] P. Smulders, "Exploiting the 60 GHz band for local wireless multimedia access: prospects and future directions," *IEEE Communications Magazine*, vol. 40, no. 1, pp. 140–147, Jan. 2002.

[83] Y. Zhang, M. Sun, K. Chua, L. Wai, and D. Liu, "Antenna-in-Package design for wirebond interconnection to highly integrated 60-GHz radios," *IEEE Trans. Antennas Propagat.*, vol. 57, no. 10, pp. 2842–2852, 2009.

[84] L. Pazin and Y. Leviatan, "A Compact 60-GHz tapered slot antenna printed on LCP substrate for WPAN applications," *IEEE Antenna Wireless Propagat. Lett.*, 2010.

[85] C.-H. Tseng, C.-J. Chen, and T.-H. Chu, "A Low-cost 60-GHz switched-beam patch antenna array with butler matrix network," *IEEE Antenna Wireless Propagat. Lett.*, 2008.

[86] M. Sun, Y. Zhang, Y. Guo, K. Chua, and L. Wai, "Integration of grid array antenna in chip package for highly integrated 60-GHz radios," *IEEE Antenna Wireless Propagat. Lett.*, 2009. 111

[87] F. Bilotti, A. Alu, and L. Vegni, "Design of miniaturized metamaterial patch antennas with μ -negative loading," *IEEE Trans. Antennas Propagat.*, vol. 56, no. 6, pp. 1640 –1647, 2008. 111

[88] P. Mookiah and K. Dandekar, "Metamaterial-substrate antenna array for MIMO communication system," *IEEE Trans. Antennas Propagat.*, vol. 57, no. 10, pp. 3283 –3292, 2009.

[89] J. Liang and H. Yang, "Microstrip patch antennas on tunable electromagnetic bandgap substrates," *IEEE Trans. Antennas Propagat.*, vol. 57, no. 6, pp. 1612 –1617, 2009.

[90] H. Mosallaei and K. Sarabandi, "Design and modeling of patch antenna printed on magneto-dielectric embedded-circuit metasubstrate," *IEEE Trans. Antennas Propagat.*, vol. 55, no. 1, pp. 45 –52, 2007. 111

[91] P. Ikonen and S. Tretyakov, "Determination of generalized permeability function and field energy density in artificial magnetics using the equivalent-circuit method," *IEEE Transactions on Microwave Theory and Techniques,*, vol. 55, no. 1, pp. 92–99, 2007. 112